Turbulence Observations on Soundings Balloons: Geophysical Interpretations based on Instrumental Revisions

Dissertation
zur
Erlangung des akademischen Grades
doctor rerum naturalium (Dr. rer. nat.)
an der Mathematisch-Naturwissenschaftlichen Fakultät
der Universität Rostock

vorgelegt von:
Jens Söder
geboren am 13. Januar 1987
in Osnabrück

eingereicht: 10.12.2019
verteidigt: 15.05.2020
korrigiert: 14.07.2020

Gutachter:
Prof. Franz-Josef Lübken
(Leibniz-Institut für Atmosphärenphysik)
Prof. Richard Wilson
(Sorbonne Université Paris, Frankreich)

Universität Rostock Traditio et Innovatio

LEIBNIZ-INSTITUT FÜR ATMOSPHÄREN PHYSIK IAP

https://doi.org/10.18453/rosdok_id00002707

Abstract

The occurrence and impact of atmospheric turbulence are manifold. It is associated with the breakdown of gravity waves, induces small-scale mixing and drives larger scale flows by vorticity generation. Since turbulent processes involve spatial scales below one meter, only high-resolution in situ measurements allow for reliable turbulence observations in the atmosphere. Our balloon-borne LITOS instrument (Leibniz-Institute Turbulence Observations in the Stratosphere) measures turbulence strength by inferring kinetic energy dissipation rates from velocity fluctuations.

In the course of this research, the LITOS instrument and turbulence retrieval have been substantially refined. Most important, we identified the consequences of encountering the balloon's wake on the gondola below the balloon. A software tool has been created that calculates the likelihood of encountering the balloon's wake on an ascending balloon. We find that the balloon's wake and the wake from smaller objects, like the payload suspension ropes, fundamentally impact high-resolution turbulence measurements like LITOS. However, these influence can be completely avoided by measuring with the sensors facing downwards on a descending balloon.

Furthermore, we achieved a significant noise reduction by revising the electronics and adapting our retrieval scheme. Additionally, the impact of rarefied flow conditions in the stratosphere on constant temperature anemometer (CTA) measurements are investigated using the Direct Simulation Monte Carlo method. A significant reduction of the CTA signal is found for Knudsen numbers below $Kn < 0.1$, which is as large as the reduction from density effects. Due to likely influences of this signal reduction on our retrieval scheme we do not retrieve energy dissipation rates for $Kn < 0.1$ (altitudes larger than $\sim 17.5\,\mathrm{km}$), but limit our analysis to separating turbulent from non-turbulent layers.

These data quality improvements allow for a clear separation of atmospheric turbulence from instrumental artefacts. A comparison with turbulence measurements from the newly built HYFLITS instrument (University of Colorado Boulder) shows a reasonably good correlation ($r = 0.71$). Possibilities for further developments on the LITOS payload are shown based on this comparison.

This revised and reviewed version of the LITOS instrument is used for two geophysical case studies. The first study investigates turbulence generation by gravity wave attenuation in a wind minimum. It is shown that this concept also holds for shallow wind minima with vertical extents much smaller than the vertical wavelength of the attenuated gravity wave. In the second case study, turbulence generation in the vicinity of a tropopause fold is investigated. Previously, turbulence has been known to play a significant role in the generation of tropopause folds. Here, we present one of the very few turbulence measurements under theses conditions. The observed turbulence pattern shows enhanced dissipation rates above the tropopause jet, but not below. This picture differs significantly from the expectations of previous publications, calling for further experimental investigations of the phenomenon.

Zusammenfassung

Sowohl das Auftreten als auch die Einflüsse von atmosphärischer Turbulenz sind vielfältig: sie steht in Verbindung mit dem Brechen von Schwerewellen, ruft kleinskalige Mischungsprozesse hervor und treibt durch Erzeugung von Vortizität großskalige Strömungen an. Weil turbulente Prozesse auch auf Skalen kleiner als ein Meter ablaufen, können zuverlässige Turbulenzmessungen in der Atmosphäre nur mit hoher Auflösung und in-situ durchgeführt werden. Unser ballongetragenes LITOS Instrument (Leibniz-Institute Turbulence Observations in the Stratosphere) misst die Turbulenzstärke, indem es kinetische Energiedissipationsraten aus Geschwindigkeitsfluktuationen bestimmt.

Im Verlauf dieser Arbeit sind das LITOS Instrument und die Auswertung der Turbulenzdaten grundlegend verbessert worden. Der wichtigste Punkt war es festzustellen, welche Konsequenzen auftreten, wenn der turbulente Nachlauf des Ballons die Gondel trifft. Es ist ein Computerprogramm entwickelt worden, das für aufsteigende Ballone die Wahrscheinlichkeit dafür berechnet, den turbulenten Nachlauf zu treffen. Es ist uns gelungen fundamentale Beeinflussungen von hochaufgelösten Turbulenzmessungen wie LITOS aufzudecken. Diese sind verursacht durch den Nachlauf des Ballons und den Nachlauf kleinerer Objekte wie der Schnüre an der Gondel. Allerdings können diese Störungen durch Messungen auf absteigenden Ballons mit den Sensoren an der Unterseite der Gondel komplett vermieden werden.

Desweiteren haben wir durch eine Überarbeitung der Elektronik und die Anpassung unseres Auswertungsschemas eine signifikante Reduzierung des instrumentellen Rauschens erreicht. Zusätzlich werden Einflüsse verdünnter Strömungen auf Konstant-Temperatur-Anemometrie (CTA) mit Hilfe der Direct Simulation Monte Carlo Method untersucht. Für Knudsen Zahlen kleiner als $Kn < 0.1$ (Höhen größer als $\sim 17.5\,\mathrm{km}$) wird eine erhebliche Abnahme des CTA Signals aufgrund der Verdünnung des Mediums festgestellt. Diese Abnahme ist nahezu gleich groß wie die Reduzierung des Signals durch den Effekt der Dichte. Da man durch diese Signalreduzierung eine Beeinträchtigung unsere Turbulenzauswertung erwarten kann, leiten wir für $Kn < 0.1$ (Höhen größer als $\sim 17.5\,\mathrm{km}$) keine Energiedissipationsraten ab. Stattdessen beschränken wir unsere Analyse auf das Unterscheiden von turbulenten und nicht-turbulenten Höhenbereichen.

Diese Verbesserungen der Datenqualität erlauben eine klare Unterscheidung zwischen atmosphärischer Turbulenz und instrumentellen Artefakten. Der Vergleich mit Turbulenzmessungen des neuen Instruments HYFLITS (Universität von Colorado Boulder) zeigen eine hinreichend gute Korrelation ($r = 0.71$). Ferner werden auf Grundlage dieses Vergleichs Möglichkeiten zur Weiterentwicklung der LITOS-Nutzlast aufgezeigt.

Die überarbeitete und überprüfte Version des LITOS Instruments wird für zwei geophysikalische Fallstudien genutzt. In der ersten wird Turbulenzentstehung durch Schwerewellen und einem Wind-Minimum untersucht. Es wird gezeigt, dass dieses Konzept auch auf flache Wind-Minima anwendbar ist. Dies gilt auch dann, wenn sie eine im Vergleich zur vertikale Wellenlänge der gedämpften Schwerewelle wesentlich kleinere vertikalen Ausdehnung haben. In der zweiten Fallstudie wird Turbulenzentstehung in der Umgebung einer Tropopausenfalte untersucht. Bereits zuvor war bekannt, dass Turbulenz eine wesentliche

Rolle bei der Entstehung von Tropopausenfalten spielt. Hier wird eine der wenigen Turbulenzmessungen unter diesen Bedingungen präsentiert. Das beobachtete Turbulenzmuster zeigt erhöhte Dissipationsraten über dem Tropopausen-Jet aber nicht darunter. Dieses Bild unterscheidet sich signifikant von den Erwartungen aus frühere Publikationen. Aus diesem Grund erscheinen weitere Messstudien zu dem Phänomens wünschenswert.

Contents

Introduction

Studying atmospheric turbulence is a truly fascinating field of science. It is of fundamental importance for energy transport, the mixing of trace gases and aviation safety. However, due to the multitude of scales involved in the geophysical processes leading to and representing turbulence, there is not just *one* exhaustive method to study the phenomenon. Instead, it is the author's personal impression that only a combination of high-resolution in situ measurements, numerical weather prediction and analytical models will lead to advances in the field.

This thesis primarily focuses on the measurements. However, numerical models are used to assess the performance of the instrument as well as to understand the meteorological conditions that led to the formation of turbulence. Furthermore, generalised hypotheses on the interaction of turbulence with the background flow are compared to our measurements. Last but not least, an independent intercomparison with another turbulence measuring instrument is performed. However, *measuring turbulence* is not only interesting from the perspective of the geophysical outcome; discussing what the term *turbulence* means at all will be the substance of the following section.

On the nature of turbulence

The word *turbulence* is widely used in everyday language. Most people will acknowledge that for example a volcanic plume as shown in Figure 0.1 looks turbulent. The question is: *How can we tell that it really is turbulent*? When it comes to defining turbulence, even more recent textbooks (e.g. Lesieur, 2008; Pope, 2000; Mathieu and Scott, 2000) rely on listing common properties of turbulent flows. Here, a few examples of turbulent flows are used to illustrate these properties (as highlighted by bold print). One of the earlier descriptions of turbulence was given by Richardson (1922, p. 66):

> Big whirls have little whirls
> that feed on their velocity,
> and little whirls have lesser whirls
> and so on to viscosity

Figure 0.1: Volcanic plume of Anak Krakatau on 7 Feb 2008 (CC BY 2.0)

Also from Figure 0.1 one may see that the plume shows structures of different length scales. In other words, there are a multitude of eddies (or *whirls* in Richardson's (1922) terminology) of different sizes that exist at the same time in a common volume. This is referred to as a **multi-scale flow**.

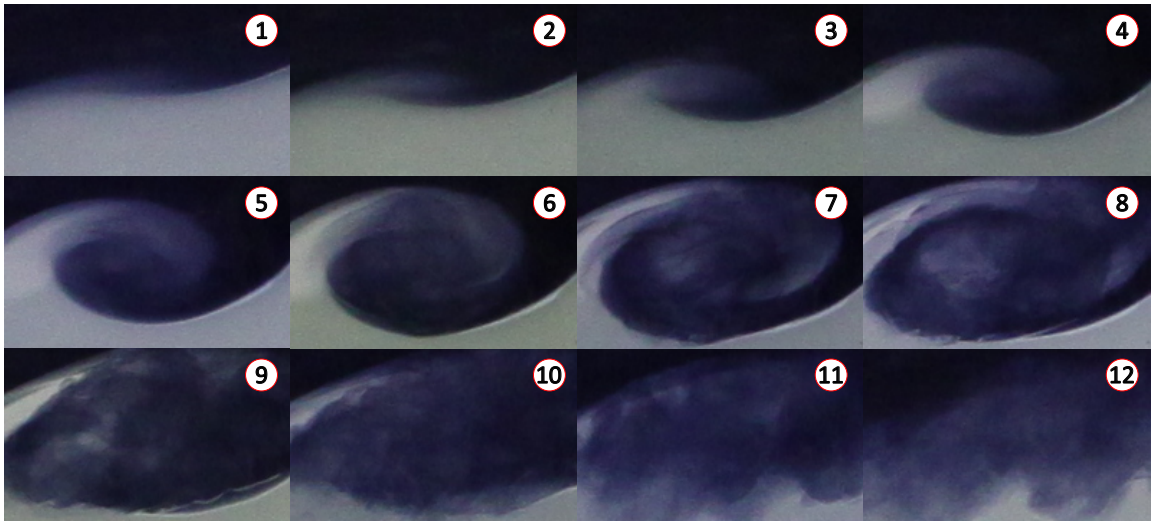

Figure 0.2: The evolution of a Kelvin-Helmholtz billow. Total time of the sequence is 2 s.

Turbulence can be created by several types of instability in a flow. One of them is a *Kelvin-Helmholtz instability* (KHI). It is driven by the vertical shear of a horizontal flow in a stably stratified fluid and is one of the most common types of instability in the atmosphere (e.g. Fritts and Alexander, 2003). The time evolution of such an instability in a laboratory experiment can be seen in Figure 0.2 (six pictures per second). For a complete view of the apparatus, please see Figure 0.3. In our experiment the upper phase of the flow (blue) moves to the right and the lower phase (grey) moves to the left. At the beginning, the interface of the fluids shows a wave-like deformation. This deformation steepens and starts overturning (1-4). In the following phase (5-8), structures of smaller spatial scales start to grow within the larger-scale billows. The shape of the overturning billow remains intact however. These smaller structures overturn and form vortices (eddies). This points to another characteristic of turbulent flows, namely that they are **rotational down to the smallest scales** (Mathieu and Scott, 2000; Tennekes and Lumley, 1972). In the final phase (9-12), the outer structure of the billow vanishes but turbulence still occurs on different length scales.

This particular example of a KHI was created using fresh water layered on saltwater in a tank. Turbulence in general, however, can be seen in any arbitrary liquid or gas. It occurs in fluids as diverse as molten metal or air. This suggests that turbulence is a **property of the flow, not the fluid**. Accordingly, it should be possible to characterise flows that are likely to become turbulent and differentiate them from those that are not. Pioneering work on this matter has been done by Reynolds (1883, p.938). He introduced a dimensionless parameter that denotes the ratio of inertial forces to viscous forces, which has been subsequently named *Reynolds number*:

$$Re = \frac{U\,l}{\nu}. \tag{0.1}$$

U describes the characteristic velocity of the fluctuations and l the characteristic length scale. In the case of a pipe flow, for example, *characteristic* means the mean speed of the flow through the pipe and its diameter. If turbulence is present, inertial forces prevail over viscous forces, making it a **high Reynolds number flow**.

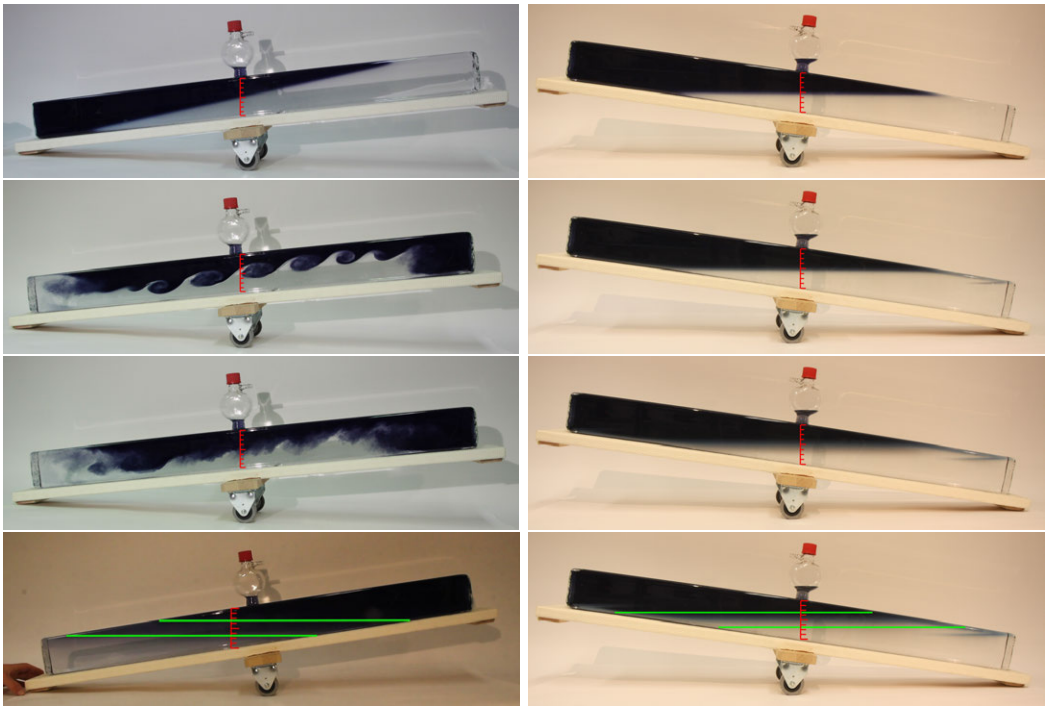

Figure 0.3: Left: Evolving Kelvin-Helmholtz instability (KHI). Right: Molecular diffusion after 0, 12, 24 and 36 h, respectively (top to bottom). The ticks on the red scales in the middle of the tank are 1 cm apart. The green lines are meant to show the extend of the mixed layer. The pictures visualise that turbulent mixing is much faster compared to molecular diffusion.

Another point introduced by Reynolds (1895, p.134) is the so-called *Reynolds decomposition*. It states that in a turbulent flow the speed of the flow can conveniently be separated in a slowly varying background $\langle u \rangle$ and the turbulent fluctuations u':

$$u = \langle u \rangle + u'. \tag{0.2}$$

The turbulent fluctuations u' are of a random nature. In a statistical sense it is assumed that they are isotropic and homogeneous (e.g. Lesieur, 2008, 1.5.3). This is used in the statistical approach to turbulence established by Kolmogorov (1941) and briefly outlined in Section 1.2.

Another feature of turbulence can be seen when stirring milk into a cup of coffee: **it strongly enhances the dispersion of material and heat** (e.g. Mathieu and Scott, 2000). In the atmosphere, turbulent mixing plays a role in transporting trace gases within the troposphere. Furthermore, turbulent mixing is important for troposphere-stratosphere exchange processes (e.g. Butchart, 2014).

A demonstration of enhanced mixing caused by turbulence is shown in Figure 0.3. In both cases, the tank is filled with salt water (salinity $\sim 15\,\%$, high density) on the bottom and coloured fresh water on top (low density). In the left column, a KHI is generated by tilting the tank, which in turn creates a shear flow at the halocline. It takes about $\tau_\mathrm{t} = 10\,\mathrm{s}$ from the onset of the KHI until the eddies have stopped. Afterwards, there is a mixed layer with a thickness of about 3 cm (marked by green lines). $\tau_\mathrm{t} = 10\,\mathrm{s}$ indicates that the turbulent motion stops rather quickly after the energy input (shear flow) has stopped. This points

to the **dissipative** nature of turbulent flows. Due to this property of turbulent flows, the turbulent kinetic energy dissipation rate ε is an adequate measure of turbulence strength. It describes the kinetic energy per unit mass and time that is dissipated to heat within a turbulent flow. The spectral properties of the dissipation process shown in Figure 0.3 are discussed in Section 1.2.

In the right column, the same experiment is shown without any turbulence (tank not tilted). Here, molecular diffusion takes about $\tau_\mathrm{m} = 36\,\mathrm{h}$ to generate a mixed layer of similar depth. Accordingly, in the current example, turbulent diffusion was more than four orders of magnitude faster than molecular diffusion. This again highlights the importance of turbulence for atmospheric mixing processes.

Content overview

After this general overview on turbulence, the different subjects of this thesis will be introduced. Even though each chapter covers individual issues, their content is grouped around three questions. These questions mark the key conceptual points of this thesis as opposed to work packages that govern the arrangement of chapters and sections.

Q 1 Which theoretical models, measurement concepts and hardware solutions are suitable for atmospheric turbulence measurements?

Q 2 Which quality control procedures are needed for reliable measurements?

Q 3 Which results have been obtained with the revised LITOS instrument?

These questions will be addressed within the separate chapters as follows:

Ch. 1 gives an overview on the impact of atmospheric turbulence. In the first part, it provides a brief introduction on the conditions under which atmospheric turbulence arises. In the second part, it introduces the measurement concept of LITOS in comparison with other techniques to obtain energy dissipation rates. Accordingly, this chapter mainly deals with **Q 1**.

Ch. 2 introduces the hardware concept and the turbulence retrieval scheme of the LITOS instrument, and documents changes that have been made to both in the course of this project. Furthermore, numerical simulations that describe aerodynamic effects of flow rarefication on the readings of our wind fluctuation measurement are presented and evaluated. The last part of the chapter is concerned with the aerodynamic behaviour of sounding balloons and its impact on turbulence measurements. Therefore, this chapter delivers answers on **Q 1** and **Q 2**.

Ch. 3 deals with wake effects on rising balloons. A prediction tool for the probability of encountering the balloon's wake at the payload is presented and evaluated. Furthermore, effects of the wake from smaller objects close to the sensors are described. This is augmented by an evaluation of wake influences on several LITOS flights as well as their possible influences on radiosonde analyses (**Q 2**).

Ch. 4 presents a comparative study where an atmospheric turbulence sounding has been performed with two independent instruments using different evaluation techniques. Within this chapter, technical comparisons of the LITOS and the HYFLITS measurement are performed as well as the occurrence of a Kelvin-Helmholtz instability is discussed. Hence, this chapter contains elements concerning **Q 1**, **Q 2** as well as **Q 3**.

Ch. 5 describes a case study on turbulence generation by mountain wave breaking. The applicability of the *valve layer* concept to new geophysical conditions is discussed based on a LITOS sounding. Our measurements are augmented by numerical weather prediction using WRF and by idealised numerical simulations using EULAG (**Q 3**).

Ch. 6 deals with the interpretation of a LITOS measurement through a tropopause fold. It investigates turbulence not only as a result of the meteorological conditions, but also as a driver the mesoscale flow in upper-level fronts (**Q 3**).

Ch. 7 summarises the results.

1 Methods and motivation to study atmospheric turbulence

1.1 The effects of atmospheric turbulence

When we consider the effects of atmospheric turbulence, we normally think about the experience of turbulence on a commercial flight. Even though pilot reports are used by other pilots to avoid hazardous areas, turbulence is still the primary cause for injuries in commercial aircraft at cruise altitudes (Sharman et al., 2012). According to Koch et al. (2005) turbulence caused 257 fatalities in the decade from 1990 to 2000. Accordingly, turbulence forecast systems have been developed that use data from numerical weather prediction (NWP) models (Sharman et al., 2006).

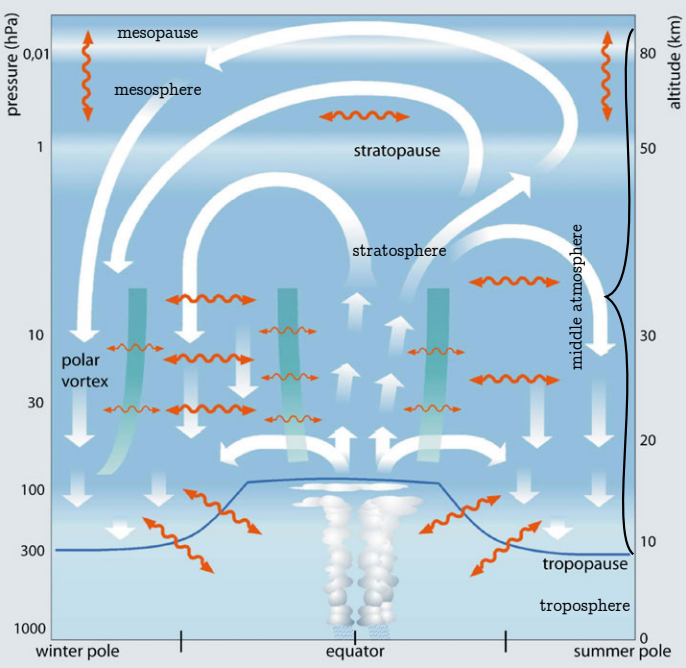

Figure 1.1: Schematics of the Brewer-Dobson circulation from Bönisch et al. (2011)

Furthermore, turbulence plays an important role in atmospheric dynamics where it marks the endpoint of the life cycle of several types of atmospheric waves. Whereas local winds in the atmosphere are highly variable, the residual mean flow (driven by the above mentioned breaking waves) follows a distinct pattern. In the stratosphere and mesosphere, this pattern is called *Brewer-Dobson circulation* (BDC). In the zonal mean picture of the stratosphere it shows an upwelling from the troposphere in the tropics, and a subsequent poleward transport in the stratosphere with a downwelling in polar regions (c.f. Figure 1.1). It has been described by Brewer (1949) based on measurements of the water vapour distribution in the upper troposphere lower stratosphere (UTLS) region and by Dobson and Massey (1956). In the mesosphere the BDC shows an upwelling above the summer pole, a horizontal transport into the other hemisphere and a downwelling above the winter pole. These two main circulations in the middle atmosphere are driven by breaking internal waves, namely by Rossby waves in the stratospheric part and by gravity waves (GWs) in the mesospheric part (e.g. Butchart, 2014). Rossby waves are large scale waves with horizontal wavelengths of several thousand kilometres that form the typical weather patterns with high and low pressure systems in the troposphere.

Their restoring force is based in the conservation of potential vorticity. In the northern hemisphere, Rossby waves always have a westward phase velocity. Therefore, a breaking Rossby wave exerts a westward drag on the mean flow. Due to the Coriolis effect, this leads to a poleward drift in the stratosphere as depicted in Figure 1.1.

As their name suggests, gravity waves are driven by gravity as a restoring force (e.g. Sutherland, 2010). In contrast to Rossby waves they can be excited with arbitrary phase propagation directions. Under the assumption that the vertical wavelength of a gravity wave is much smaller than the vertical scale of variations in the buoyancy frequency N (called *WKB approximation*), the vertical wavenumber of a gravity wave can be expressed as (e.g. Nappo, 2012, 7.24):

$$m = \frac{N}{c - u_0}. \tag{1.1}$$

c denotes the phase speed of the wave and u_0 the background wind speed in the direction of the phase propagation. The buoyancy frequency N describes the frequency at which an air parcel oscillates if it is vertically deflected from its position. It is given as:

$$N = \sqrt{\frac{g}{\Theta}\frac{\partial\theta}{\partial z}} = \sqrt{-\frac{g}{\rho}\frac{d\rho}{dz}}, \tag{1.2}$$

using the gravitational constant g, the potential temperature Θ and the density ρ.

On the other hand the stability of a given flow is described by the Richardson number Ri, which is a function of N and the vertical shear of the horizontal wind $\partial u_\mathrm{h}/\partial z$ (*wind shear*):

$$Ri = \frac{N^2}{\left(\partial u_\mathrm{h}/\partial z\right)^2}. \tag{1.3}$$

If $Ri < 1/4$, the flow is *dynamically* unstable (shear driven instability), whereas it is called *convectively unstable* in the case of $Ri < 0$ (e.g. Fritts and Alexander, 2003). The latter happens if and only if the fluid is unstably stratified ($N^2 < 0$), regardless of the shear.

For high-frequency gravity waves with an internal frequency ω much larger than the Coriolis frequency f, the general dispersion relation simplifies to:

$$\omega^2 = \frac{N^2(k^2 + l^2)}{k^2 + l^2 + m^2} = N^2 \cos^2\alpha \tag{1.4}$$

(e.g. Fritts and Alexander, 2003). (k, l, m) denote the wave vector components and α the angle between lines of constant phase and the vertical. The Coriolis frequency is given by:

$$f = 2\,\Omega_\mathrm{e}\,\sin\phi, \tag{1.5}$$

where Ω_e is the Earth's angular frequency and ϕ the latitude. If gravity waves propagate without breaking, they conserve their pseudo momentum flux. It is given by:

$$\overrightarrow{\mathrm{MF}} = (\mathrm{MF}_x, \mathrm{MF}_y) = \overline{\rho}\left(1 - \frac{f^2}{\omega^2}\right)\left(\overline{u'w'}, \overline{v'w'}\right) \tag{1.6}$$

(Fritts and Alexander, 2003). Overlines denote spatial and temporal averages over at least one wavelength and wave period, while primes indicate wave perturbations compared to this background.

Coming back to the vertical wavelength of a gravity wave ($\lambda_z = \frac{2\pi}{m}$, c.f. Eq. 1.1), we note that whenever c matches u_0 the gravity wave reaches a critical level. I.e. its vertical wavelength approaches zero and Ri becomes very small or even negative. This leads to wave breaking and turbulence production. Due to the zonal mean wind in the stratosphere (eastward in winter, westward in summer), only waves with westward phase propagation in winter and with eastward phase propagation in summer will reach the mesosphere (e.g. Holton and Alexander, 2000). In the mesosphere, they break because their amplitudes grow large due to the decreasing density of the background atmosphere. They thereby exert a westward drag in winter and an eastward drag in summer. As can be seen in Figure 1.1, the Coriolis effect leads to a residual circulation from the summer to the winter pole due to gravity wave drag (GWD). The gravity wave drag is given by (e.g. Kruse et al., 2016):

$$\overrightarrow{\mathrm{GWD}} = -\frac{1}{\rho}\frac{\Delta\,\overrightarrow{\mathrm{MF}}}{\Delta z} \tag{1.7}$$

In other words this means that for dissipating waves the conservation of pseudo momentum flux is violated ($\Delta\mathrm{MF} \neq 0$) and the momentum of the wave is transferred to the background flow (e.g. Sutherland, 2010).

On the other hand, a gravity wave becomes evanescent according to linear theory if $m \to \infty$. For a mountain wave (i.e. $c = 0$), this condition is described by the Scorer parameter (Scorer, 1949):

$$\ell^2 = \frac{N^2}{u_\mathrm{h}^2} - \frac{\partial^2 u_\mathrm{h}/\partial z^2}{u_\mathrm{h}}, \tag{1.8}$$

where u_h is the speed of the horizontal background wind. ℓ is derived from the dispersion relation of two dimentional gravity waves and describes the maximum horizontal wavenumber of a mountain wave above which it becomes evanescent and cannot propagate vertically. This parameter is especially useful for identifying wave ducts: if there is an atmospheric layer showing enhanced ℓ between two regions of lower ℓ, trapped lee waves are likely to form in this layer (e.g. Lane et al., 2000).

Coming back to the large-scale atmospheric circulation, we note that the speed of the Brewer-Dobson circulation is measured by the average time that has passed for an air parcel in a certain region since it left the equatorial tropopause. It is called *age of air* and generally increases with altitude and towards the poles. On average it reaches five years in the polar stratosphere (Butchart, 2014). The resulting mesospheric downwelling above the winter pole and the upwelling above the summer pole leads to temperatures that are far from radiative-convective equilibrium due to adiabatic heating/cooling. In the summer mesopause region these temperature deviations exceed 50 K (Becker, 2012; Holton and Alexander, 2000). But this is not confined to the middle atmosphere. Even in the boundary layer of the atmosphere, temperature deviations from the radiative-convective equilibrium reach 45 K (c.f. Figure 1.2). These results have been obtained with the Kühlungsborn Mechanistic general Circulation Model (KMCM). They highlight the importance of a proper representation of wave and turbulence dynamics in numerical weather prediction.

Furthermore, the middle atmosphere can be understood as an early warning system for climate change, because temperature trends in the summer mesosphere are significantly higher than in the troposphere (Lübken et al., 2013). Of course, models that are used to simulate theses effects should give a correct representation of the dynamics including turbulence effects on the BDC.

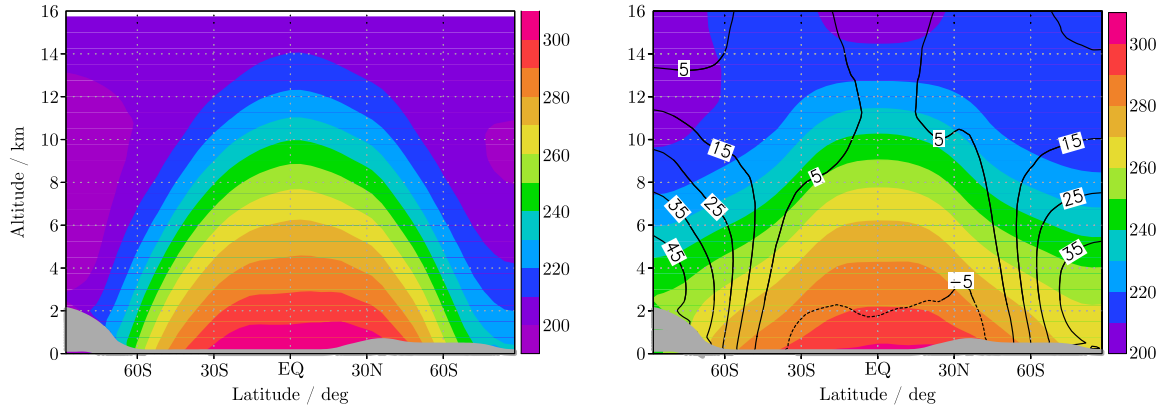

Figure 1.2: Left: Atmospheric annual mean temperature (K) in radiative-convective equilibrium. Right: Annual mean temperature (K) from a climate simulation including waves and turbulence. Temperature differences are shown by black contour lines. Graphics adapted from Becker (16 June 2014).

As mentioned above, the zonal mean circulation of the middle atmosphere is driven by breaking internal waves. In other words, the wave breaking leads to an advection of air parcels. These breaking processes are associated with turbulence production and can therefore be identified by a turbulence resolving instrument like our *Leibniz-Institute Turbulence Observations in the Stratosphere (LITOS)* sensor. As demonstrated in the KHI experiment (c.f. Figure 0.3), the rapid mixing of tracers is an important property of turbulent flows. These mixing processes are indicated by orange double arrows in Figure 1.1. They include primarily horizontal mixing by breaking Rossby waves in the stratosphere and vertical mixing by breaking gravity waves in the mesosphere (e.g. Holton and Alexander, 2000). Furthermore, turbulence accounts for mixing of chemical tracers such as ozone across the tropopause. This often occurs in tropopause folds, where an intrusion of stratospheric air into the troposphere is formed by dynamic processes. This leads to small-scale turbulent mixing (e.g. Holton et al., 1995; Shapiro, 1980). These turbulent mixing processes, however, lead to an increase of the age of air by about 10 % (Dietmüller et al., 2017). Accordingly, turbulence has a twin role in terms of atmospheric circulation: it directly facilitates atmospheric transport by turbulent mixing and it serves as an indicator for wave breaking, which drives the advection of airparcels by the Brewer-Dobson circulation.

Another point where turbulence plays a role is the predictability of atmospheric flows. Generally, it can be said that an enhancement in forecast time of NWP models would be beneficial for human society. These NWP models assimilate various observations such as satellite or radiosonde measurements in order to predict the future state of the atmosphere (e.g. Bouttier and Kelly, 2001). However, Lorenz (1969) realised that these predictions cannot be made for an arbitrary length of time. He states that the range of prediction is not only limited by computational cost, but also by the sensitivity of any future atmospheric state on the current state. This is, because due to the many scales involved in atmospheric flows, any statistical uncertainty on the small scales is transferred to larger scales. Therefore, the error in the prediction of any particular future state of the atmosphere cannot be reduced below a certain limit unless the initial error is zero. Due to measurement uncertainties, however, the initial error cannot vanish. Lorenz (1969) concludes that if his statistical assumptions are correct, "certain turbulent systems, possibly including the earth's [*sic*]

atmosphere, possess for practical purposes a final range of predictability". This underlines that understanding turbulence is an integral part of understanding the Earth's atmosphere.

1.2 Measuring turbulence

This section aims to illustrate a way of determining the kinetic energy dissipation rate ε from turbulent velocity fluctuations measured on a balloon in the troposphere and stratosphere. The description is only carried out as far as it is necessary to follow the concept behind our measurements. For a more detailed analysis the reader may refer to Schneider (2015); Lesieur (2008); Pope (2000); Tennekes and Lumley (1972).

1.2.1 Obtaining kinetic energy dissipation rates

We will focus on a statistical description of fully developed turbulence that is based on a concept developed by Kolmogorov (1941). He provided a mathematical framework for the energy cascade from large to small turbulent scales that is introduced in Richardson (1922) (see also Section 1). More specifically, he described the variation in the strength of velocity fluctuations with changing spatial distance between two measurements. However, we will not follow this so-called *structure function* method here, but use the same theory in the form of a kinetic energy spectrum. Both versions of the theory are interconnected by *Taylor's frozen field hypothesis* that is described below. Based on Kolmogorov's ideas, we divide the kinetic energy spectrum of a turbulent flow into several subranges to determine basic measurable quantities of turbulent flows. These subranges are depicted in Figure 1.3 and will be introduced subsequently. We will present ways to determine the kinetic energy dissipation rate ε from wind velocity fluctuations and discuss their feasibility in terms of an atmospheric measurement on a sounding balloon.

ε describes the rate per unit mass at which kinetic energy is transferred into heat. This transformation happens at scales where inertial forces are of similar magnitude compared to viscous forces. This ratio is described by the Reynolds number (Eq. 0.1). The smallest eddies in a turbulent flow occur at $Re = 1$, because for smaller scales molecular friction dominates and dissipates the kinetic energy. In honour of the findings by Kolmogorov (1941), this length-scale η has been called *Kolmogorov microscale*. After his first similarity hypothesis (Kolmogorov, 1941; Pope, 2000) this scale is only dependent on the dissipation rate ε and on the kinematic viscosity ν by:

$$\eta \equiv (\nu^3/\varepsilon)^{1/4} \tag{1.9}$$

Theoretically speaking, this looks like a promising way to determine ε on a balloon, because the (slowly varying) ν can be determined from a radiosonde measurement. In practical terms however, at an altitude of 15 km ($\nu \approx 10^{-4}\,\mathrm{m^2\,s^{-1}}$) and a typical dissipation rate of $\varepsilon = 10\,\mathrm{mW\,kg^{-1}}$ the Kolmogorov microscale is at ~ 3 mm and the magnitude of the velocity fluctuations is so small that the signal to noise ratio (SNR) of current measurement techniques is insufficient for this approach. Therefore, we need to develop a way of determining ε from velocity fluctuations at larger scales.

For large spatial scales in the same order of magnitude as the size of the turbulent flow L (a jet or a wall-shear flow, for example) the motions will be anisotropic. This is, because they are constrained by the transversal dimension of the flow (e.g. height of the jet or height of the boundary layer). The Kolmogorov (1941) hypothesis of local isotropy states

that scales sufficiently smaller than the size of the flow ($l \ll L$) will be isotropic. In practical terms this means that we only need to measure the fluctuations in one direction (e.g. longitudinally to the main flow), which simplifies the instrumentation.

For spatial scales with $L \gg l \gg \eta$ the second hypothesis of similarity by Kolmogorov (1941) states that the spectrum of velocity fluctuations depends on ε alone and is independent of ν (Kolmogorov, 1941). This spectral range of the turbulent spectrum is called the inertial subrange. From dimensional reasoning it can be shown that the one-dimensional power spectrum of the fluctuations follows

$$W(k) = C_{\mathrm{v}}^2 k^{-5/3} \tag{1.10}$$

(e.g. Pope, 2000; Tennekes and Lumley, 1972). $k = 2\pi/l$ denotes the wavenumber of the fluctuations and

$$C_{\mathrm{v}}^2 = b_{xx} a_{\mathrm{v}}^2 \varepsilon^{2/3} \tag{1.11}$$

the so called structure function constant. b_{xx} is a scaling factor near unity that depends on the direction of the fluctuation measurement with respect to the main flow (A1, Schneider et al., 2017). a_{v}^2 is an empirically determined constant for velocity fluctuations. Even though there is some dispute in the literature about the value of a_{v}^2 (c.f. Schneider, 2015), we will follow Pope (2000); Barat and Bertin (1984); Theuerkauf (2012) and use $a_{\mathrm{v}}^2 = 2.0$. Retrieving energy dissipation rates ε from Eqs. 1.10;1.11 will be named *inertial subrange method* in the following.

Directly resolving the spatial scales l of an atmospheric turbulent flow by a multi-point measurement is technically challenging and therefore rarely done (e.g. Wilczek et al., 2014). As a result, our instrument LITOS (Leibniz-Institute Turbulence Observations in the Stratosphere) is designed to use a single sensor for velocity fluctuations. Therefore, we measure a time series of velocity fluctuations at a single point and relate them to the spatial scales of the flow. This represents Taylor's (1938) frozen field hypothesis. Its main idea is that if the mean speed of the flow $\langle u \rangle$ or the speed of the sensor is large compared to the fluctuation speed u', the turbulent velocity field can be regarded as stationary in a statistical sense with respect to a fixed point measurement. This means that the wavenumber of the turbulent fluctuations can be inferred from the time series of the single point measurement by

$$k = \frac{\omega}{\langle u \rangle}. \tag{1.12}$$

ω denotes the angular frequency of the fluctuations. On a sounding balloon, the mean speed of the flow $\langle u \rangle$ is given by the relative velocity between the balloon and the atmosphere w_{rel}, which can be approximated from the vertical wind w and the ascent rate of the balloon w_{asc} by $w_{\mathrm{rel}} = w_{\mathrm{asc}} - w$. Compared to other in-situ measurement techniques like sounding rockets, balloons show far lower relative velocities w_{rel}. Therefore, the applicability Taylor's hypothesis ($\langle u \rangle \gg u'$) is discussed in more detail below.

In stably stratified environments like the atmosphere there is a large scale limit for the isotropic part of the spectrum, which is often below the size of the turbulent flow L. This is, because the stratification of the fluid will prevent the vertical growth of larger eddies. Accordingly, this critical length scale depends on the buoyancy frequency N. Ozmidov (1965) found the following expression for the scale of the largest isotropic eddies L_0, which

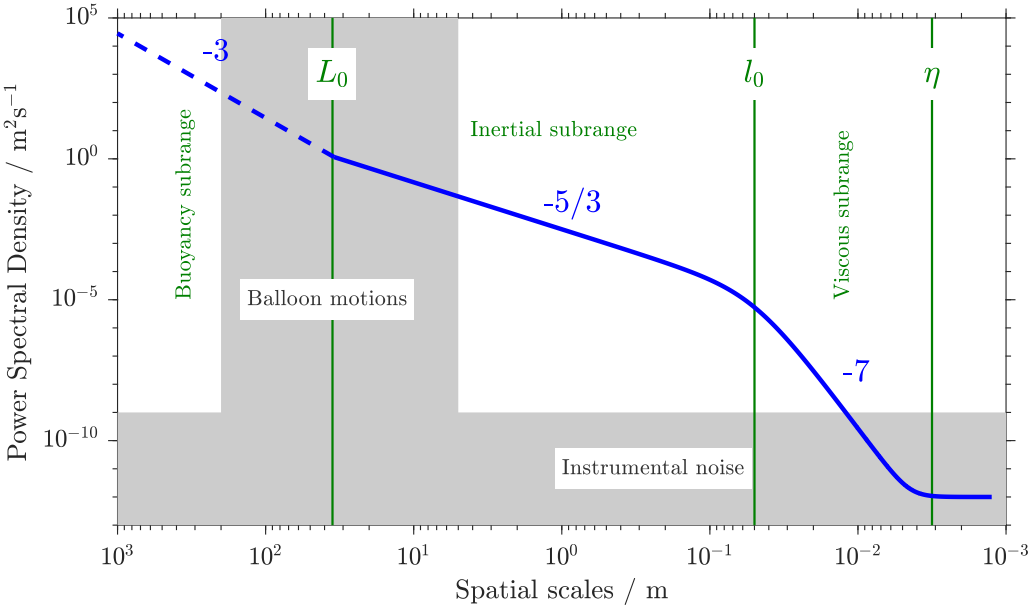

Figure 1.3: Heisenberg spectrum of atmospheric velocity fluctuations in an altitude of 15 km for a kinetic energy dissipation rate of 10 mW kg^{-1}. Grey shaded areas denote parts of the spectrum where the measurement of velocity fluctuations on a balloon is distorted or impossible.

has subsequently been named *Ozmidov Scale*:

$$L_0 = c_{L_0}\sqrt{\frac{\varepsilon}{N^3}} \tag{1.13}$$

c_{L_0} is a constant near unity. Typical spatial scales of the inertial subrange for the troposphere and stratosphere are decimetres to few ten metres. In contrast to the Kolmogorov microscale, the fluctuation-power at these scales is high enough to be measured with commonly used instruments (e.g. constant temperature anemometer; CTA). However, this requires an absolute calibration of the measurement which is difficult to achieve for the relevant pressure and temperature ranges (Xie et al., 2017; Frehlich et al., 2003). Furthermore, the larger scales in the inertial subrange will be subject to self-induced balloon motions that distort the measurement (Barat et al., 1984; Söder et al., 2019).

Therefore, in this study a third approach is used to derive energy dissipation rates. It has been proposed by Lübken (1992) for density fluctuations on sounding rockets and adapted to velocity fluctuations by Theuerkauf (2012) and Schneider (2015). It will be called *inner scale method* in the following. Its main idea is to describe all scales of turbulent motion from the Ozmidov scale L_0 to the Kolmogorov scale η by a common function (Heisenberg, 1948):

$$W(\omega) = C_\mathrm{v}^2 \frac{\Gamma\left(\frac{5}{3}\right)\sin\left(\frac{\pi}{3}\right)}{2\pi w_\mathrm{rel}} \frac{\left(\omega/w_\mathrm{rel}\right)^{-5/3}}{\left(1+\left(\frac{\omega}{\omega_0}\right)^{8/3}\right)^2}. \tag{1.14}$$

The angular frequency $\omega_0 = \frac{2\pi w_\mathrm{rel}}{l_0}$ represents the inner scale l_0 using Taylor (1938)'s frozen field hypothesis (please see Section 1.2.3 for details). l_0 marks the small scale limit of the

inertial subrange. For smaller scales the model assumes a smooth transition to a -7 slope in the so called *viscous subrange* (c.f. Figure 1.3). There are other models that propose slightly different slopes of the spectrum in the viscous subrange. The Tatarskii (1971) model for example fits a double exponential decay instead. However, Lübken (1993) finds that the differences between both models in retrieved energy dissipation rate ε are small compared to other uncertainties on rocket-borne turbulence soundings. Similarly, Strelnikov et al. (2017) reveal that both models yield very close dissipation rates. Accordingly, we will rely on the Heisenberg model, because it is less computationally expensive.

The key point of this method is that the energy dissipation rate ε depends on the inner scale l_0 by (e.g. Schneider, 2015; Tatarskii, 1971):

$$\varepsilon = c_{l0}^4 \frac{\nu^3}{l_0^4}. \tag{1.15}$$

l_0 is acquired by fitting Eq. 1.14 to the time series of the turbulence velocity fluctuations. Most noteworthy is that this method does not depend on a calibration of the measured velocity spectra. Instead, it relies on the spectral slope of the data only. In Eq.1.15 c_{l0} is a constant depending on the type of fluctuations, the direction of the measurement with respect to the main flow and the aforementioned empirical constant a_v^2. In our case, it reads $c_{l0} = 15.8$ (Schneider et al., 2017). The kinematic viscosity of the background flow is calculated according to the US Standard Atmosphere 1976 (NOAA, 1976) from the temperature T and the density ρ by

$$\nu = \frac{1.458 \cdot 10^{-6} \cdot T^{3/2}}{\rho(T + 110.4)}. \tag{1.16}$$

As stated above, Eq. 1.14 depends on the applicability of Taylor's frozen field hypothesis. Namely, this approach is only valid if $\langle u \rangle \gg u'$ (e.g. Taylor, 1938; Wyngaard and Clifford, 1977). Wilczek et al. (2014) estimate from a theoretical model that the error of the structure function constant C_v will be below 5 %, if the turbulence intensity $\xi = \frac{u'}{\langle u \rangle}$ is below 30 %. The characteristic velocity of the turbulent fluctuations u' at a specific scale l can be calculated from $u' = \sqrt{k\,W(k)}$ (e.g. Tennekes and Lumley, 1972, p. 260). Here, $k = 2\pi/l$ denotes the wavenumber of fluctuations with wavelength l. For a turbulence measurement on a sounding balloon we therewith find for the turbulence intensity in the flow around the sensor (using Eq. 1.10):

$$\xi = \frac{\sqrt{b_{xx}}\, a_\mathrm{v}}{w_\mathrm{rel}} \left(\varepsilon \frac{l}{2\pi} \right)^{1/3}. \tag{1.17}$$

In the case of the LITOS sensor, which is sensitive in the direction of the main flow and one perpendicular direction, Schneider et al. (2017) found $b_{xx} = 7/3$.

Generally, our procedure to retrieve ε using the *inner scale method* is the following:

- Divide raw data into time bins of a few seconds.
- Compute the PSD $W(\omega)$ from each raw data bin and fit Eq 1.14 to the data. The fit will have two degrees of freedom: A calibration constant χ and the inner scale l_0.
- Calculate the energy dissipation rate from l_0 with Eq 1.15.
- Apply certain quality control criteria for the fit and discard all measurements of ε from altitude bins where one of these criteria is not met.

A more explicit description of the fit procedure as well as the quality control criteria will be given in Section 2.3.

As mentioned above, the most important advantage of the *inner scale method* compared to the *inertial subrange method* is that the wind-fluctuation measurement does not need to be calibrated. Furthermore, the measurement can be constrained to spatial scales below a few metres, thereby avoiding the influence of self-induced balloon motions and limitations to Taylor's frozen field hypothesis due to high turbulence intensities. The disadvantage is that compared to measurements resolving the inertial subrange only, we need an enhancement in the SNR by a factor of at least 10. This is, because we need to resolve at least two orders of magnitude in PSD of the viscous subrange for a reliable determination of l_0 from the fit. Accordingly, it is vital for our measurements to choose a sensitive measurement method for velocity fluctuations and to sufficiently suppress the instrumental noise. This is discussed in Section 2.

Generally, the turbulent kinetic energy dissipation rate ε is a good measure to describe the strength of atmospheric turbulence as it directly represents the amount of kinetic energy dissipated into heat. The impact of turbulence on aircraft however, is proportional to the vertical acceleration of the plane. Sharman et al. (2012) argue that the vertical acceleration is proportional to the cube root of ε. Therefore, the *eddy dissipation rate* $\mathrm{EDR} = \varepsilon^{1/3}$ is used as a measure for the impact of turbulence on aircraft (Sharman et al., 2012, 2014; Sharman and Pearson, 2017). Sharman et al. (2014) finds from acceleration measurements on commercial aircraft that the EDR for *light*, *moderate* and *severe* turbulence is 0.1[1], 0.21 and 0.47, respectively. These values denote measured median values of peak EDR during times when the pilots reported the respective turbulence strength. They are valid for medium sized aircraft. Even though aircraft related turbulence detection is not the focus of our institute, we adopt this classification to allow for easier comparison with other reports, because these measures are widely used in the community.

1.2.2 Calibrating wind fluctuation measurements

As mentioned above, obtaining ε from Eqs. 1.10;1.11 would require a calibration of the CTA wind fluctuation measurement. On a CTA, the measured quantity is the resistance of the wire, which is connected to the heat flux across the sensor surface. This heat flux in turn is equivalent to the convective heat transfer h, because radiative heat transfers can be neglected.

For many applications, however, the calibration of a CTA is not done in terms of the convective heat transfer, but in terms of Nusselt number versus the velocity of the flow. Generally, the Nusselt number is a function of the Reynolds number Re, the Prandtl number Pr and the Knudsen number Kn. It denotes the ratio of convective to conductive heat transfer:

$$Nu(Re, Pr, Kn) = \frac{h\,l}{k}. \tag{1.18}$$

However, as the influence of the Prandtl number on the forced convection from a cylinder is weak, we assume $Nu(Re, Pr, Kn) \approx Nu(Re, Kn)$ (Xie et al., 2017). h is the convective heat transfer coefficient of the flow, $l = 5\,\mu\mathrm{m}$ the characteristic length scale given by the diameter of the sensing wire and k the thermal conductivity of the fluid. In the context of

[1] Sharman et al. (2014) write EDR = 0.01. From their figures and from other literature however, I assume that this is a typo and use EDR = 0.1.

this work, all thermal conductivities have been calculated according to Lasance (2002). An overview on different experimentally obtained thermal conductivities is given by Kadoya et al. (1985). The Knudsen number is a dimensionless number that classifies the rarefication of a flow:

$$Kn = \frac{\lambda}{l} \tag{1.19}$$

There are slightly differing definitions of Kn (e.g. Bird, 2003). However, in order to keep our considerations simple, we will use the one given here. λ is the mean free path in the gas. It denotes the average distance a molecule travels between collisions. It is given by:

$$\lambda = \frac{R\,T}{\sqrt{2}\,\pi\,d_a^2\,N_A\,p} \tag{1.20}$$

R denotes the universal gas constant, N_A the Avogadro constant, d_a the collisional cross section and p the pressure of the gas. Further information on the characteristics of rarefied flows can be found in Bird (2003) and Colin (2004). For a more specific discussion of CTA measurements in rarefied flows, please see Section 2.5.

The general measurement parameter on CTA soundings is the voltage drop across the sensor V_s. According to Hugo et al. (1999) it is given by:

$$V_\mathrm{s} = \sqrt{Nu\,\pi\,k\,L(T_\mathrm{s} - T_\mathrm{a})\,R_\mathrm{s}}. \tag{1.21}$$

L is the length of the sensing wire, $T_\mathrm{s} - T_\mathrm{a}$ denotes the temperature difference between the sensor and the ambient flow (called *overtemperature*) and R_s the resistance of the sensor. The Nusselt number depends on the Reynolds number and therefore on the flow speed, because the convective heat transfer coefficient h is a function of velocity. Namely, the functional relation depends on the cross sectional shape of the wire. For cylindrical wires as used on most CTAs King (1914) proposed a functional dependence that is now known as *King's law*:

$$Nu = a + b\,(Re)^n. \tag{1.22}$$

a, b and n denote empirical constants that need to be determined in a calibration fit. This results in the following relation for the flow speed u from a CTA measurement (Hugo et al., 1999; Frehlich et al., 2003):

$$u(t) = \frac{1}{\rho\,b^{1/n}}\left(\frac{V_\mathrm{s}(t)^2}{T_\mathrm{s} - T_\mathrm{a}} - b\right)^{1/n} \tag{1.23}$$

These relations, however, do not take into account a rarefication of the flow and can therefore be applied only when $Kn << 1$. For a free molecular flow with $Kn >> 10$, Gai (1977) presented a calibration for CTA measurements. In the transitional flow regime ($0.1 < Kn < 10$), however, the only published CTA calibration known to us is by Xie et al. (2017). They did not attempt to develop a mathematical model based on the description of the physical processes involved in such a measurement. Instead, they used the above mentioned assumption that the Nusselt number can be described as a function of the Reynolds number and the Knudsen number. Consequently, they used a nonlinear least squares algorithm to determine the coefficients of the nonlinear regression analysis of their experimental data taken in an open-circuit wind tunnel. However, this type of calibration is not available for the LITOS sensor so far. Nevertheless, we carried out a cross comparison with the HYFLITS instrument that uses such a calibration to retrieve kinetic energy dissipation rates from the small scale part of the inertial subrange (Chapter 4).

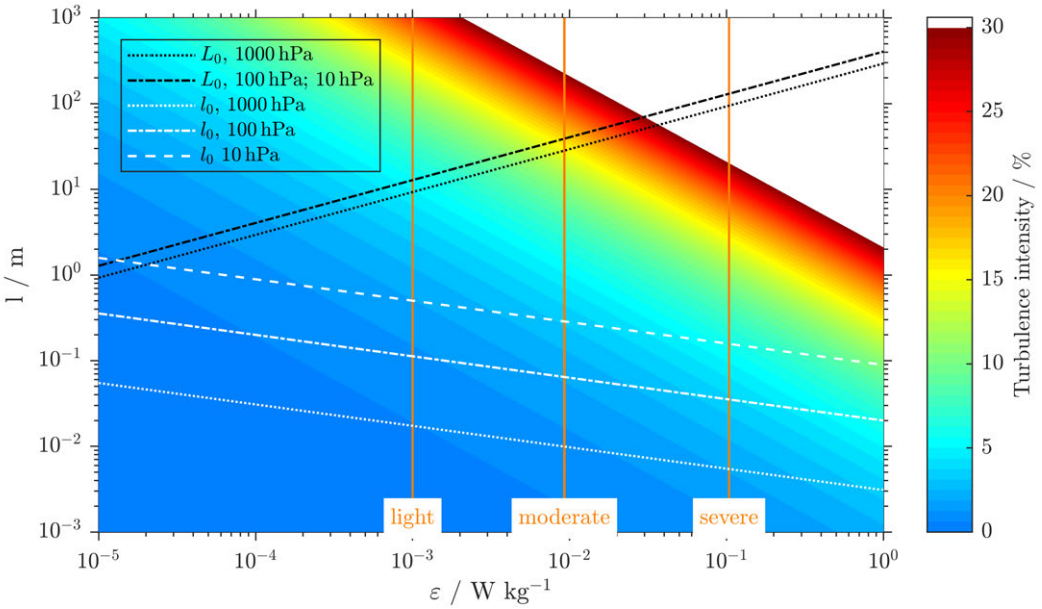

Figure 1.4: Turbulence intensity ξ for a typical balloon turbulence sounding ($w_{\mathrm{rel}} = 5\,\mathrm{m\,s^{-1}}$) as a function of the kinetic energy dissipation rate ε and the length scale of the flow l. Critical turbulence intensities above 30 % are marked by white colour-shading. For comparison, aircraft standards for turbulence strengths are shown by orange lines (Sharman et al., 2014). The outer scales for 100 hPa and 10 hPa are so close, that their lines cannot be separated in the scaling of this plot.

1.2.3 Taylor's frozen field hypothesis

In Figure 1.4, the turbulence intensity of the flow around the LITOS sensor is shown for $w_{\mathrm{rel}} = 5\,\mathrm{m\,s^{-1}}$. Wilczek et al. (2014) show that for $\xi > 30\,\%$, the bias of the PSD estimate in the inertial subrange is larger than 5 %. Therefore, corrections would be needed for the dissipation rate retrieval. Accordingly, all areas where such a correction would be required are marked by white colour-shading in Figure 1.4. In order to evaluate the relevance of these effects for different turbulence retrievals, we plot the inner scale l_0 (Eq. 1.14) and the outer scale of turbulence (Eq. 1.13), each for different pressure levels. The buoyancy frequency and the kinematic viscosity underlying these data have been acquired using data from CIRA-86 for 50 °N (Fleming et al., 1990).

We note that even for extreme turbulence events with dissipation rates of up to $1\,\mathrm{W\,kg^{-1}}$ Taylor's hypothesis is accurate for the inner scale of the flow l_0 in typical altitudes where sounding balloons are operated. It is also visible however, that it is not unconditionally valid for the outer scale L_0 in the case of higher than *moderate* dissipation rates. This is especially important when obtaining ε from the structure function constant in the large scale part of the inertial subrange (bounded by L_0, Eq. 1.10), because in this method the retrieved dissipation rate directly depends on the calibration of the PSD estimate.

2 Instrumentation

2.1 The LITOS instrument

As its name suggests, Leibniz-Institute Turbulence Observations in the Stratosphere (LITOS) is an instrument designed to measure the turbulent kinetic energy dissipation rate ε from the ground to the lower stratosphere. Generally, these altitudes can be reached by unmanned balloons as well as by unmanned aerial vehicles (UAV). The latter have been used for atmospheric turbulence soundings, for example by Podglajen et al. (2017). However, the former combines significantly lower operational cost with a lower airspeed, thereby enhancing the resolution of the measurement. Therefore, we use sounding balloons as a platform for our LITOS instrument. These balloons (TOTEX, TX 3000) are made of rubber and have a typical lifting capability of a few kilogrammes. Earlier turbulence measurements have been carried out on floating balloons as well as on rising balloons (e.g. Barat, 1982; Barat and Genie, 1982; Theuerkauf et al., 2011; Clayson and Kantha, 2008). Rising balloons, however, create a wake downstream of the balloon that may significantly disturb the measurements on the gondola (Barat et al., 1984; Kräuchi et al., 2016; Söder et al., 2019). These wake related influences on turbulence measurements will be discussed in Chapter 3. Here we describe the current version of the LITOS instrument, which provides wake free measurements of turbulent velocity fluctuations on a descending balloon.

An overview of the *payload chain* (consisting of all payload boxes suspended below the balloons) is given in Figure 2.1. It is lifted by two balloons at an ascent rate of $\sim 5\,\mathrm{m\,s^{-1}}$. During flight, the actual position of the instrument is measured using the Global Positioning System (GPS) and transmitted to the operator via Iridium communication. This is done with the stand alone unit 9602-A from NAL Research Corporation. It is connected to the electronics, custom made by IAP, that allow the operator to trigger pyrotechnical cable cutters via the Iridium uplink.

As mentioned above, measurements on sounding balloons are commonly carried out in the ascent phase. In order to avoid any wake influences however, we measure in the descent phase (c.f. Chapter 3). Accordingly, we cut away the lifting balloon with *cutter 1* when it has reached about 90 % of its predicted top altitude. The amount of lifting gas in the descent balloon is calculated such that it leads to a constant descent rate of $\sim 5\,\mathrm{m\,s^{-1}}$. This is the measurement phase, where LITOS records turbulence data. During this phase, the parachute remains closed, because there is still tension on the cord between the parachute and the payload. A few hundred metres above ground the descent balloon is cut away by the operator. This releases the tension from the string, the parachute opens up and the payload touches down at a vertical speed of about $4\,\mathrm{m\,s^{-1}}$.

The LITOS payload consists of two Constant Temperature Anemometers (CTAs). Their sensors are mounted below the LITOS gondola to ensure that they measure within the free atmosphere unperturbed by the wake of any part of the payload during descent (c.f. Figure 2.1). The radiosonde is mounted upside-down in between the LITOS box and the balloons. This is done to keep the flow around the instrument as similar to a conventional ascent measurement as possible.

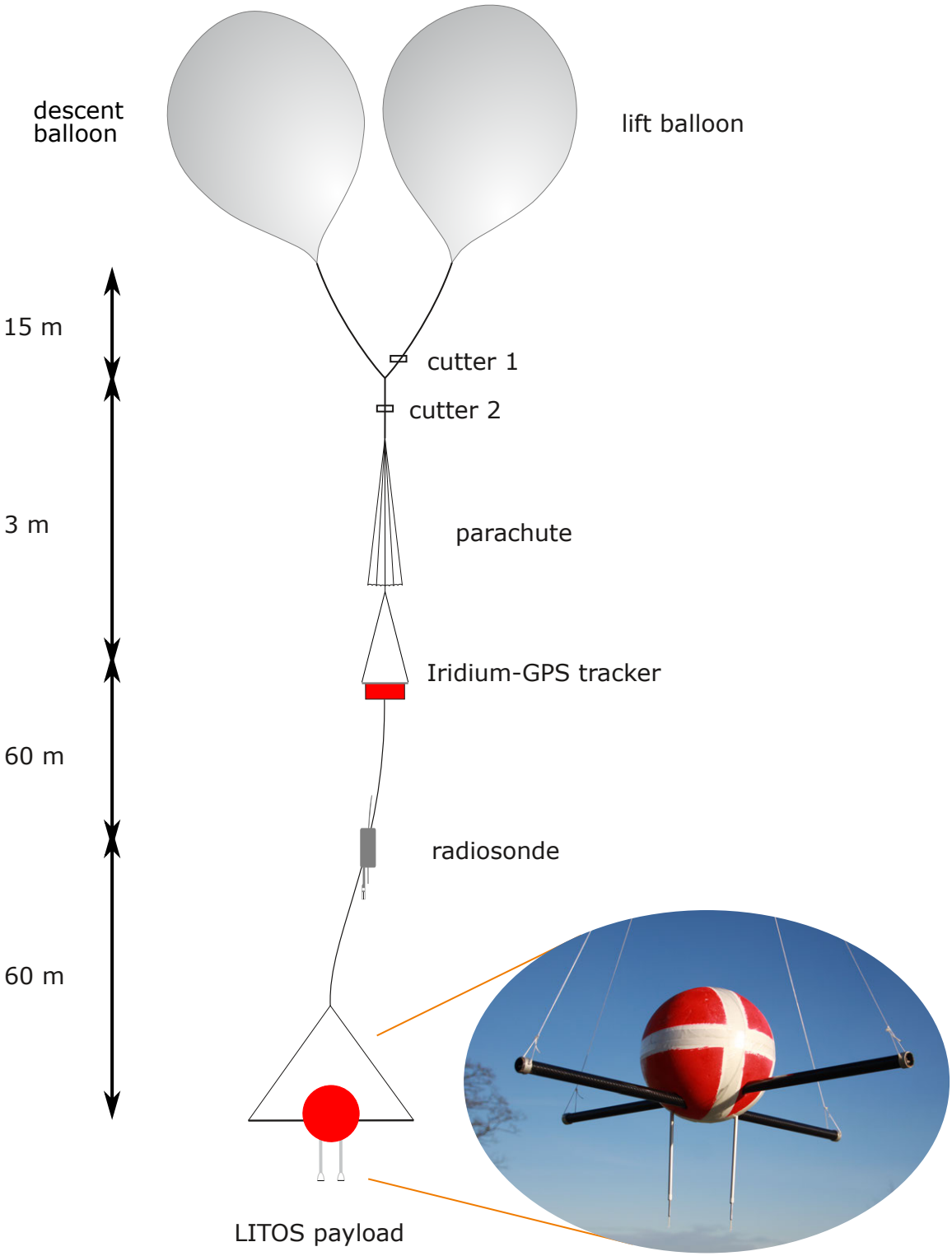

Figure 2.1: LITOS payload

The LITOS payload is made of a polystyrene sphere (30 cm in diameter). It is mounted on two carbon composite rods that increase the lever arm and therefore suppress tilting motions of the gondola. The sensors are mounted 25 cm below (upstream on downleg) the gondola. The sensors (Dantec 55P01) are each connected to a separate Wheatstone bridge (Dantec 54T42). This bridge produces an analogue output signal that is related to the airspeed around the sensor by King's law (King, 1914). It is subsequently digitized using an analogue-digital converter (Analog Devices AD7608) at a sampling rate of 16 kHz and a resolution of 18-Bit. Furthermore, the data acquisition electronics (custom made at IAP) record housekeeping data like time and supply voltages. Additionally, the movements of the gondola and the airpressure are recorded by an inertial sensor (Analog Devices ADIS16407). The reconstruction of the gondola movements from the sensor data has been developed by Schneider (2015, Ch. 3.3). In the most recent version of the payload, all data are stored on an SD-card. Previously, a telemetry system developed in cooperation with Argus Electronic GmbH was used to downlink the data to a ground station. However, this development has been discontinued due to interference problems between the transmitter and the CTA sensors.

Generally, the CTA-signal is a function of air density, air temperature, wire temperature and humidity (if the latter is not negligible, see Theuerkauf, 2012). Frehlich et al. (2003) use a modified version of King's law and find for the calibrated velocity $U(t)$ of a CTA:

$$U(t) = \frac{1}{\rho\, d^{1/n}} \left[\frac{X(t)^2}{T_\mathrm{w} - T} - c \right]^{1/n} . \tag{2.1}$$

$X(t)$ is the CTA output signal, $T_\mathrm{w} - T$ the temperature difference between the hot-wire and the ambient air and ρ the air density. c, d and n denote empirically determined calibration constants. For an exemplary measurement in the boundary layer, Frehlich et al. (2003) find $c = 1.02 \cdot 10^{-2}$, $d = 4.4 \cdot 10^{-3}$ and $n = 4.6 \cdot 10^{-1}$. Eq. 2.1 implies that the anemometer signal is reduced with decreasing pressure. Within the troposphere, this effect is counteracted by the decreasing temperature. In conclusion, the SNR of a CTA slightly decreases in the troposphere and far more rapidly thereafter (data not shown here). This increases the lower turbulence detection limit of the LITOS instrument (see Section 2.5 for more details). Generally, such a calibration for the relevant density and temperature ranges is difficult to obtain (Theuerkauf, 2012). However, recently Xie et al. (2017) was able to obtain a calibration using a temperature controlled pipe flow fed from bottled gas streaming into a vacuum chamber. This type of device is not available to us at the moment. However, a comparison with an instrument using this technique is presented in Chapter 4.

2.2 The Leibniz-Institute flightpath forecast (LIFF)

For a safe operation of LITOS, a flightpath prediction is needed in order to avoid landing in densely populated areas or on sea. The latter has to be avoided, because the lack of a telemetry system makes payload recovery mandatory. Our flightpath prediction system is called LIFF. It uses GFS[1] or WRF[2] data to calculate the flightpath of the balloon as a passive tracer through the wind field. The resulting flightpath is exported to a Google Earth

[1] Global Forecast System, https://www.emc.ncep.noaa.gov/index.php?branch=GFS (Last accessed: 26/11/19)

[2] Weather Research and Forecasting, https://www.mmm.ucar.edu/weather-research-and-forecasting-model (Last accessed: 26/11/19)

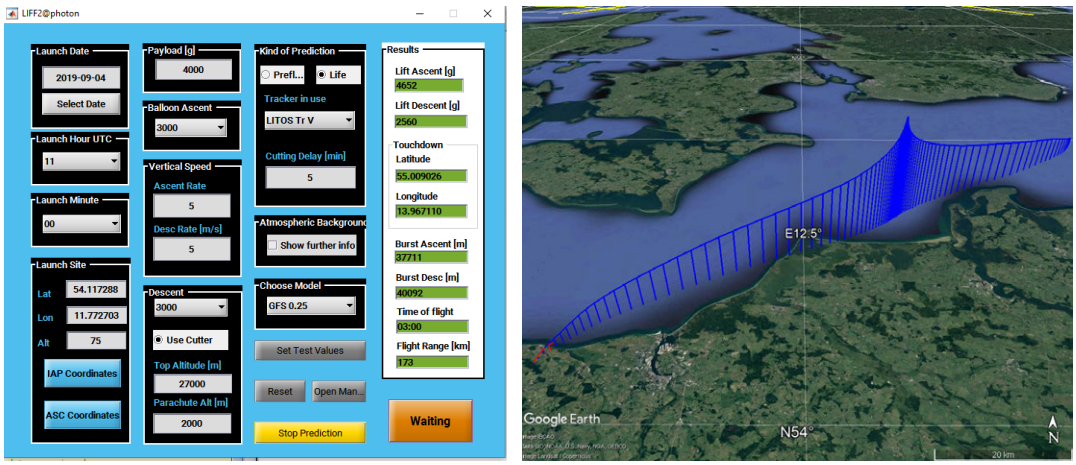

Figure 2.2: Leibniz-Institute flightpath forecast (LIFF). Left: GUI set for a life prediction. Right: predicted flightpath for a normal ascent in blue, flightpath if cutter is operated at the earliest possibility in red.

readable file. The user interface of our software and an exemplary flightpath prediction are shown in Figure 2.2. The precursor version has been described by Söder (2014, Section 3.3). A description of the mathematics behind the tool and an evaluation of its performance can be found there. Within the course of this thesis, the functionality of this software has been extended by the features shown in Table 2.1.

To summarise, we state that incorporating the double balloon technique into our flightpath forecast makes the operation much smoother. In particular, the development of the life forecast significantly enhances the safety of the operation. If there are imperfections in the prediction due to an imprecise balloon filling, for example, the operator can immediately see the consequences of cutting the balloon away at all times. This clearly reduces the risk of landing in a populated area.

2.3 Introduction to the turbulence retrieval scheme

In this section, a brief introduction to the turbulence retrieval scheme used for the LITOS data is given. For further information, please see Schneider (2015). Here, the current version of the retrieval scheme is depicted. The changes that have been made in the course of this thesis will be presented in Section 2.4.

As outlined in Section 1.2, our turbulence evaluation is based on dividing the CTA data into time bins of a few seconds. In the most recent version of the retrieval we use data segments of 5 s in length. Such a time bin from an altitude range where turbulence was present is seen in the left panel of Figure 2.3. In a next step the DC-offset is removed from the time bin and the data are tapered using a Blackman-Harris window in order to suppress spectral leakage. From these modified raw data, a PSD is estimated using a procedure similar to Welsh's method (details are described in Section 2.4.2). From that power spectrum, the instrumental noise level is detected and subtracted (result in right panel of Figure 2.3). This is done because the instrumental noise would change the curvature of the atmospheric spectrum at the small scale end. However, it leads to data gaps on spatial scales smaller than the fit range (irrelevant for our retrieval). They occur, because subtracting an aver-

Feature	Function	Method
descent on balloon	• calculate lift of both ascent and descent balloon	• take drag coefficient from balloon manufacturer and use root-finding to get nozzle lift for both balloons
life prediction	• use tracker position to run forecast for regular flight from current balloon position (Figure 2.2, blue)	• regularly check for new position, check if balloon is already on descent
	• show flightpath prediction if cutter is operated at earliest convenience (Figure 2.2, red)	• only use parachute for descent
use different models	• increase robustness of prediction by comparing different wind models	• incorporate WRF predictions to be used on a campaign basis and different versions of the GFS model for regular forecasts
error handling	• implement warnings against unsafe user inputs	• e.g. intercept too high ascent or descent rates that may flip over descent balloon

Table 2.1: Improvements to the Leibniz-Institute flightpath forecast (LIFF).

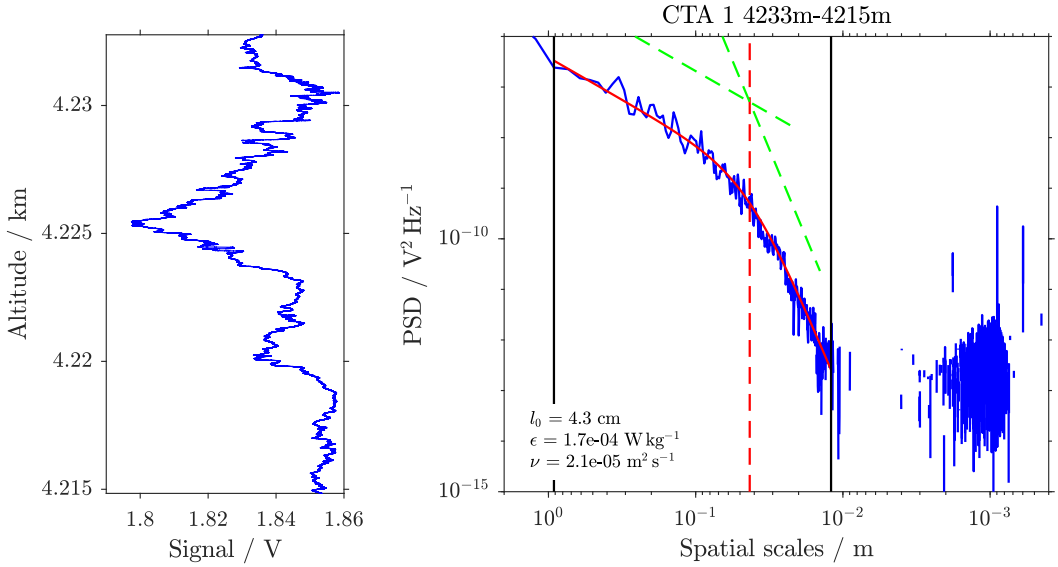

Figure 2.3: Evaluation of a turbulent altitude range. Left: raw data signal from this 5 s time bin. Right: PSD from raw data of left panel (blue), fit following Equation 1.14 (solid red), inner scale l_0 (dashed red), fit range (solid black) as well as slope of inertial ($-5/3$, light green) and viscous subrange (-7, light green). ε denotes the retrieved energy dissipation rate and ν the kinematic viscosity.

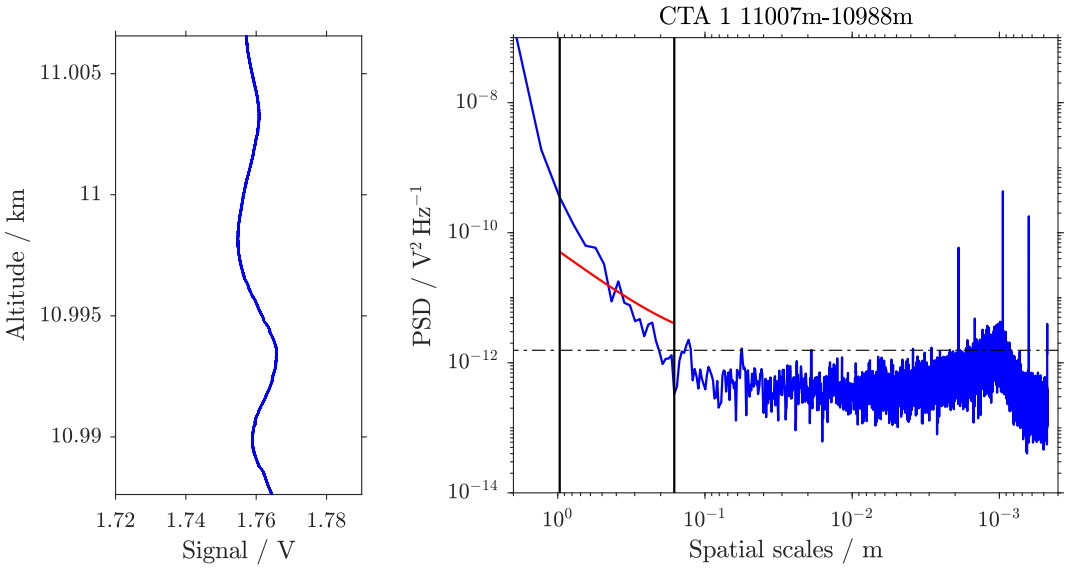

Figure 2.4: Same as Figure 2.3, but for a non-turbulent altitude range. Noise level not subtracted and marked by dashed-dotted black line.

age noise level leads to negative PSD values that are non-physical. Next, the Heisenberg spectrum of turbulence is fitted to the spectrum using the absolute level of the PSD χ and the inner scale l_0 as free parameters (Eq. 1.14). l_0 is the desired fit parameter because, together with the kinematic viscosity, it determines the kinetic energy dissipation rate ε (Eqs. 1.15; 1.16). As mentioned in Section 1.2, the result from fitting χ is not used in the retrieval, because there is no calibration of the CTA available on the LITOS instrument.

This procedure is done for each time bin. The next step is to discriminate turbulent from non-turbulent time bins. In order to visualise the difference in spectral shape, a non-turbulent time bin is shown in Figure 2.4. In the raw data much less small scale fluctuations are visible compared to the turbulent altitude bin shown in Figure 2.3 (same scaling range in both figures). The remaining fluctuations are caused by the internal oscillations of the balloon (c.f. Section 2.6.2). The power spectrum shows rapidly declining power with increasing frequency, which is mainly influenced by the tapering window. For a discussion of the noise, please see Section 2.4.1. There is no resemblance between this spectrum and the spectrum of atmospheric turbulence shown in Figure 1.3. Accordingly, the fit fails (detected l_0 is outside of the fit range). However, there are other cases where the fit does not fail, but the estimated dissipation rate is unreliable because of bad fit quality. Based on Schneider (2015) and Schneider et al. (2017), we use the following criteria to discriminate truly turbulent altitude bins:

1. The noise level detection must not fail.
2. The fitting routine has to terminate.
3. The width of the fit range (marked by solid black lines in Figure 2.3) has to be at least one order of magnitude.
4. The outer scale l_0 has to be within the fit range.

5. The root mean square distance between the data and the fit must not be larger than 0.3 orders of magnitude.

6. The slope at the small scale end of the fit range has to be at least -4.

The reason for the first two criteria is evident. For further information on the noise level detection scheme, please see Section 2.4.2. A criterion for the minimal width of the fit range is introduced because in some cases the roll-off from the tapering window may produce slopes that could be mistaken for a spectrum of atmospheric turbulence. The fourth point is needed, because the fitting algorithm may even detect cases, where l_0 is expected to be outside the fit range (the spectrum shown in Figure 2.4 is one of them). However, we do not consider this as a reliable basis for estimating ε and therefore discard these cases. The fifth criterion sorts out cases where the fit does not match the spectrum properly. The last criterion is meant to sort out cases, where l_0 is very close to the small scale end of the spectrum and the viscous subrange is hardly resolved at all. This especially occurs with the older data acquisition electronics (c.f. Section 2.4.1). We do not regard those cases as reliable estimations of the dissipation rate and therefore discard them.

For further information on the detection limit of our instrument, please see Section 2.5. Overall, our methodology does not allow to clearly identify an altitude range as non-turbulent. Instead, we identify those regions that are certainly turbulent and determine their kinetic energy dissipation rate ε.

2.4 Improvements for a more reliable turbulence retrieval

In this section the most relevant changes to the electronics and to the turbulence retrieval scheme are discussed. In the first place, the need for the developments carried out in the course of this thesis shall be demonstrated using Figure 2.5.

In the left panel of this figure, a turbulent PSD from one of the flights during the combined METROSI/GW-LCycle II campaign from January 2016 is shown. It is calculated from a 5 s long data sample in the lowermost third of the measurement around 7 688 m altitude. This time bin is a typical example of a low turbulence strength measurement ($\varepsilon = 2.2{\cdot}10^{-4}\,\mathrm{W\,kg^{-1}}$). Due to the decreasing SNR of the instrument, it resembles measurements of larger dissipation rates in higher altitudes. It is clearly visible that the data hardly resolve the viscous subrange. In total the fit range spans 3.8 orders of magnitude in PSD. However, only 0.53 orders of magnitude are located in the viscous subrange. Accordingly, the kink between the inertial and the viscous subrange is badly resolved and this spectrum would be sorted out by the sixth quality control criterion from Section 2.3. In the course of this thesis, this issues has been resolved by increasing the SNR. In a similar geophysical situation, the recent version of the LITOS instrument spans 4.9 orders of magnitude in PSD of which 2.6 orders are in the viscous subrange (right panel of Figure 2.5). This spectrum allows for a reliable determination of the energy dissipation rate.

2.4.1 Improvements to the electronics

This improvement in SNR has mainly been achieved by reducing the noise level of the instrument. Originally, LITOS used a 16-bit analogue-digital converter (*ADC*, Analog Devices AD7606). The CTA-output (Dantec 54T42) was low-pass filtered by a built-in filter of the CTA with a cut-off frequency of 10 kHz. At a sampling frequency of $f_s = 8$ kHz,

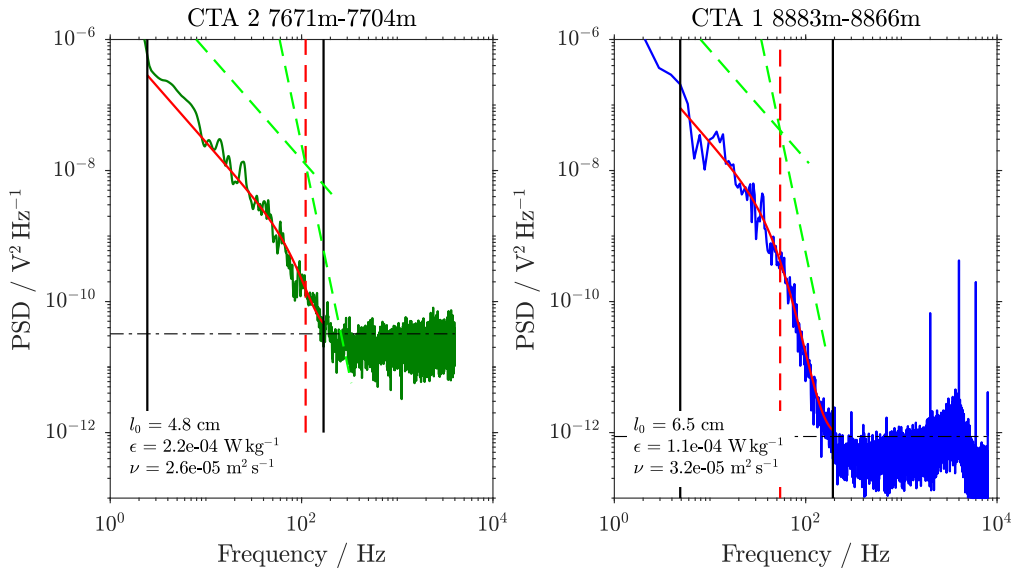

Figure 2.5: Same as right panel of Figure 2.3, but without subtracting the noise level and using frequency on the x-axis. Left: Turbulent spectrum from 16 Jan 2016 i. Right: Turbulent spectrum from 14 Nov 2018 featuring all changes made to the electronics and the data acquisition scheme in the process of this thesis. The spikes in the kHz range are caused by another electronics that was flown on the same balloon.

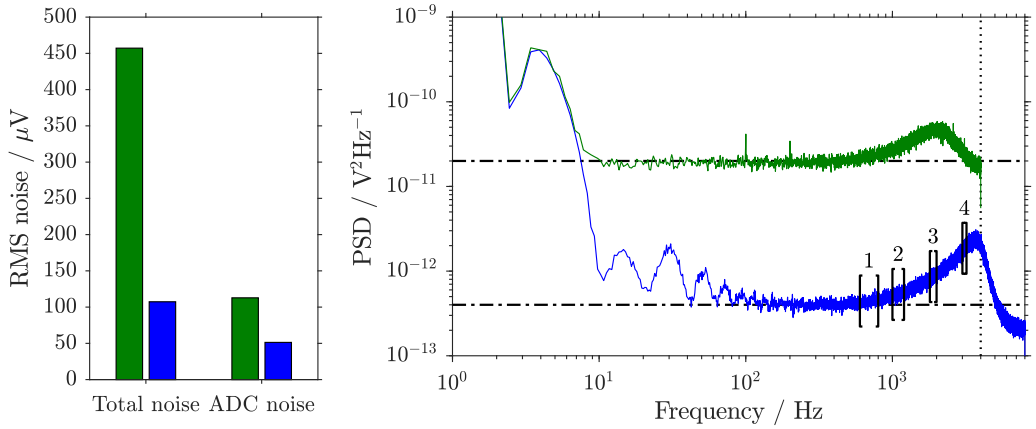

Figure 2.6: Green: old data acquisition electronics (f_s = 8 kHz, 16-Bit). Blue: new data acquisition electronics (f_s = 16 kHz, 18-Bit, including anti-aliasing filter and oversampling). Left: RMS of electronics noise. Right: PSD of electronics noise. Dashed-dotted lines: noise levels. Dotted line: cut-off frequency of the anti-aliasing filter. Frequency ranges of the new data noise level detection algorithm shown by black brackets.

this violates the Nyquist-Shannon sampling theorem, because input signals $f > f_s/2$ may occur. The noise of this configuration can be seen from the green curve in Figure 2.6.

Accordingly, a custom-built low pass filter has been added to our electronics between the CTA and the ADC. The goals were to achieve a steep roll-off of the filter transfer function, an easy integration in the existing data acquisition system and to avoid ripple in the transfer function of the filter, because they would disturb the spectral evaluation of the CTA signal. These purposes are well served by a Butterworth filter. For the LITOS system we combine two active fourth-order filters (Linear Technology LTC1563-2) that are mounted on a separate hook-up board connected to the previous data acquisition electronics. The power supply is realised using a separate 7.2 V battery pack and a drop-out regulator to avoid interferences from the digital part of the data acquisition. According to the data sheet, this yields a filter roll-off at -160 dB per decade. The cut-off frequency is 4 kHz.

In order to avoid aliasing due to noise above the Nyquist frequency, the sampling rate of the ADC has been doubled from 8 kHz to 16 kHz. Furthermore, we noticed that in the old configuration with the AD7606 converter, the quantisation noise made up a significant amount of the total noise. Therefore, it was decided to use an 18-bit converter Analog Devices AD7608. This reduced the quantisation noise significantly (data not shown). However, each filter unit itself produces a noise of $\sim 50\,\mu\mathrm{V_{RMS}}$. This is counteracted by using an internal eightfold oversampling of the ADC that acts like digital anti-aliasing filter with a cut-off frequency of 5 kHz.

This reduces the RMS value of noise from the data acquisition electronics from $110\,\mu\mathrm{V_{RMS}}$ to $50\,\mu\mathrm{V_{RMS}}$ (c.f. left panel of Figure 2.6). The combined noise of the CTA in operation (zero wind conditions) and the ADC is reduced from $460\,\mu\mathrm{V_{RMS}}$ to $110\,\mu\mathrm{V_{RMS}}$. From the right panel of Figure 2.6 it can be seen that the noise in the relevant frequency range of the PSD (between 1 Hz and 500 Hz, c.f. Figure 2.3) has been reduced by more than 1.5 orders of magnitude. Please note that the peak in the spectrum around 4 Hz and its higher harmonics are caused by the stronger smoothing of the spectrum compared to a usual LITOS evaluation as seen in Figure 2.5. Generally, the new data acquisition electronics in particular shows an increase in PSD at frequencies above 500 Hz until the signal is reduced by the anti-aliasing filter. This peak is caused by the analogue CTA electronics and cannot be avoided without a complete redesign of the instrument. However, this does not influence the data retrieval as described in Section 2.4.2.

Overall, these changes reduce the noise level of the electronics and allow us to measure weaker turbulence than before, as it is shown in Figure 2.5. Furthermore, possible influences of high frequency distortions on the energy dissipation rate estimate are reduced, because a larger part of the viscous subrange is resolved.

2.4.2 Improvements to the retrieval scheme

In general, the data retrieval schemes follows Schneider (2015). However, we have made some changes in order to increase the robustness of the algorithm. They shall briefly be presented in the following.

Schneider (2015) obtained the **periodogram** $W(\omega)$ by removing a linear trend and using a Hann window to avoid spectral leakage. $W(\omega)$ is denoised using a running average over 31 datapoints. In the current version, we use a Blackmann-Harris window as tapering function because it further suppresses spectral leakage. The slightly reduced frequency resolution is of subordinate importance in our case. Due to the non-equidistant datapoints of the PSD on the logarithmic frequency axis, the running average in the frequency domain leads to

a slight change in the curvature of the data. Therefore, we decided to use a periodogram estimate similar to Welsh's method. The basic idea is to subdivide each 5 s time bin into sub bins that are averaged to reduce the noise. In the current version of our retrieval the width of a sub bin is 1 s with an overlap of 50 %. In contrast to Welsh's method, we do not apply linear averaging, but average by

$$\overline{W(\omega)} = \frac{1}{N} \sum_{i=1}^{N} \log_{10} \left(W_i(\omega) \right) . \tag{2.2}$$

Here, N denotes the number of sub bins. The logarithmic averaging is done, because the fitting procedure is applied in logarithmic coordinates as well (for details see Schneider, 2015). This logarithmic averaging in Welsh's method is proposed by Attivissimo et al. (2000).

Previously, the **noise level detection algorithm** retrieved the noise level of the electronics by taking the median of the PSD in the frequency range from $f_s/3$ to $f_s/2$. This is not feasible with the revised electronics, because above $\sim f/3$ the spectrum is governed by the (lower) noise level of the ADC. Due to the rise in noise level with increasing frequency, the most effective noise level detection will use as low frequencies as possible (c.f. right panel of Figure 2.5). Therefore, we developed an adaptive method that is depicted in Figure 2.7. This method uses an input vector containing four frequency ranges f_n^R from which the noise level shall be detected. The ranges are shown by black brackets in Figure 2.6.

The general scheme of the noise level detection as depicted in Figure 2.7 is the following:

In the first place, the geometric mean of the PSD in the first frequency range (0.6 kHz to 0.8 kHz) is calculated. The *frequency of the noise level* (f_n, upper limit of fit range) is defined as the frequency where the PSD of the velocity fluctuations is smaller than the above mentioned noise mean. If the lower limit of the noise frequency range f_n^R is less than 0.25 decades larger than f_n, we expect that the respective range of f_n^R does not represent the true noise level. Instead we suppose that the frequency range of f_n^R is still in the viscous subrange. This usually happens in case of high dissipation rates ε. In this case, we change to the next frequency pair of 1.0 kHz and 1.2 kHz and so forth. If the last frequency pair at 3.0 kHz to 3.2 kHz is reached and the above described condition on the frequencies is still not met, the software reports an error. In this case, the noise level cannot be detected reliably due to the local peak in the PSD of the noise as shown by the blue curve in the right panel of Figure 2.6. We are aware that the frequency ranges 2-4 do not ideally represent the noise level of the electronics in the lower frequencies. However, as they are only used in case of high dissipation rates the addition of the noise power does not significantly deform the spectrum at these lower frequencies. This is because the PSD of the atmospheric signal is orders of magnitude larger than the PSD of the noise.

Further improvements to the retrieval scheme that have been made in the course of this thesis include a **revision of all fit quality criteria**. The result has been outlined in Section 2.3 already. We were able to reduce the number of criteria because the revised electronics and the improved calculation of the PSD shows less distortions than previous versions.

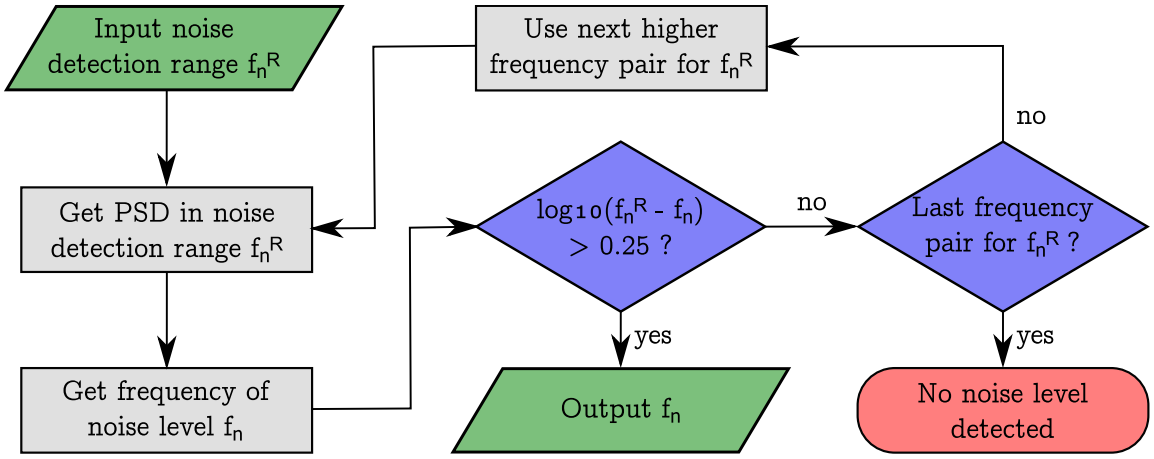

Figure 2.7: Flowchart showing the revised version of the noise level retrieval.

2.5 Limitations of atmospheric CTA measurements due to flow rarefication

Constant temperature anemometers (CTAs) have been used for many decades to record turbulent wind fluctuations in the atmospheric boundary layer (e.g. Gill, 1954). These applications demand a comparatively sophisticated calibration of the anemometer, because temperature and pressure of the examined flow change to a large extend. Such a calibration can be done, for example by mounting the apparatus on a vehicle and driving through a mountainous area in different temperatures at different speeds (Hugo et al., 1999). In order to reduce the attenuation of the CTA signal due to heat conduction from the wire to its prongs, it is commonly acknowledged that the length to diameter ratio of the wire needs to be larger than 200 (e.g. Li, 2004). Therefore, the sensor diameter is restricted to a few micrometers (5 μm in our case).

Due to these low sensor diameters in combination with ceiling altitudes of our measurements exceeding 30 km, the flow around the sensor reaches Knudsen numbers larger than one (see Figure 2.8). This means that the mean free path of the measured flow is larger than the diameter of our sensor. From these initial considerations, three questions emerge that shall be addressed in this section:

- What are the appropriate means to evaluate the influence of rarefication on CTA measurements?
- Is rarefication of the flow around the sensor a point of concern for our LITOS measurements?
- If the answer to the above question is

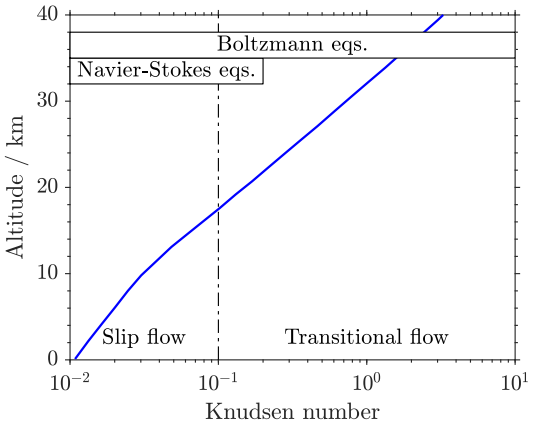

Figure 2.8: Knudsen number of the flow around the LITOS sensor. Annually averaged atmospheric background taken for 50 °N.

yes, what is the altitude limit for our turbulence evaluation?

The Knudsen numbers shown in Figure 2.8 are calculated according to Equation 1.19. Temperature and pressure data were taken for 50 °N from CIRA-86 (Fleming et al., 1990). The calculation reveals that the CTA is operated in the slip flow regime throughout the troposphere and in the lower part of the stratosphere (e.g. Colin, 2004). In the slip flow regime the Navier-Stokes equations remain valid, but a velocity and temperature jump at walls is expected and should be taken into account. Bird (2003) states that the Navier-Stokes equations show significant errors for a local Knudsen number above 0.1 and that it must be replaced by a molecular approach for $Kn \geq 0.2$. Consequently, the continuum approach of the Navier-Stokes equations is no longer valid in the transition regime, but collisions between molecules cannot be neglected. However, both ranges can be mathematically described by the Boltzmann equations (Bird, 2003).

Concerning the Knudsen number limit for the CTA, the manufacturer of the device, and the related hot-wire probes, states that the lower pressure limit for the operation of the CTA is given by the slip-flow regime (Jørgensen, 2005). This would correspond to an altitude limit of about 18 km. Previously, Theuerkauf (2012) has mentioned that there may be issues with CTA measurements at high Kn, but had no experimental means of analysing the question. Generally, we expect that the reduced sensitivity of the CTA in the transition flow regime will increase the relative influence of unwanted effects like heat conduction from the wire to the prongs. The increased heat conduction to the prongs in turn is expected to increase the attenuation at high frequencies (Li, 2004).

This calls for further investigations of the effect of flow rarefication on the LITOS measurement. However, currently we do not have access to a wind tunnel that can generate flows in the relevant pressure and temperature ranges. Therefore, we chose to study the behaviour of the LITOS sensor using the *Direct Simulation Monte Carlo* (DSMC) method as outlined in Sections 2.5.1 and 2.5.2. In Section 2.5.3, these simulations will be compared to and augmented by experimental results obtained in an open-circuit flow chamber by Xie et al. (2017).

2.5.1 DSMC method and setup

As mentioned above, we apply two dimensional DSMC to simulate the heat flux on the surface of the sensor. DSMC is used, because solving the Navier-Stokes equations does not allow one to correctly simulate transitional flows. Direct numerical calculations of the Boltzmann equations are too computationally expensive in our case. The same is true for deterministic simulations at the molecular level, like the *molecular dynamics* (MD) method. The DSMC method has been introduced by Bird (1963). Its basic principle is to uncouple the molecular motions from intermolecular collisions for a short time interval. Namely, for each time step all molecules are moved along a distance according to their thermal velocity and the length of the time step. The latter needs to be small compared to the mean collision time. In a second step, a representative amount of collisions are calculated. Each collision partner will be given a random direction of motion after the impact. Generally, the DSMC method has similar limitations as direct numerical calculations of the Boltzmann equations: they can be applied to dilute gasses only (Bird, 2003). However, the DSMC method is computationally much faster.

Currently, there are mainly two implementations of the DSMC method available: the

original code[3] described by Bird (2003) and the dsmcFoam+ solver described by White et al. (2018). The latter is more flexible,because it is based on the open source platform OpenFOAM. However, our two dimensional setup can be conveniently realised using Bird's original code. This is because our LITOS sensor can be investigated by simulating the flow around an infinitely long heated cylinder. Please note that this excludes end-conduction effects from the wire to the prongs. This simplification is necessary because including the whole dynamic behaviour of the sensor in the simulation would not be possible in the time frame of this work.

In the setup we chose a domain from $-100\,\mu\mathrm{m} < x < 200\,\mu\mathrm{m}$ and $0 < y < 100\,\mu\mathrm{m}$. The cylinder of $5\,\mu\mathrm{m}$ diameter is located at the centre of the domain with a uniform surface temperature of 553 K (280 K overtemperature). $y = 0$ is a symmetry plane while all other domain borders are interfaces with the main stream. This comparatively large domain size is used in order to minimise boundary effects on the temperature field. This simulation is set up for four different pressures: $p = [3,\ 10,\ 30,\ 100]$ hPa. Generally, it would be desirable to cover all pressure ranges that occur during a LITOS sounding by different simulations. This would enable us to use them for an error estimate as proposed in Section 2.5.4. However, simulating the flow around the wire at pressures > 100 hPa requires the use of parallelised DSMC implementations, which is beyond the scope of this work.

The gas in the simulation domain is air consisting of 80 % nitrogen and 20 % oxygen. The temperature of the main stream is taken from the annual average of CIRA-86 (Fleming et al., 1990) for 50 °N ($T = [249.6\ 230.7\ 219.6\ 218.4]$ K). Some further parameters are set according to the recommendations made by Graeme A. Bird via the programme's interface (number of collision cells, number of sampling cells, number of simulated molecules and time step). At each altitude, the flow is simulated for two different velocities: $3\,\mathrm{m\,s^{-1}}$ and $7\,\mathrm{m\,s^{-1}}$. At an average descent speed between $4.5\,\mathrm{m\,s^{-1}}$ and $5.5\,\mathrm{m\,s^{-1}}$, we expect this to be the range that will be covered by the changing background together with the turbulent fluctuations.

2.5.2 DSMC flow field and surface properties

Before describing the flow field in our DSMC simulations of the LITOS sensor, we introduce the general picture that can be expected from the flow around a heated cylinder. In all investigated altitudes the Reynolds number of the flow around the sensor is below 50, which hints that no vortex shedding takes place (e.g. Henderson, 1995). In this case, we expect an increased velocity orthogonal to the object and slightly more downstream with respect to the flow direction. Furthermore, a reduced speed in the wake behind the sensor as well as directly in front of it is expected. Gas temperatures will decrease radially from the heated sensor with the circular shape being deformed by the flow towards the downstream side of the domain (e.g. Jodlbauer, 1933). For an increasing rarefication of the flow, we furthermore expect an increasing temperature jump and velocity slip from the wall of the heated cylinder to the flow (e.g. Colin, 2004).

Figure 2.9 shows the temperature of the flow in the domain of the DSMC simulations. It is clearly visible that, for higher pressures, the temperature field is deformed with increased temperatures occurring downstream of the heated sensor. This effect diminishes for decreasing pressure until the effect is barely visible at 3 hPa. Furthermore, we note that the temperature jump from the surface of the sensor (553 K) to the boundary layer flow

[3] www.gab.com.au/downloads.html (Last accessed: 20/09/19)

increases from $-65\,\mathrm{K}$ at $Kn = 0.079$ to $-205\,\mathrm{K}$ at $Kn = 3$.

As stated by Fan and Shen (2001), DSMC velocity fields show considerable statistical scatter if the simulation is run for low speeds. We counteract this effect by spatially averaging the velocity fields. This is done by individually applying a convolution with a five-point Gaussian-shaped averaging kernel on the U, V and W fields. The smoothed fields are then used to calculate the absolute flow speed that is shown in Figure 2.10. This leads to smooth flows for 100 hPa, 30 hPa and 10 hPa. On the other hand the simulation at 3 hPa still shows some velocity scatter. This is overlaid by wave-like oscillations that could possibly influence surface heat fluxes. However, as these oscillations are not present on the surface values depicted in Figure 2.11, we still consider the 3 hPa heat fluxes usable for our analysis. For higher pressures, the flow speeds exhibit the typical pattern of a flow around a cylinder with an increased velocity orthogonal to the object and downstream of the object. However, these patterns get weaker with decreasing pressure and almost vanish for 3 hPa. Similarly, the size of the wake zone around the cylinder decreases with increasing Kn, thereby increasing the velocity slip as described above.

In order to examine the effects of density reduction and flow rarefication on the CTA signal, we investigate the mean net energy flux along the surface of the sensor. This flux is equivalent to the convective heat transfer h, which is proportional to the Nusselt number $Nu(Re, Kn) = \frac{h\,l}{k}$ (c.f. Section 1.2.2). Here, we will regard the Nusselt number of the flow around the sensor instead of looking at the heat flux directly in order to allow for a quantitative comparison with Xie et al. (2017). This is possible because the thermal conductivity k is nearly constant for all pressures and temperatures used in the simulations. More precisely, we use $k = [0.0200,\ 0.0200,\ 0.0205,\ 0.0185]$ for the pressure levels of our simulation. The values for k are taken from Lasance (2002), though further information can be obtained from Kadoya et al. (1985). The temperatures corresponding to the pressures have been acquired from CIRA-86 (Fleming et al., 1990) for 50 °N. In conclusion, the differences in k are below 10 % and the characteristic length scale l is constant, which makes Nu a good representative of h.

In the first place, we show the net heat flux across the surface of the sensor, which is a direct output of the DSMC simulations. Figure 2.11 shows the net heat flux data averaged over 100 time steps of the simulation, after the flow field has stabilised. The negative sign denotes an energy outflow from the heated wire. We note first that the heat flux significantly depends on the pressure of the flow. Additionally, we observe that for $Kn = 0.079$ (i.e. 100 hPa) the heat flux for a flow speed of $7\,\mathrm{m\,s^{-1}}$ is larger than for $3\,\mathrm{m\,s^{-1}}$ almost everywhere on the wire. This is different for $Kn = 3$ (3 hPa). Here, the heat flux at the downstream position of the sensor is larger for $3\,\mathrm{m\,s^{-1}}$ than for $7\,\mathrm{m\,s^{-1}}$. This can be understood as a consequence of flow rarefication. Since the mean free path is larger than the diameter of the sensor, the increased number of upstream surface interactions for the higher flow velocity is almost balanced by the reduced number of interactions downstream. Furthermore, we note that the relative and absolute fluctuations of the heat flux along the surface are larger for higher pressures. This is a technical effect caused by the type of simulation: due to the higher number of molecular interactions, the number of collision and sampling cells in the simulation needs to be enhanced for higher pressures. Therefore, the number of molecules per cell is lower in order to limit the computational cost. This in turn leads to higher fluctuations in the surface heat flux. However, as we are only interested in the averaged heat flux along the surface for quantitative comparisons, this does not limit our evaluation.

The dependence of the Nusselt number on the flow velocity ($\Delta Nu/\Delta U$) is shown in the

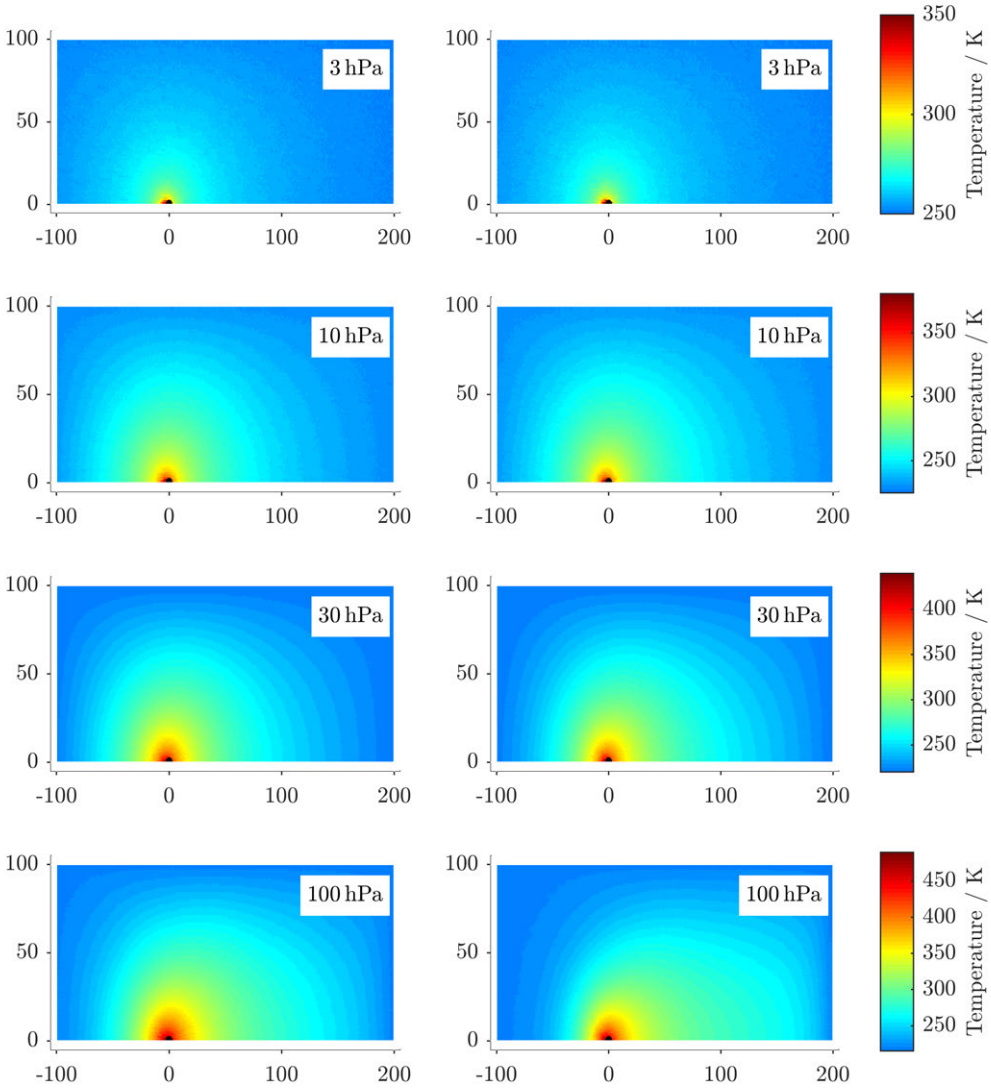

Figure 2.9: Gas temperature in the DSMC domain. The sensor is located at coordinate centre (black half circle). Left to right: Flow speed in the reference stream of $3\,\mathrm{m\,s^{-1}}$ and $7\,\mathrm{m\,s^{-1}}$, respectively. The reference pressures correspond to Knudsen numbers of 3, 1.0, 0.28 and 0.079 (top to bottom). x and y-axes show domain size in μm. The flow is in positive x-direction. Please note the different colour scales.

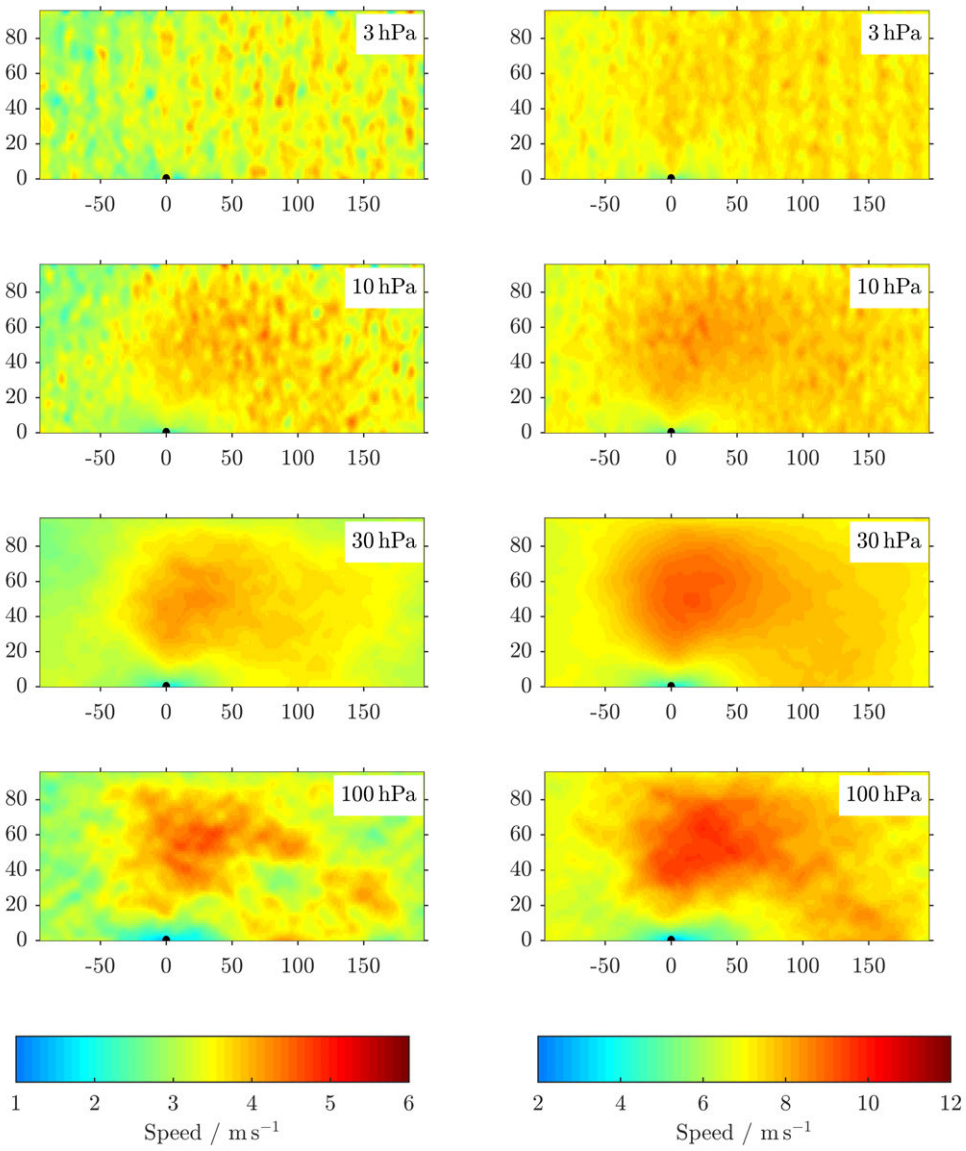

Figure 2.10: Same as Figure 2.9, but for flow velocity.

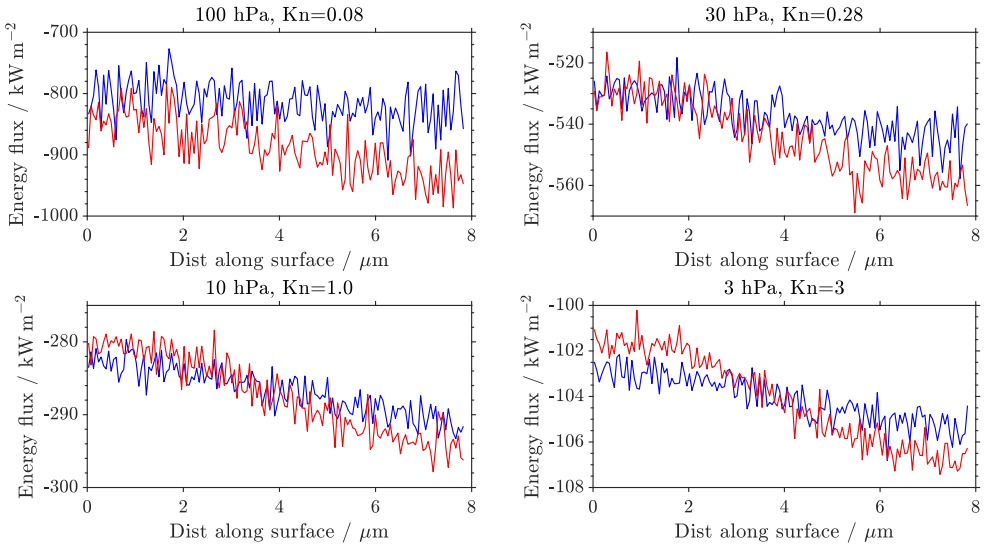

Figure 2.11: Net energy flux in DSMC simulations on sensor surface. Distance along surface given counter-clockwise from the most downstream point of the simulated sensor. Flow velocities are $3\,\mathrm{m\,s^{-1}}$ for the blue curve and $7\,\mathrm{m\,s^{-1}}$ for the red curves.

left panel of Figure 2.12. The plot is based on the heat flux from the DSMC simulations at $3\,\mathrm{m\,s^{-1}}$ and $7\,\mathrm{m\,s^{-1}}$ presented in Figure 2.11. For the absolute values of the Nusselt number, please see Figure 2.13. According to our simulations, the dependence of the Nusselt number on velocity is reduced by three orders of magnitude when the pressure changes from 100 hPa to 3 hPa. The right panel of Figure 2.12 shows the dependence of the Nusselt number on the Reynolds number for the same set of simulations ($\Delta Nu/\Delta Re$). We see a reduction of this ratio by 1.5 orders of magnitude when the Knudsen number changes from 0.079 to 3. It is insightful too look at this ratio because $Re = \frac{U\,l}{\nu}$ already includes density effects on the heat transfer from the sensor. Therefore, $\Delta Nu/\Delta Re$ mirrors the effect of the flow rarefication on the CTA signal separated from the effect of density reduction.

2.5.3 Discussion

As can be seen in the right panel of Figure 2.13, the Nussel number of the flow around our sensor is reduced by about two orders of magnitude between 100 hPa and 3 hPa (16 km and 39 km). As discussed above, the reduction in Nu corresponds to a reduction in the CTA signal level, because Nu is a good representative of the heatflow across the sensor surface h. In order to compare these results with measurements, we will consider results from Xie et al. (2017).

The left panel of Figure 2.13 shows Nusselt number against Reynolds number for the flow around a CTA sensor from Xie et al. (2017). Generally, we see that for an increased Knudsen number, the dependence of the Nusselt number on the Reynolds number decreases. In other words, the sensitivity of a CTA measurement on velocity changes is reduced by flow rarefication. The effect seen in the left panel of Figure 2.13 is not caused by density reduction as, for example, already included in less complex descriptions of the CTA response like in Eq. 1.23. In the data underlying Figure 2.13, the density dependence is already taken into account by plotting the Nusselt number as a function of Reynolds number instead of

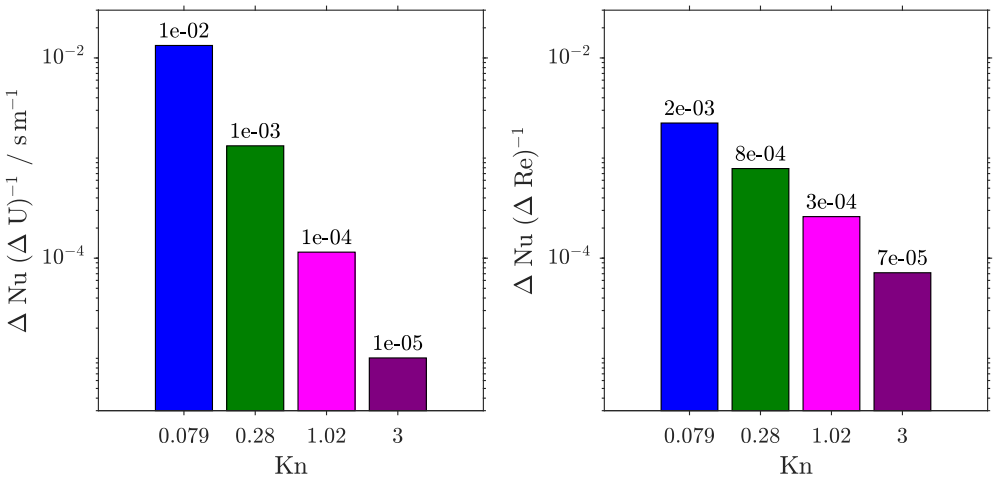

Figure 2.12: Left: dependence of Nusselt number on velocity. Right: dependence of Nusselt number on Reynolds number. For each Knudsen number, two DSMC simulations at $3\,\mathrm{m\,s^{-1}}$ and $7\,\mathrm{m\,s^{-1}}$ have been used. The Knudsen numbers correspond to pressure levels of 100 hPa, 30 hPa, 10 hPa and 3 hPa from left to right.

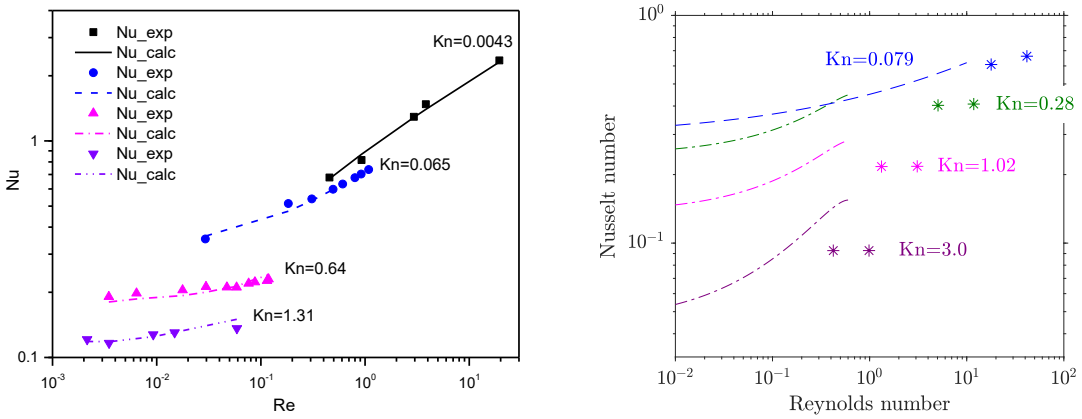

Figure 2.13: Left: Reprint of Figure 9 from Xie et al. (2017). Right: Stars denote results from DSMC simulations presented in Figure 2.11. The dashed line denotes calculations according to Xie et al. (2017, Eq. 22), dashed-dotted lines according to Xie et al. (2017, Eq. 23).

velocity. A reduction in pressure at a constant Knudsen number would lead to a reduction in Re, where the slope of the Nu vs. Re function is reduced. Similarly, the left panel of Figure 2.13 shows a reduction of the slope $\Delta Nu/\Delta Re$ with increasing Kn for Knudsen numbers larger than one. However, this does not hold for the higher Knudsen numbers they investigated (e.g. $Kn = 1.31$, Xie et al., 2017, Figure 10). Their predictions see a reduction in overall Nu, but an increase in the slope of Nu vs. Re. We do not understand this counterintuitive behaviour of their prediction for high Kn. Generally, it should be noted that Xie et al. (2017) do not attempt to model the underlying physical processes of heat transfer in their mathematical model. Instead, they simply fitted their experimental data using the Matlab function *nlinfit*. They offer three different fit functions for different Knudsen and Reynolds number ranges denoted by solid, dashed and dashed-dotted/dashed-double-dotted lines.

In the right panel of Figure 2.13 we compare our DSMC simulations to the fit functions from Xie et al. (2017). There is a good agreement between our simulation and their fit function for $Kn = 0.079$ (at 100 hPa). This is the case with respect to the absolute value of the Nusselt number as well as for the slope of the dependence. For higher Knudsen numbers, the upper limit of their fit function is reduced to $Re = 0.6$. We note that their fit function for the transitional flow regime ($0.1 < Kn < 3$, dashed-dotted lines in Figure 2.13) shows a considerably higher slope compared to the fit function in the slip flow regime ($0.01 < Kn < 0.1$, dashed lines in Figure 2.13). This seems to contradict their experimental results shown in the left panel of Figure 2.13 as well as ours obtained from DSMC. This is probably because all their experimental data from the relevant Knudsen number range that they included in Figure 2.13 do not exceed $Re = 1.5$ and because their fitting algorithm does not model the physical processes behind their experiment. Furthermore, all data shown in Xie et al. (2017, Figure 8) for $Nu < 0.1$ (high Knudsen numbers) show distinctly worse correlation between the experiment and the calculation than those for higher Nusselt numbers. This leads us to the conclusion that further experimental investigations of the CTA calibration for $Re > 10^{-1}$ and $Kn > 0.1$ might be worth the effort.

Possible reasons for errors on our side include that we assume an ideal sensor with no aerodynamic influence of the prongs and an equal surface temperature throughout the wire. For real sensors, the temperature distribution along the wire axis follows a hyperbolic cosine (catebary curve) due to heat losses to the prongs (e.g. Bailey et al., 2010). However, we assume that this effect will not be crucial because the attenuation of the wire signal due to the heat flow into the prongs mainly affects higher frequency components, which are not investigated in our DSMC simulations (Li, 2004).

Xie et al. (2017) show that a reduction in density and Knudsen number reduces the signal level (Nu) as well as the dependence of the signal on Reynolds number. This is true for all Kn except $Kn = 1.31$. Our DSMC shows that the SNR of our CTA is reduced by three orders of magnitude when the pressure is reduced from 100 hPa to 3 hPa. 1.5 orders of magnitude of this reduction are caused by flow rarefication (c.f. Figure 2.12). Even though this is a considerable reduction in SNR, it still does not give a clear answer up to which pressure level a CTA measurement can be used with our LITOS turbulence evaluation.

As our method of obtaining energy dissipation rates is based on the slope of the velocity spectrum, we crucially depend on the frequency response of the CTA. Li (2004) has studied the frequency response of a similar CTA system (5 μm platinum sensor, length to diameter ratio of 200, overheat ratio of 0.5, $Re \approx 350$). He finds a combined cut-off frequency of 13 kHz (determined from the 3 dB line in Li, 2004, Figure 9). Furthermore, he states that a decrease in Reynolds number as well as a decrease in length to diameter ratio will further

reduce this cut-off frequency. This is mainly due to attenuation by heat flow into the prongs. More specifically, reducing the Reynolds number from $Re \approx 1000$ to $Re \approx 100$ will reduce the cut-off frequency from 22 kHz to 9.2 kHz. The cut-off frequency used in our evaluation is 4 kHz. Typical frequencies where our turbulent velocity signal goes below the noise level of the instrument are a few 100 Hz. Therefore, we assume that reducing our signal by three orders of magnitude from 100 hPa to 3 hPa ($Re = 30$ to $Re = 0.7$) may alter the frequency response such that the relevant part of the measured spectrum is expected to be deformed by the attenuation of our anemometer system.

2.5.4 Conclusion

Coming back to the questions posed at the beginning of this section, we state that the rarefication of the flow around the CTA sensor reduces the Nusselt number by three orders of magnitude, according to our DSMC simulations. However, we did not find any Knudsen number where the CTA principle appeared to be unusable up to $Kn = 3$. Also, based on the experimental results from Xie et al. (2017), and especially on the considerations of the dynamic response of a CTA system in turbulence measurements by Li (2004), we take the following decision for the altitude or Knudsen number limit of our turbulence evaluations.

We will retrieve **energy dissipation rates for Knudsen numbers below** $Kn = 0.1$. This corresponds to an altitude limit of about 17.5 km. We consider this limit to be a conservative estimate, also based on guidance given by the manufacturer of the CTA system (Jørgensen, 2005) and on more general considerations by Bird (2003). This does certainly include that later evaluations of the frequency response of our CTA system may reveal that it is perfectly fine to use our data evaluation technique in higher altitudes. Other evaluation techniques like the "inertial subrange method" used on the HYFLITS instrument (c.f. Chapter 4) can be evaluated because they do not need a frequency resolution as high as LITOS.

However, we still expect that we **can distinguish between turbulent and non-turbulent altitude bins in all altitude ranges**. This is because also slightly deformed turbulent spectra are easily distinguishable from non-turbulent ones. This is used in Chapter 5 to describe a breaking mountain wave in about 30 km altitude.

Coming back to the first question on the importance of rarefication effects, we state that they should not be neglected for pressures below 100 hPa. They lead to a signal reduction of 1.5 orders of magnitude out of the total reduction of three orders of magnitude from 100 hPa to 3 hPa.

From our point of view, the best method to investigate the effect of flow rarefication is an experimental dynamic response test in a wind tunnel. Appropriate wind tunnels have been described by Wilson et al. (2008) and Xie et al. (2017). However, the experimental investigation of dynamic responses is technically challenging and can be replaced by determining the CTA signal as done by Xie et al. (2017), but for higher Reynolds numbers. The dynamic response could then be investigated by analytical methods as proposed by Li (2004).

However, such a wind tunnel is not available to us at the moment. Therefore, this study could be advanced by using the CTA signal as obtained from our DSMC simulations as a basis for the above mentioned analytical investigations in the frequency response of the CTA system. Furthermore, the uncertainty of our turbulence evaluation can be evaluated by an error propagation including all parameters of the evaluation, like the relative vertical balloon velocity w_{rel}. The influence of the decreasing SNR will than be included by a Monte-

Carlo-type simulation, where we use a theoretical spectrum with added atmospheric and instrumental noise. This artificial spectrum is evaluated by our turbulence retrieval scheme. By statistically applying this method for all altitude ranges, we will get a mean error of our spectral model due to instrumental noise and fit errors for each altitude range. Even though some work has been done along the described route, the task cannot be finished in the time limit of this work.

Such an error analysis will also allow to determine the influence of the dissipation rate (i.e. the SNR) on these flow rarefication effects. For low dissipation rates (low SNR) we expect a lower altitude limit compared to higher dissipation rates. In Chapter 4 we present a comparison of two turbulence measuring instruments, where we saw an influence of these flow rarefication effects on the LITOS instrument in case of low SNR measurements.

2.6 Sounding balloons as a platform for atmospheric turbulence measurements

Generally, sounding balloons are a well established platform for atmospheric in-situ measurements from the ground to an altitude of about 35 km. Horizontally, they roughly act as a passive tracer, i.e. they approximately follow the wind. However, as already mentioned in Section 1.2, a payload below a sounding balloon will not exactly follow the air motions but will be subject to certain eigenmotions. They can be divided in:

- Self-induced balloon motions
- Internal balloon oscillations
- Swinging of the payload below the balloon
- Rotation of the payload.

The latter two have been discussed by Schneider (2015) and Söder (2014). Their main findings were that in order to reduce the pendulum motions a high weight to drag ratio is beneficial. This can be achieved, for example, by using spherically shaped payloads. This will slightly increase the rotation of the payload. However, a spherical shape was found to be the best compromise in terms of data quality. Furthermore, a longer string increases the period of the pendulum motions, taking them further away from the relevant spectral range of the measurement. Therefore, we use a distance between the balloon and the gondola of 130 m in the current version of the payload.

Self-induced balloon motions were studied extensively during the 1960s in the United States. The interest was triggered by the need for reliable stratospheric wind measurements within the Apollo programme. However, the attention of the scientific community to the subject has reduced in the past decades. It is nevertheless discussed in the Section 2.6.1, because for high resolution turbulence measurements, these effects should not be neglected.
On the other hand, the occurrence of internal balloon motions has not been extensively discussed in the literature. Their influence on balloon measurements is discussed in Section 2.6.2.

2.6.1 Self-induced balloon motions

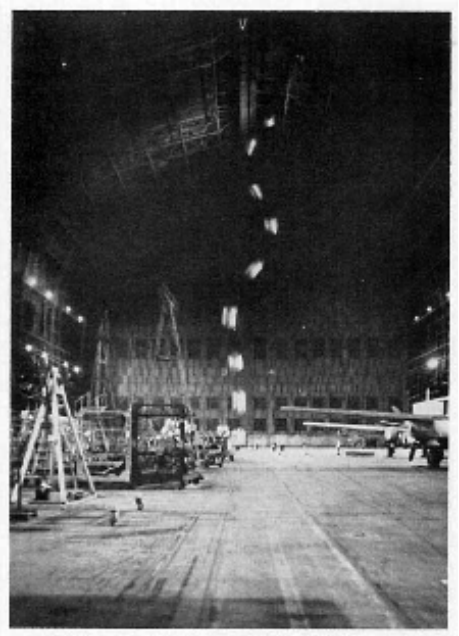

Figure 2.14: Self-induced motions of a spherical balloon captured by multiple exposure every 1/4 second. Image taken from Murrow and Henry (1965).

During ascent, the shape of a sounding balloon is approximately spherical. Some wobbling motions of the balloon's skin lead to deviations from this shape, as discussed in Section 2.6.2. Even a spherical balloon, however, will not ascent straight, but shows erratic motions in the horizontal plane as well as erratic variations in ascent rate (c.f. Figure 2.17). They are called *Self-induced motions* in this study. A comprehensive summary of the phenomenon is given by Scoggins (1967). These motions appear in the supercritical ($Re > 4 \cdot 10^5$) Reynolds number range. The critical Reynolds number range is characterised by a sharply decreasing drag coefficient c_d with increasing Re as shown in Figure 2.15 from Achenbach (1972).

The Reynolds number of the flow around the LITOS-balloon is shown in the left panel of Figure 2.16. In the critical Reynolds number regime ($Re \approx 3000 \ldots 4000$ for a smooth sphere), the flow separation moves further downstream on the surface of the sphere with increasing Re (a good visualisation is given by Taneda, 1978). In the supercritical regime, however, an increase in ascent rate leads to higher Re and lower c_d (c.f. Figure 2.15). This in turn decelerates the balloon, reducing Re, decreasing c_d and so forth. Accordingly, the ascent rate of a rising balloon in the supercritical Reynoldsnumber regime is unstable. The wavelet analysis in the right panel of Figure 2.16 shows oscillation periods between 10 s and 50 s (wavelengths between 50 m and 250 m). Scoggins (1965) obtained similar oscillation periods with the peak in power spectral density at 40 s. The wavelet analysis from Figure 2.16 shows another peak at periods of roughly 400 s in a altitude above 15 km. This signal is related to mountain waves and not caused by the balloon (model data and analysis not shown).

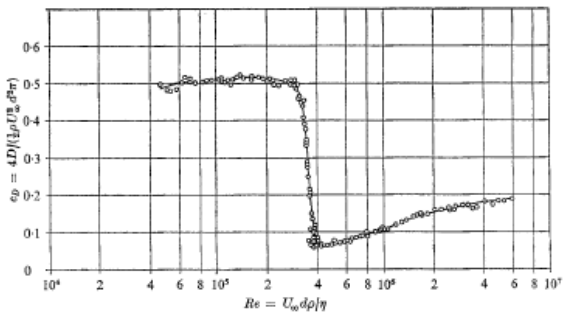

Figure 2.15: Drag coefficient of a smooth sphere vs. Reynolds number. From Achenbach (1972)

The self-induced balloon motions do not only occur on the ascent rate, but they lead to horizontal oscillations of the balloon as well. A multiply exposed picture of a balloon ascent in still air showing these oscillations is given in Figure 2.14. These horizontal oscillations occur because small imperfections of the sphere (caused, for example, by internal balloon motions as described in Section 2.6.2) lead to an asymetric boundary layer detachment that results in a lateral drag force. For a quantitative analysis using spheres in a wind tunnel, please see Norman and McKeon (2011). MacCready (1965) gives the following empirical estimate for the maximum amplitude of

these horizontal oscillations:

$$\Delta_{X_{\mathrm{SI-h}}} = \frac{2.8\,D}{1+2\,m_r}, \tag{2.3}$$

where D is the diameter of the balloon and $m_r = \frac{m_b+m_{\mathrm{He}}}{m_{\mathrm{air}}}$ the relative mass of the balloon compared to the mass of the displaced air.

These oscillations can be avoided by using a balloon-type called *Jimsphere*. It is a spherical superpressure balloon with numerous conical hubs of about 10 cm in height. As shown by Achenbach (1974), the drop in c_{d} at the critical Reynolds number range becomes smaller with increasing surface roughness. Scoggins (1965) shows that this effect makes the drag coefficient of a Jimsphere almost independent of the Reynolds number, making it unaffected by self-induced motions. Currently, Jimspheres can be obtained from Meteorological Product Inc. However, they are only available in a 2 m diameter version. Unfortunately, this is too small for our LITOS instrument.

From our own results combined with those from Scoggins (1965) and MacCready (1965), we conclude that horizontal and vertical wind measurements in the supercritical Reynolds number range on vertical scales below 500 m are presumably influenced by self-induced balloon-motions. Scales below 250 m are likely to show strong influences that make geophysical evaluations questionable. From Figure 2.16 we find that the smallest vertical scales influenced by self-induced motions are 50 m (10 s). This corresponds well to MacCready (1965), who finds the same lower wavelength limit. This is just at the outer scale L_0 limit of the inertial subrange in 15 km altitude (c.f. Figure 1.3). Accordingly, there is no influence expected on any of the retrieval schemes presented in Section 1.2. However, these effects will become important in the context of wake influences (Chapter 3).

2.6.2 Internal balloon oscillations

A phenomenon known to many balloon researchers is the oscillation of the balloon's shape from a droplet-like silhouette to a doughnut type outline. They are particularly visible directly after launch, as shown in Figure 2.17. In this study we will call them *internal balloon oscillations*. When comparing this first cycle of the oscillation, one should keep in mind that the amplitude is most likely stronger than in the measurement phase of the flight. This is expected because the payload is still on the ground and aerodynamic forces on the balloons shape are therefore stronger due to the enhanced ascent rate of the balloon.

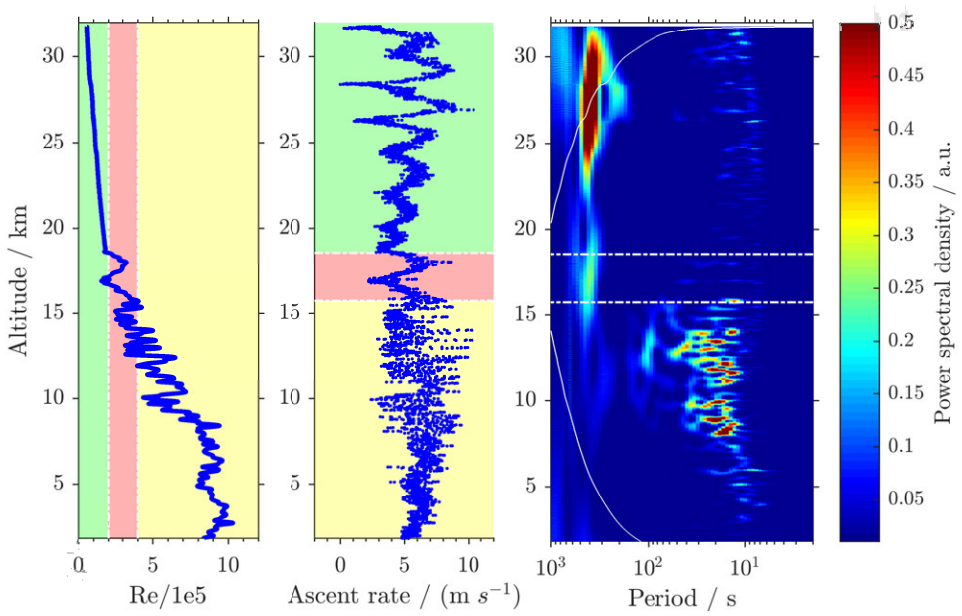

Figure 2.16: Self-induced balloon motions on 29 Jan 2016 i (Balloon: TX 3000). Left: Reynolds number of the flow around the balloon. The sub-critical, critical and super-critical ranges are marked by green, yellow and red colour-shading, respectively. Middle: Ascent rate of the balloon according to the GPS based radiosonde (Väisälä RS-41). Right: Power spectral densities of the ascent rate, using a complex Morlet wavelet. The cone of influence (solid white line) is calculated according to Torrence and Compo (1998)

.

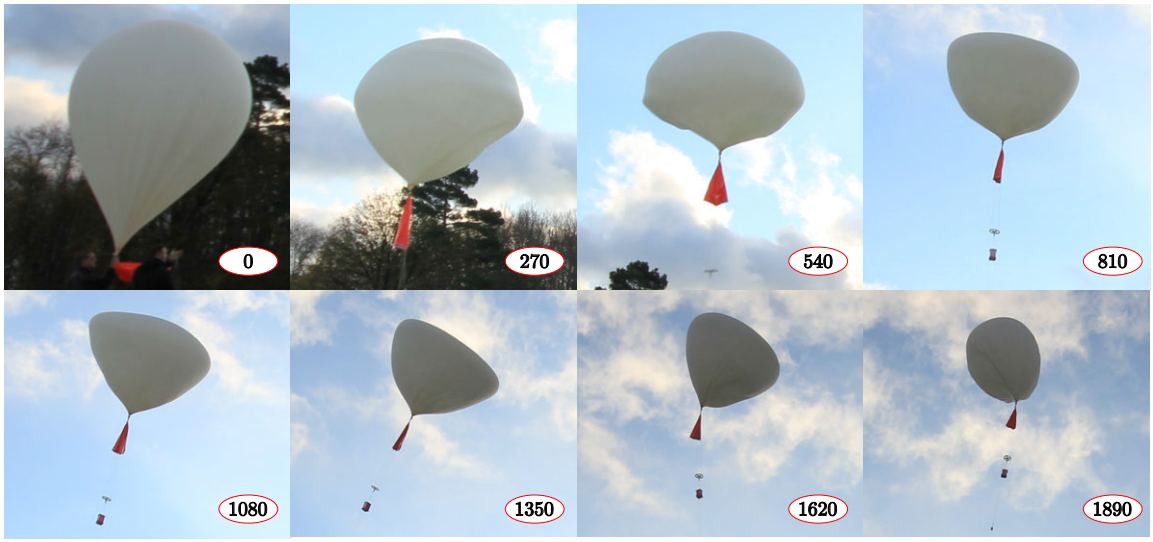

Figure 2.17: Full cycle of an internal motion of a Totex TX 3000 rubber balloon. The number indicates time in milliseconds.

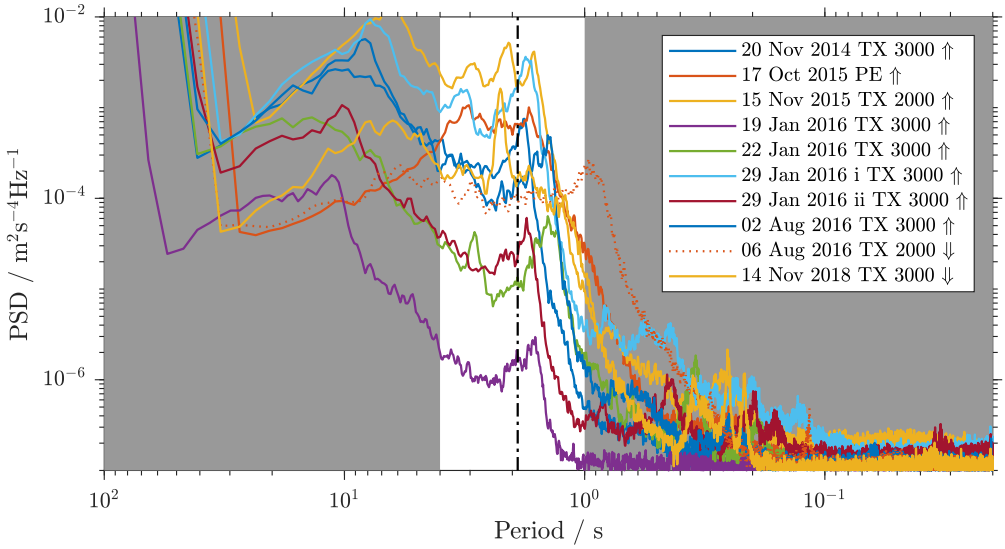

Figure 2.18: Power spectral densities of z-accelerations measured during different LITOS soundings. Periods where internal motions of the balloon occur are highlighted by a white background, the oscillation period found from Figure 2.17 is denoted by a dashed-dotted line. The legend indicates the date, followed by the balloon type. *TX* denotes a rubber balloon produced by Totex, *PE* a polyethylene balloon made by Raven Aerostar. The arrow in the end indicates ascent or descent phase measurement.

For a standard ascent rate of $5\,\mathrm{m\,s^{-1}}$ these internal balloon oscillations occur on spatial scales between 5 m and 20 m. This means that they are highly relevant for turbulence evaluations in the inertial subrange of the spectrum using Equation 1.10 (c.f. Figure 1.3).

At a first glance, they seem to be caused by the stretching of the balloon's rubber skin. In order to investigate this, we examined all LITOS flights that reached an altitude of at least 20 km. Figure 2.18 shows the PSD of the acceleration along the z-axis. Data have been acquired using the accelerometer aboard the LITOS gondola. It is noted that all flights show a local maximum in the oscillation power for periods between 1 s and 3 s. This corresponds very well to the period of 1.89 s, measured from the picture series shown in Figure 2.17. There is a second local maximum for periods around 10 s. This is most likely a mode of the self-induced balloon motions (Section 2.6.1) and shall not be discussed here. The

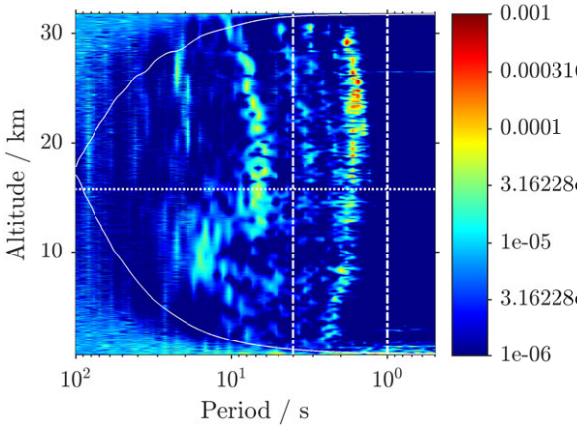

Figure 2.19: PSD of the acceleration along the z-axis using a complex Morlet wavelet. Data taken from the 29 Jan 2016 i ascent measurement. Cone of influence as in Figure 2.16. Dashed-dotted lines: lower and upper limit for internal balloon oscillations. Dotted line: upper limit of supercritical *Re*.

range of periods for the internal motions is between 1 s and 4 s (apart from one descent measurement using a TX 2000 balloon; dotted line). Both elastic TX 2000 and TX 3000 rubber balloons as well as an inextensible polyethylene (*PE*) balloon were used in this study. The PE balloon shows the same oscillating behaviour as the rubber balloons at a similar frequency. This clearly shows that the internal oscillations are *not* caused by a stretching of the balloon's skin.

Instead we propose the following mechanism: Due to aerodynamic forces, the top of the balloon is flattened, slowing down the balloon. This deceleration leads to a dynamic reduction of the weight force from the payload, flattening the bottom and giving the whole balloon a doughnut like shape. After the balloon is sufficiently slowed down the top expands again and the reduced drag leads to an acceleration of the balloon, which in turn increases the weight force from the payload. This turns the balloon back into a droplet like shape. The whole cycle can be seen in the picture series of Figure 2.17. Please note however that the sequence of the effects described above is slightly altered in the picture series, because the launch of different payload boxes modifies the weight force on the balloon.

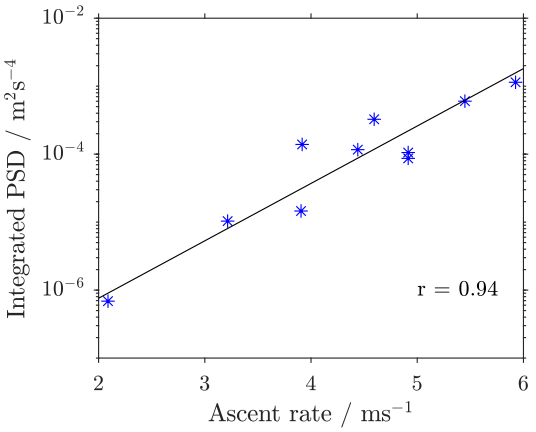

Figure 2.20: Averaged power of internal balloon oscillations. Each flight presented in Figure 2.18 is represented by a blue star, the black line shows a logarithmic regression. r denotes the correlation coefficient between the data and the regression.

In the literature there are only a few accounts of internal balloon oscillations available. Barat et al. (1984) briefly discussed the effect of self-induced balloon oscillations. However, they solely assign these effects to the supercritical Reynolds number range. From our data we cannot confirm this hypothesis. Figure 2.19 shows a wavelet analysis of the accelerations along the z-axis during the flight 29 Jan 2016 i. It is visible that internal balloon oscillations occur throughout the whole flight (i.e. in all Reynolds number regimes). In contrast to Barat et al. (1984), we find an increased amplitude at higher altitude (lower *Re*). Furthermore, the period of theses oscillations slightly decreases from 2.5 s to just below 1 s. As there is no sharp change in the critical Reynolds number regime, we assume that the slight frequency and amplitude changes are due to the enhance slight overpressure of the balloon in higher altitudes. According to our knowledge, the only invention that would avoid these oscillations on sounding balloons was made by Isom (1949). It features a flexible sounding balloon surrounded by a non elastic envelope. Slight overpressure inside the outer envelope will keep the shape of the balloon and therefore prevent internal balloon oscillations. Unfortunately, this device is not commercially available at this time, as far as we know.

Concerning the amplitude of the z-acceleration shown in Figure 2.18, huge differences in PSD between different flights can be seen. For a quantitative evaluation, the PSD has been integrated for all 10 launches over periods from 1 s to 4 s. We find that the logarithm of the integrated PSD is linearly correlated with the mean ascent rate of the balloon (Figure 2.20). The correlation coefficient is 0.94. Evaluation of the individual physical processes behind this logarithmic relationship is beyond the scope of this study.

In conclusion, internal balloon oscillations are likely to disturb turbulence measurements in the large scale part of the inertial subrange. These oscillations occur at all altitudes and currently, there is no ballooning technology available to avoid them. Therefore, any turbulence measurement should refrain from using spatial scales larger than 5 m, as we do in our method by resolving the transition from the inertial to the viscous subrange. If spatial scales between 5 m and 20 m need to be used in the analysis, it is useful to reduce the ascent rate. A reduction from $5\,\mathrm{m\,s^{-1}}$ to $2\,\mathrm{m\,s^{-1}}$ will reduce the PSD of these oscillations by about two orders of magnitude. Furthermore, it seems possible to dampen the effect of these oscillations on the payload by adding a suitable spring/dampener combination.

However, these efforts do not need to be undertaken on the LITOS system, because we do not evaluate spatial scales larger than ~ 1 m in our turbulence retrieval (c.f. Figure 2.3).

3 Wake influences on rising balloons

On ascending balloons there is a potential for the sensors on the payload to be in the turbulent wake of the balloon (e.g. Barat et al., 1984; Tiefenau and Gebbeken, 1989; Gaffen, 1994; Kräuchi et al., 2016). We will first discuss whether wake effects need to be considered at all on the basis of the data from our LITOS instrument.

This chapter will largely follow, augment and summarise Söder et al. (2019). In order to be consistent with the publication, all data shown here are acquired with the old electronics and processed with the old retrieval scheme as described in Sections 2.4.1 and 2.4, respectively.

In order to demonstrate wake influences on turbulence measurements, the left panel of Figure 3.1 shows a typical measurement from an ascending balloon, including atmospheric and wake-related turbulence. It was taken on 29 January 2016 during the GW-LCYCLE II campaign in Kiruna, Sweden. As hinted by different colour shading in the left panel of Figure 3.1, there are two causes for wake influences on the LITOS instrument: wake created by the ropes holding the gondola and wake caused by the balloon. The first creates much stronger turbulence and therefore has the strongest potential influence on LITOS soundings, showing dissipation rates between $100\,\mathrm{mW\,kg^{-1}}$ and $1000\,\mathrm{mW\,kg^{-1}}$.

In the right panel, all potentially wake affected turbulence measurements have been removed. The procedures for removing wake-influenced data are explained further below. In the course of this study, we found that 83 % of all turbulence detections shown in the left panel are potentially wake-affected. 37 % of all wake occurrences are caused by the balloon's wake. The mean dissipation rate of all measurements, including the wake, is almost one order of magnitude higher than the mean dissipation rate of wake free turbulence detections ($\varepsilon_{\mathrm{wakefree}} = 4.2 \cdot 10^{-3}\,\mathrm{W\,kg^{-1}}$, $\varepsilon_{\mathrm{all}} = 3.9 \cdot 10^{-1}\,\mathrm{W\,kg^{-1}}$). These numbers show that a typical turbulence measurement with LITOS on an ascending balloon is seriously flawed if wake effects are neglected.

Due to their higher dissipation rates on average, wake from smaller objects in the payload chain, like the ropes holding the gondola, shall be discussed in the first place. Wake from the balloon occurs on any rising balloon measurement and may not only affect turbulence soundings but temperature and humidity measurements as well (e.g. Kräuchi et al., 2016). Its strength depends on the distance between the balloon and the gondola. For a distance of 180 m, as used on the latest ascending version of the LITOS system, typical balloon-wake related dissipation rates are between 0.01 and $1\,\mathrm{mW\,kg^{-1}}$. On previous payload versions with payload-balloon distances of only 50 m, wake-induced dissipation rates higher than $10\,\mathrm{mW\,kg^{-1}}$ have been detected.

3.1 Wake from smaller objects in the payload chain

Most object in the payload chain of a rising balloon are in a Reynolds number range that fosters the formation of a turbulent wake behind them, namely $Re \gtrsim 50$. With objects located upstream of the sensors, there is a risk that their wake may hit one of the probes,

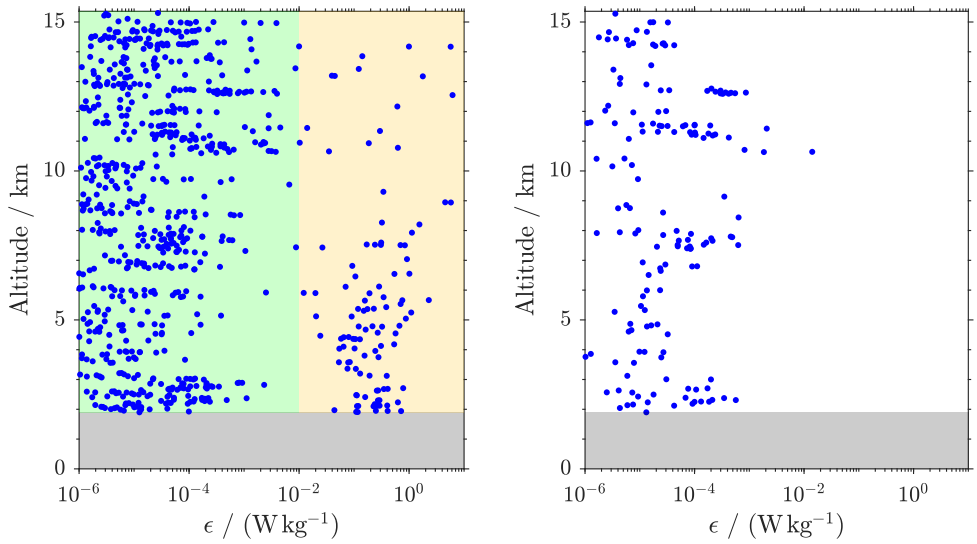

Figure 3.1: Turbulence profile from 29 January 2016. Every blue dot denotes a turbulent bin of 2 s length. In grey shaded areas the instrument cannot measure due to influences from unwinding dereelers. Left: original turbulence retrieval. Green shading denotes dissipation rates typical for balloon related wake, yellow shading highlights common dissipation rates for wake from objects close to the sensors. Right: all potentially wake affected measurements have been removed.

as visualised in Figure 3.2. Of course, this depends on the direction of the flow around the gondola. The effect of the turbulent wake on the LITOS measurement can be seen, for example, in Figure 3.3. The raw data show strong fluctuations and a reduction of the overall flow speed (left panel: instrument output voltage). The length of the turbulent section is only 6 m ($\sim$ 1.5 s) and there is a sudden transition from turbulent to non-turbulent regions.

On our payload, the most significant small objects in terms of wake production are the ropes holding the gondola. They have a length of 70 cm and a diameter of approximately 1 mm. Therefore, we can refer to basic research on the flow around cylinders in order to characterise the properties of the wake downstream of them (e.g. Williamson, 1996). The Reynolds number of the flow around the ropes is between $Re = 400$ on ground level and $Re = 5$ at 30 km altitude. For $Re > 50$ (in altitudes below $\sim$ 20 km) a Kármán vortex street forms in the flow downstream of the rope. This change of the flow properties also sharply increases the drag on the cylinder (Henderson, 1995). For $50 < Re < 10^{-5}$ such a vortex street is expected to show a distinct vortex shedding frequency. This however does not appear in the power spectrum of the rope-wake affected LITOS data shown in the right panel of Figure 3.3. This is because the sensor is located approximately 150 diameters downstream of the rope. Roshko (1954) found from CTA measurements in a wind tunnel that the energy density at the shedding frequency is reduced with increasing

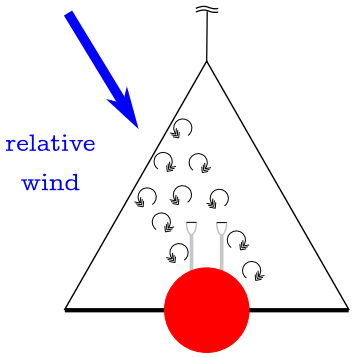

Figure 3.2: Schematic visualisation of the turbulent trail from a rope holding the payload.

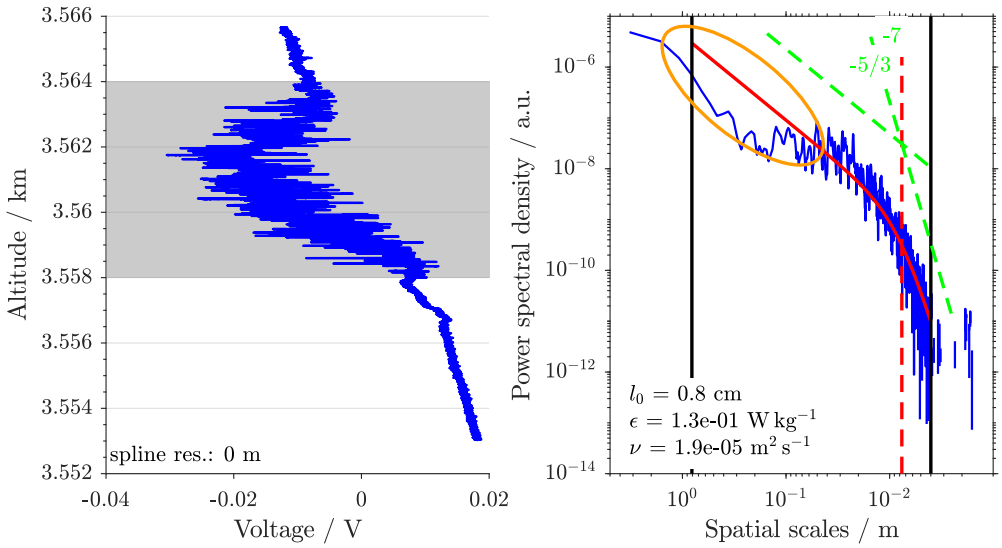

Figure 3.3: Wake of a rope holding the gondola. Left: Raw data from the CTA. Right: Turbulence retrieval fit as in Figure 2.3 from the data shown in the shaded area on the left. The orange ellipse denotes a region of reduced power spectral densities compared to the Heisenberg model (Eq. 1.14). This points to turbulence in the wake of a small object upstream of the sensor. Adapted from Söder et al. (2019).

distance to the source and cannot be recognised for more than 50 diameters. This effect can also be seen in the analogous flow around Jan-Mayen Island in Figure 3.4. The Kármán vortices are clearly visible up to 30 diameters downstream but dissolve into random turbulence for longer distances. Another informative visualisation of the breakdown of a Kármán vortex street is given in Taneda (1959).

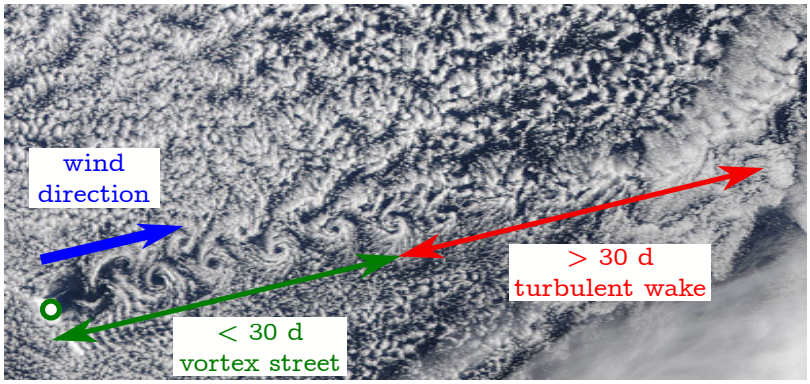

Figure 3.4: Cloud image of flow around Jan Mayen Island on 5 May 2012 with similar aerodynamic properties. Picture source: Schmaltz (2012).

Looking at the measured spectrum of such a cylinder-wake measured by the LITOS instrument, we note a drop in PSD on scales between 10 cm and 100 cm compared to the Heisenberg model (right panel of Figure 3.3). This is typical for the wake from the ropes in altitudes below 20 km ($Re > 50$). It is explained by the measurement geometry: assuming isotropy of the turbulent flow the largest eddies cannot be larger than the distance from the wake source to the sensor (15 cm here), because otherwise the growth speed of the eddies would be larger than the speed of the flow around the object. This drop in PSD allows us to sort

out those spectra from the dataset by visual inspection. An automated detection of those wake influences is not possible because the drop in PSD can be very subtle, which would dramatically increase the risk of false turbulence detections.

As we use two velocity sensors, in many cases we can circumvent an influence on our measurement by this manual inspection. If neither sensor is affected, there is obviously no action required. If only one of the sensors is influenced, we evaluate the spectrum from the other sensor. If both sensor are affected, no energy dissipation rates can be retrieved. During the LITOS measurement from 29 January 2016 this was the case for 5.8 % of all altitude bins, which equals 16 % of all altitude bins where turbulence was detected by the routine presented in Section 2.3.

This may be taken as a reminder that even small objects may create strong artificial turbulence detections on high resolution measurements ($130\,\mathrm{mW\,kg^{-1}}$ in the case shown in Figure 3.3). The turbulent motions can extend to scales orders of magnitude larger than the relevant length scale of the object, which is only 1 mm in our case. Therefore, it seems highly advisable not to place any object of the payload upstream of the sensors, even if it is of millimetre size only.

3.2 Wake from the balloon

As mentioned in the introduction to this chapter, sounding balloons create a turbulent wake showing dissipation rates usually between $0.01\,\mathrm{mW\,kg^{-1}}$ and $10\,\mathrm{mW\,kg^{-1}}$, depending on the distance to the balloon. Such a balloon has an approximately spherical shape. Therefore we can refer to fundamental laboratory studies in wind tunnels (e.g. Riddhagni et al., 1971; Taneda, 1978) and large eddy simulations (LESs, e.g. Dommermuth et al., 2002; Constantinescu and Squires, 2004). For sounding balloons as used with the LITOS payload, the Reynolds number of the flow around the balloon is between $Re = 3 \cdot 10^4$ and $Re = 1 \cdot 10^6$. A visualisation of the wake behind a sphere for slightly lower Reynolds numbers is given in Figure 3.5. It shows a plane section of the flow during a particle image velocimetry (PIV). After a short recirculation zone about 1.5 sphere diameters long, chaotic eddy formation on multiple length scales is visible. Furthermore, one can see that the diameter of the wake is not constant for different downstream distances. Instead, the core of the wake is surrounded by fringed edges.

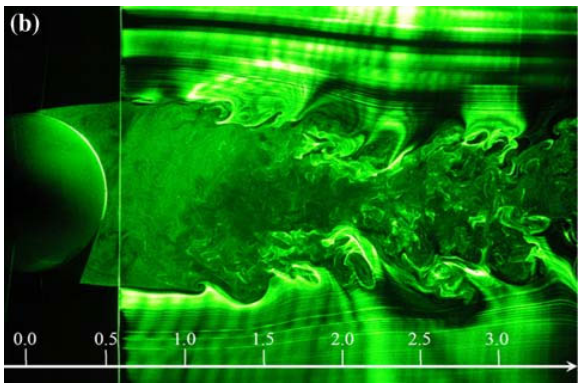

Figure 3.5: Visualisation of a turbulent wake behind a sphere at $Re = 11\,000$ from Jang and Lee (2008).

As shown in the above mentioned fundamental fluid dynamic studies, a turbulent wake will form downstream (below) the balloon for all Reynolds numbers that occur in the flow around a typical sounding balloon ($10^4 < Re < 10^6$, depending on balloon type and altitude). For a turbulence measuring instrument like LITOS, it is crucial to know whether the instrument is located within the balloon's wake or not for any moment of the measurement. There are two aspects of this question that need to be considered:

- Is there enough downstream distance between the balloon and payload in order to

completely dissolve the wake?

- Is there enough wind shear between the balloon and the gondola so that the wake passes the gondola (c.f. Figure 3.6)?

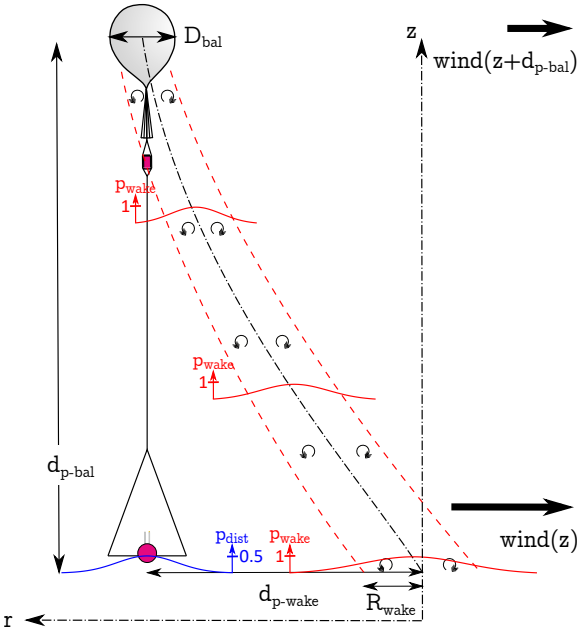

Figure 3.6: Flow within the LITOS payload chain. $d_{\text{p-bal}}$: distance between the payload and the centre of the balloon. $d_{\text{p-wake}}$: distance between the payload and the centre of the balloon's wake. Red lines show the distribution of the probability of being in the wake (dashed red line showing the full width at half maximum). The blue line shows the probability distribution for the payload-wake distance $d_{\text{p-wake}}$. Sketch is not to scale; the radiosonde below the LITOS gondola is omitted for clarity. Adapted from Söder et al. (2019).

Considering the life time of the balloon's wake, Azouit and Vernin (2005) report from laboratory experiments that the wake of a sphere persist for more than 1 000 diameters downstream. Gibson and Lin (1968) measured the turbulence intensity of a sphere wake up to 60 diameters downstream. They find a logarithmic decay of turbulence intensity with downstream distance to the sphere. At a distance of 60 sphere diameters, they measure that the turbulent dissipation rate is reduced by three orders of magnitude compared to the area just behind the sphere (from $10\,\mathrm{W\,kg^{-1}}$ to $10^{-3}\,\mathrm{W\,kg^{-1}}$). This corresponds to balloon-gondola distances between between 120 m and 800 m, depending on the respective balloon diameter. However, balloon-payload distances of more than 200 m cannot be safely handled during launch phase. Therefore, the results from Gibson and Lin (1968) suggest that the balloon's wake will not have sufficiently dissolved at the position of the gondola. Similar results are found by Dommermuth et al. (2002) in a review of laboratory experiments and direct numerical simulations (DNSs). They find a decay of kinetic energy dissipation rate with time as $t^{-2/3}$. Using the ascent rate of the balloon, the dissipation rate at the gondola position is expected to be two orders of magnitude lower than in the near field of the balloon ($t = 0.1\,\mathrm{s}$). In conclusion, we find that the dissipation rate of the balloon's wake will decrease as the balloon-payload distance increases. However, using an instrument like LITOS that resolves six orders of magnitude in dissipation rate, the wake will not sufficiently dissolve for any manageable balloon-payload distance.

Therefore, we focus on the question whether there is enough wind shear between the balloon and the payload so that the wake passes the gondola. The flow around the payload chain for this situation is depicted in Figure 3.6. Within the course of this study, we developed a tool to assess the likelihood for the balloon's wake to hit the payload. As described by Söder et al. (2019), we calculate the advection of the balloon's wake using the radiosonde wind measurement on the same balloon as the LITOS instrument. For each time step of the radiosonde, the minimal distance between the wake's centre and the turbulence

sensor is calculated. In contrast to previous approaches by Barat et al. (1984), we take into account the uncertainty in that calculation as well as self-induced motions of the balloon, pendulum motions of the gondola and vertical winds (see Section 2.6.1 and Söder et al., 2019, respectively). Therefore, we use a probabilistic approach that is briefly described in the next section. This is followed by a statistical evaluation of a radiosonde dataset and by an assessment of different parameters influencing the payload-wake distance.

Due to restrictions in the PhD examination procedure of Rostock University the content of the following three section cannot be directly quoted from Söder et al. (2019). Therefore, only a summary is given here. The MATLAB® source code for the calculations can be found at `ftp://ftp.iap-kborn.de/data-in-publications/SoederAMT2019/` (last access: 29 July 2019). The discussion of the results in Section 3.2.4 contains some information from Söder et al. (2019), but is significantly amended and augmented.

3.2.1 Method

The overall aim of our wake evaluation tool is to calculate the probability for encountering the balloon's wake at the position of the payload. This is done on the basis of radiosonde data. In order to reach a 95 % confidence level, we discard all data with wake probabilities higher than 5 % from our turbulence evaluation.

In the procedure, we assume that for every time step of the radiosonde, a wake is created at the position of the balloon. During every consecutive time step, this wake will be advected with the horizontal and vertical background wind, while the payload ascends because of the lifting balloon. Subsequently, for each time step we select all wakes that have the same time stamp. They will form a widening hose, as shown in Figure 3.6. Next, we calculate the minimal distance between the wake-hose and the payload. The mathematical expressions and further explications are given in Söder et al. (2019).

If there is no wind shear, the wake will always hit the sensors on the payload. If there is sufficient wind shear, however, the wake will pass the gondola as sketched in Figure 3.6. Nevertheless, this is a simplification of the real picture. There are considerable uncertainties in the radiosonde measurement that is used to calculate the advection of the wind and the payload. Furthermore, the diameter of the wake is not constant but changes with time due to the chaotic nature of turbulence.

The uncertainties on the radiosonde measurement that have an effect on the payload-wake distance can be divided into three categories. First, there are uncertainties in the wind measurement $\Delta\vec{U}$. They consist of errors in the horizontal wind acquired from the radiosonde and errors in the vertical wind retrieval ($0.15\,\mathrm{m\,s^{-1}}$ and $1\,\mathrm{m\,s^{-1}}$, respectively). Second, there is an error on the payload position $\Delta\vec{X}_\mathrm{p}$. The horizontal position error is given by the pendulum motions of the payload below the balloon. Their amplitude is measured by the motion sensor on board of the LITOS payload. The vertical component is given the ascent rate of the balloon and the time step of the calculation τ. This time step is decreased by linear interpolation of the radiosonde data in order to diminish that error. Third, there exist uncertainties on the position of the balloon $\Delta\vec{X}_\mathrm{bal}$. Horizontally, it is given by the self-induced motions of the balloon (c.f. Section 2.6.1). Vertically, it is governed by the vertical grid step of the calculation. Assuming these errors to be statistically independent, we find for the uncertainties of the payload-wake distance:

$$\Delta_{d_\mathrm{p\text{-}wake}} = \sqrt{\left(m\tau\vec{\Delta_U}\right)^2 + \vec{\Delta^2_{X_\mathrm{p}}} + \vec{\Delta^2_{X_\mathrm{bal}}}}, \tag{3.1}$$

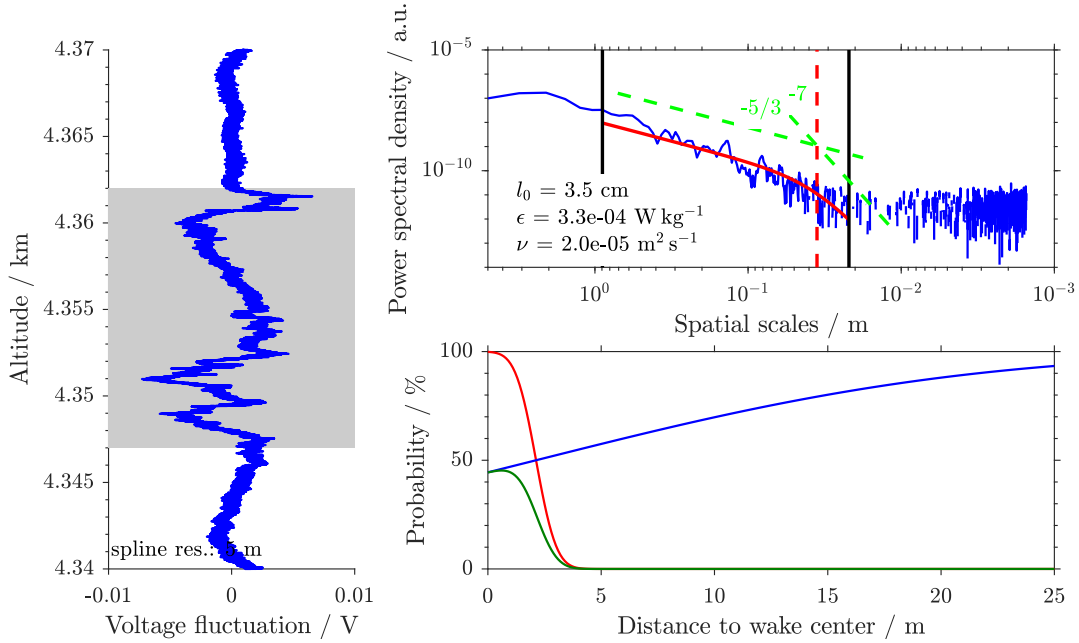

Figure 3.7: Example for turbulence caused by the balloon's wake from a LITOS launch on 29 Jan 2016. Left: Raw data from the CTA, grey shaded area influenced by wake. Top right: Turbulence retrieval fit as in Figure 2.3 from the data shown in the shaded area. Bottom right: Result from the wake prediction algorithm for the same altitude. Blue: Probability distribution of the payload-wake distance $d_{\text{p-wake}}$ to be in the range of $[0, d]$ after Equation 3.2. Red: Radial probability distribution of the wake after Equation 3.3. Green: Combined probability for wake encounter P_{wake} according to Equation 3.5. Adapted from Söder et al. (2019).

where m marks the above mentioned number of time steps between the creation of the wake and its closest encounter with the payload.

For the purpose of estimating the probability of wake encounter, the important question is: How likely is it for the true distance between the payload and the centre of the wake to be smaller than $d_{\text{p-wake}}$ as retrieved by the algorithm? This likelihood is given by a cumulative Gaussian distribution with a mean of $d_{\text{p-wake}}$ and a standard deviation of $\Delta_{d_{\text{p-wake}}} = d_{\text{p-wake}}/2$:

$$\Phi(x \mid d_{\text{p-wake}}, \Delta_{d_{\text{p-wake}}}) = \frac{\sqrt{2}}{\Delta_{d_{\text{p-wake}}}\sqrt{\pi}} \int_{-\infty}^{x} e^{-\frac{2(y-d_{\text{p-wake}})^2}{d^2_{\text{p-wake}}}} dy. \tag{3.2}$$

It is shown by the blue curve in the lower right panel of Figure 3.7.

As mentioned above, the second probabilistic process is the question whether at a certain distance to the wake centre, we are still inside or already outside of the wake. Riddhagni et al. (1971), Dommermuth et al. (2002) and Constantinescu and Squires (2004) show that the outer edge of the wake does not have a constant diameter but that its diameter varies with downstream distance to the balloon (c.f. Figure 3.5). Furthermore, the mean radius of the wake R_{wake} increases with downstream distance. Therefore, the probability for being

in the wake at a certain radial distance r is given by a cumulative Gaussian distribution:

$$\Psi(x \,|\, R_{\text{wake}}) = 1 - \frac{3}{R_{\text{wake}}\sqrt{2\pi}} \int_{-\infty}^{x} e^{-\frac{9(y-R_{\text{wake}})^2}{2\,R_{\text{wake}}^2}}\, dy. \tag{3.3}$$

It is shown by the red line in the lower right panel of Figure 3.7. The mean radius of the wake is given by the full width at half maximum (FWHM) of that distribution. Riddhagni et al. (1971) find for the mean radius:

$$R_{\text{wake}} = 0.7 \cdot \begin{cases} \left(\frac{d_{\text{p-bal}}}{D_{\text{bal}}}\right)^{\frac{1}{3}} & \text{if } d_{\text{p-bal}} \geq 6\, D_{\text{bal}} \\ 1 & \text{if } d_{\text{p-bal}} < 6\, D_{\text{bal}}, \end{cases} \tag{3.4}$$

where D_{bal} denotes the balloon diameter.

Because the uncertainties in the measurement and the width of the wake are statistically independent processes, we consider both probability distributions as statistically independent. Accordingly, the probability for wake encounter at a certain distance d to the wake centre is given by the product of both distributions (green line in the lower right panel of Figure 3.7):

$$P_{\text{wake}}(d \,|R_{\text{wake}}, d_{\text{p-wake}}, \Delta_{d_{\text{p-wake}}}) = \Phi(d \,|\, d_{\text{p-wake}}, \Delta_{d_{\text{p-wake}}}) \cdot \Psi(d \,|\, R_{\text{wake}}). \tag{3.5}$$

The probability for wake encounter at a certain altitude is given by the maximum of this distribution. We consider every data point as potentially wake affected, where $P_{\text{wake}} > 5\,\%$.

The exemplary balloon wake encounter shown in Figure 3.7 has a vertical extend of 15 m with a sharp lower and upper boundary of the region. The mean probability for encountering the balloon's wake in this altitude region is comparatively high at 47 %. The spectrum of the raw data resembles the spectrum of atmospheric turbulence with a low signal to noise ratio (i.e. low dissipation rate and/or high altitude).

3.2.2 Statistical evaluation of wake encounter probability

In order to acquire typical values for wake encounter probability, we evaluate a dataset of thirty radiosondes taken during the GW-LCycle II campaign in January/February 2016 in Kiruna (Northern Sweden), using the wake evaluation tool outlined in Section 3.2.1. The further treatment of the dataset is described in Söder et al. (2019). With our wake evaluation tool we calculate the percentage of potentially wake affected altitude bins and the mean wake probability as shown in Figure 3.8. Both values are obtained for payload-balloon distances between 20 m and 200 m and averaged over all flights of the dataset and all altitudes.

For a typical radiosonde with a payload-balloon distance of $d_{\text{p-bal}} = 55\,\text{m}$, we find a mean probability for wake encounter of 28 % and see that about 96 % of all altitude bins are potentially wake affected. For older radiosondes with $d_{\text{p-bal}} = 30\,\text{m}$, these values rise to 40 % and close to 100 %, respectively. For larger payload-balloon distances the values decrease to an average wake probability of 8.8 % with 66 % of all altitude bins being certainly wake free for $d_{\text{p-bal}} = 200\,\text{m}$.

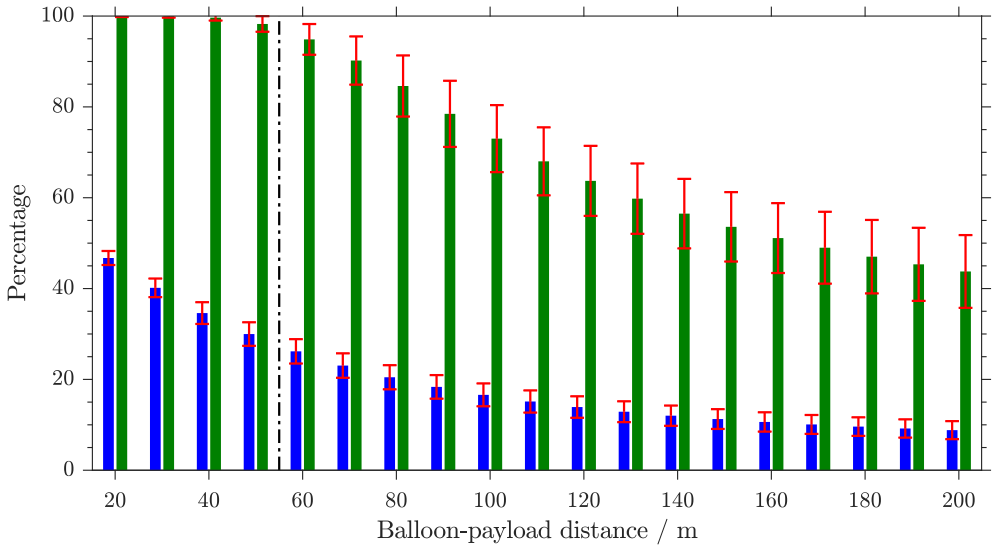

Figure 3.8: Blue: Mean probability of wake encounter using background information from 30 radiosondes flights. Green: Percentage of potentially wake affected altitude bins ($P_{\text{wake}} > 5\,\%$). Red: Standard deviation between different launches. Black: payload-balloon distance of a standard radiosonde. Adapted from Söder et al. (2019).

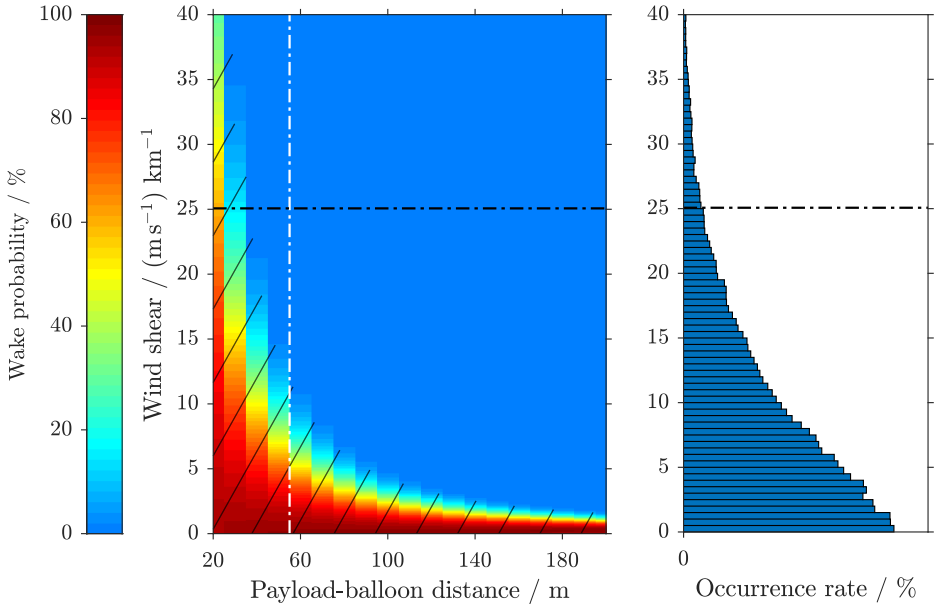

Figure 3.9: Wind shear influence on the wake probability P_{wake} (no wind rotation, relative vertical balloon velocity w_{rel}: $5\,\text{m}\,\text{s}^{-1}$). The ninety-fifth percentile of the measured wind shear is indicated by the black dashed-dotted line. Left: Wake probability as a function of the magnitude of the wind shear and payload-balloon distance $d_{\text{p-bal}}$. The white line denotes the horizontal balloon gondola distance for the RS41 radiosonde, the hatched area is potentially affected by the balloon's wake ($P_{\text{wake}} > 5\,\%$). Right: Wind shear from the 30 radiosonde observations mentioned in Section 3.2.2. Adapted from Söder et al. (2019).

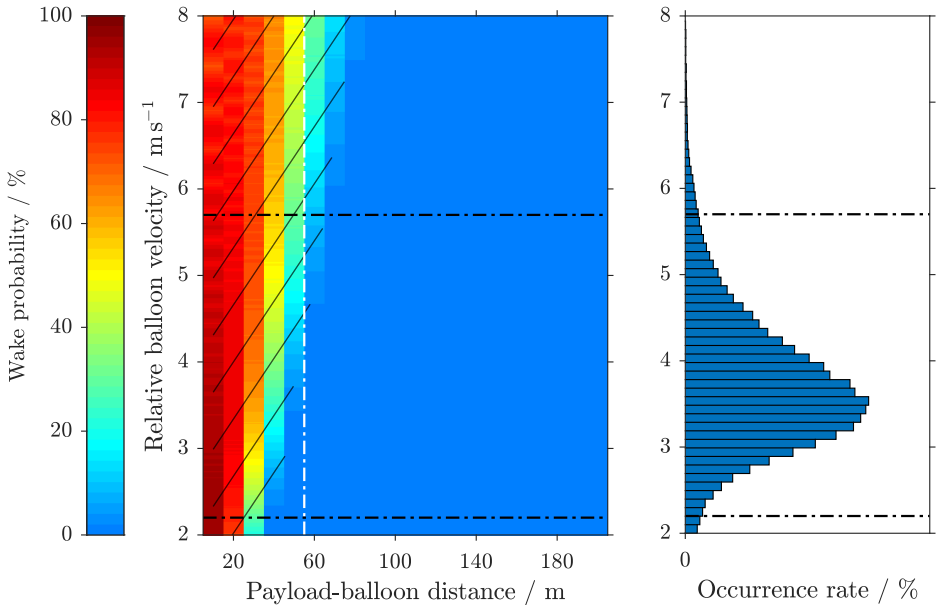

Figure 3.10: Same as Figure 3.9, but showing the influence of the relative vertical balloon velocity w_{rel} on the wake probability (wind shear: $10\,\mathrm{m\,s^{-1}\,km^{-1}}$, no wind rotation).

3.2.3 Influence of the payload-balloon distance for idealised soundings

Within this section, we summarise influences from geophysical and instrumental parameters that affect the probability for wake encounter. Namely, we present the influence of wind shear and the relative vertical velocity between the balloon and the atmosphere w_{rel}. For the influence of further parameters, please see Söder et al. (2019).

In order to investigate the influence of wind shear on the wake encounter probability P_{wake}, the left panel of Figure 3.9 shows P_{wake} as a function of vertical shear of the horizontal wind for typical payload-balloon distances $d_{\mathrm{p-bal}}$. Here, we apply the wake detection algorithm outlined in Section 3.2.1 to an artificial dataset based on standard radiosonde balloons weighing 500 g and having ascent rates of $5\,\mathrm{m\,s^{-1}}$. Furthermore, we assume no rotation of the wind vector. The right panel shows the occurrence rate of the wind shears used in the left panel from the above mentioned radiosonde dataset for comparison. From Figure 3.9, we see that for a typical radiosonde with $d_{\mathrm{p-bal}} = 55\,\mathrm{m}$, uncritical conditions are only reached if the wind shear is larger than $12\,\mathrm{m\,s^{-1}\,km^{-1}}$ ($P_{\mathrm{wake}} < 5\,\%$). From the right panel we note that this is the case for about 30 % of the radiosonde dataset. Within the ninety-fifth percentile of the wind shear measurements from the radiosonde dataset, the wake probability changes from 0.1 % to 96 %.

A similar analysis for relative vertical velocity of the radiosonde w_{rel} is shown in Figure 3.10 for a typical wind shear of $10\,\mathrm{m\,s^{-1}\,km^{-1}}$. Under these conditions, only relative vertical velocities below $\sim 4\,\mathrm{m\,s^{-1}}$ allow for wake free measurements on a standard radiosonde. Within the ninety-fifth percentile of the relative vertical velocities measured in the radiosonde dataset we found wake probabilities ranging from 0.5 % to 43 %. Please note that Figure 3.10 is different from Söder et al. (2019, Figure 8). We found a plotting error in the publication, but it does not significantly compromise either the results in the paper nor the wake detection algorithm published online.

3.2.4 Discussion on wake influences from the balloon

As previously mentioned, there are several articles in the literature that deal with influences of the balloon's wake on balloon-borne measurements. One of the earliest is Barat et al. (1984). They calculate the distance between the payload and the wake $d_{\mathrm{p-wake}}$ from a wind shear measurement on board of their gondola (Barat and Genie, 1982). Barat et al. (1984) state that turbulence retrievals from altitude bins with $d_{\mathrm{p-wake}} < 2D_{\mathrm{bal}}$ are likely to be affected by the balloon's wake. We extended their approach by considering vertical winds in our retrieval and by switching to a probabilistic approach that accounts for the variable diameter of the wake due to the chaotic nature of turbulence, for self-induced balloon motions and for the uncertainties in our calculation.

In order to evaluate the prediction skill of our algorithm it would be desirable to identify wake related turbulence encounters in a LITOS dataset and then compare them to the wake prediction algorithm. One example is given in Figure 3.7. However, such examples where the measured turbulence can be unambiguously related to the balloon's wake are rare. I.e. in many cases we see a correlation but cannot prove a causal relationship. This is because, in contrast to the wake from smaller objects, we did not find any recognisable spectral shape of the balloon's wake. Only very short balloon wake encounters can be manually detected. They are recognised by their small vertical extend of only a few ten meters. The ability to detect balloon-wake in the LITOS data is further reduced because the sensor on an ascending payload is usually blind for about one-third of the time due to the stronger wake from smaller objects. Therefore, we conclude that we found many instances of good agreement between wake-related turbulence measurements with LITOS and our wake prediction algorithm as examplarily shown in Figure 3.7. Nevertheless, it is hardly possible to do a sound statistical correlation for each altitude bin individually.

What we can do, however, is a qualitative comparison of the turbulence data between flights with high average wake encounter probabilities and wake free measurements on descent. Figure 3.11 shows scatter plots of logarithmic dissipation rate over wind shear for different LITOS launches. In order to clearly show the effects of wake related turbulence, we choose four extreme examples: two BEXUS launches with strong wake influences due to low payload-balloon distances of about 70 m and two wake-free descent measurements. An intermediate case is the launch from 29 January 2016 that is used in Chapter 5. Due to the larger balloon-payload distance, balloon-wake related measurements show lower dissipations rates because of the logarithmic decay of turbulence intensity with time (Gibson and Lin, 1968, data not shown here). For the purpose of avoiding influences from the rarification of the flow on our results, we show only data where the Knudsen number around the wire is below 10^{-1}. Please, see Section 2.5 for an explication.

In the atmosphere, Kelvin-Helmholtz Instabilites (KHIs) are the predominant generation mechanism of turbulence (e.g. Fritts and Alexander, 2003). In an elementary picture, they occur if $Ri < 1/4$. For the qualitative picture given in Figure 3.11 we only consider the influence of wind shear on the Richardson number for a better comparison with wake related turbulence. The general expectation is to find stronger dissipation rates with increasing wind shear. This is the case for both measurements from descending balloons shown in the lower part of Figure 3.11. Both flights show the same order of magnitude for the slope of the linear regression, even though they are made under different geophysical conditions and with different electronics (c.f. Section 2.4.1). For wake related turbulence, however, we expect the turbulence strength to be independent of the wind shear. This is because the question whether the sensor is hit by the wake or not is governed by statistical processes and

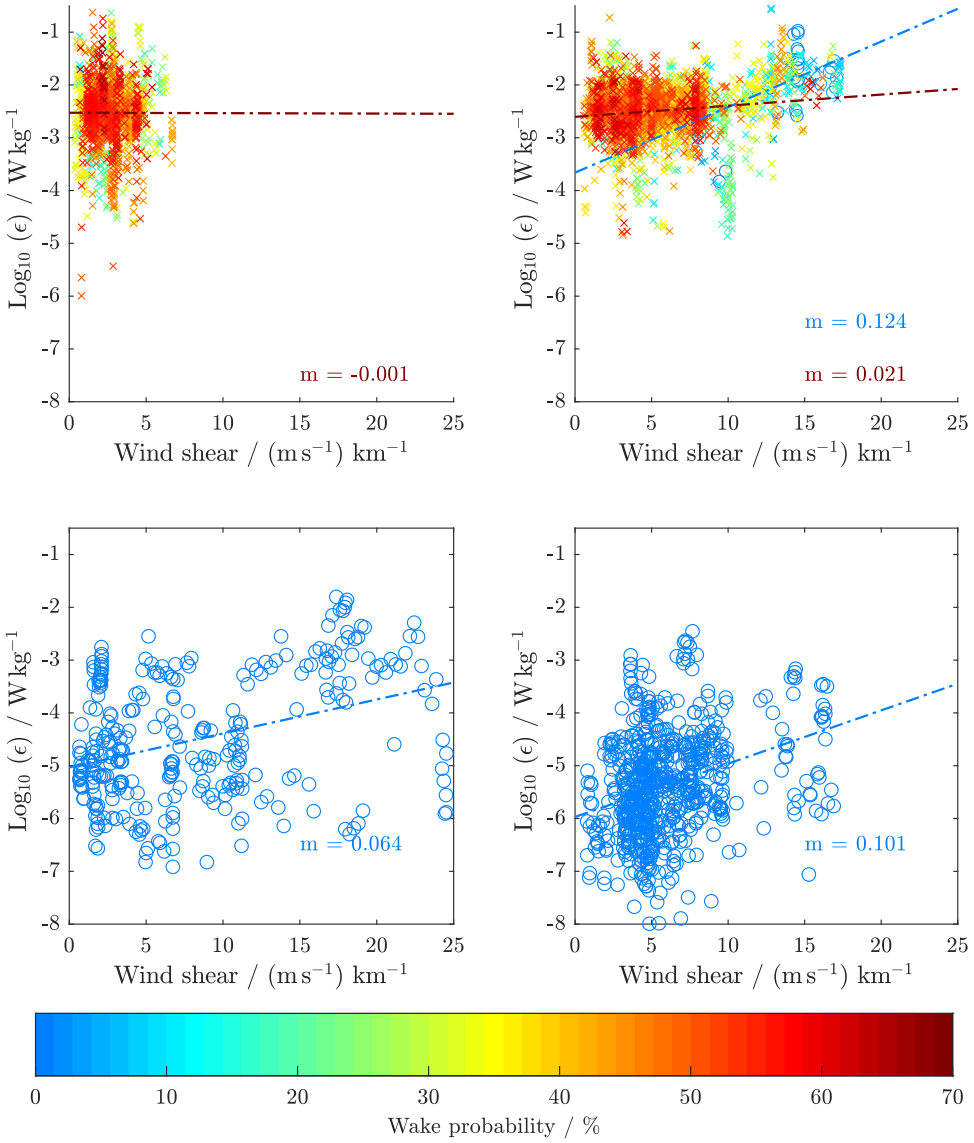

Figure 3.11: Scatter plots of logarithmic dissipation rate versus wind shear. Each cross marks a potentially wake affected measurement ($P_{\text{wake}} > 5\,\%$), each circle a wake free measurement ($P_{\text{wake}} < 5\,\%$). Dashed-dotted lines denote linear orthogonal regressions of wake-free data (blue) and potentially wake affected data (dark red), respectively. The slope of every regression is given in the lower right corner of each panel. Top left: BEXUS 08 data acquired on 10 October 2009 during ascent. Top right: BEXUS 12 from 27 September 2011, ascent. Lower left: 06 August 2016, descent. Lower right: 14 November 2018, descent.

by the wind shear. We expect the percentage of wake affected altitude bins to decrease with increasing wind shear (c.f. Figure 3.9). The turbulence strength, however, only depends on the constant distance between the payload and the balloon.

During BEXUS 08 (Figure 3.11, top left), the wind shear was so low that no certainly wake free altitude bins are found. As expected, the slope of the regression curve is negligible. During BEXUS 12, higher wind shears were present, leading to 2.0 % of all altitude bins to be considered certainly wake free. Their regression shows a slope in the same order of magnitude as both descent measurements. The slope of the regression for $P_{\text{wake}} > 5\,\%$ on the contrary is much lower but still larger than for BEXUS 08. Especially for wind shears above $10\,\text{m}\,\text{s}^{-1}\,\text{km}^{-1}$ there are many measurements showing wake probabilities between 5 % and 40 %. Probably some of them are not caused by wake but by atmospheric turbulence. Due to our conservative approach of considering $P_{\text{wake}} > 5\,\%$ as potentially wake affected, these measurements cause a slope of our wake-data regression that is higher than the result from BEXUS 08.

In conclusion, Figure 3.11 shows that there are wake influences from the balloon on ascending payloads that manifest in a serious amount of false turbulence detections and in an enhanced wake probability according to our algorithm presented in Section 3.2.1. Our careful error analysis and the results from the BEXUS 12 launch make us confident that the algorithm is able to identify wake free altitude bins. Mainly due of self-induced balloon motions, however, we cannot single out wake affected altitude bins with certainty. This is because the width of the wake is in the same order of magnitude as the amplitude of those self-induced motions. This is inherent to measurements on rising balloons. It cannot be overcome by an improved wake retrieval method or a better instrumentation.

For the LITOS flight from 29 January 2016, with a payload-balloon distance of 180 m, we find 69 % of all altitudes bins to be certainly wake free ($P_{\text{wake}} < 5\,\%$). However, Barat et al. (1984) find 90 % of the sounding to be wake free for a similar balloon size and a payload-balloon distance of 100 m. Combining their payload-balloon distance of 100 m with our statistical radiosonde dataset (for wind shear, ascent rate etc.), we find that on average only 27 % of all altitude bins are certainly wake free. There are several reasons for the considerable increase in percentage of potentially wake affected bins. In contrast to Barat et al. (1984), we consider self-induced motions of the balloon, vertical winds and the uncertainty in our calculation. Furthermore, we replaced their heuristic criterion for the minimal payload-balloon distance by a description of the transversal shape of the wake obtained from laboratory experiments (Gibson and Lin, 1968; Riddhagni et al., 1971). Therefore, our higher number of potentially wake affected altitude bins also reflects the level of uncertainty in the calculation that is mainly caused by self-induced balloon motions.

Contrary to our results, Azouit and Vernin (2005) find that for a payload balloon-distance of 50 m and an ascent rate of $4\,\text{m}\,\text{s}^{-1}$, only 2 % of all altitude bins are affected by the balloon's wake by the criterion of Barat et al. (1984). This extremely low percentage is probably due to their much higher average wind shear compared to our radiosonde dataset ($\sim 30\,\text{m}\,\text{s}^{-1}\,\text{km}^{-1}$ vs. $9.1\,\text{m}\,\text{s}^{-1}\,\text{km}^{-1}$).

Comparing different measurements from ascending balloons, we expect the balloon's wake to have the strongest influence on high resolution turbulence soundings that cover the small-scale end of the inertial subrange and possibly the viscous subrange. This is the case because, for a balloon diameter between 2 m and 13 m (depending on altitude) the average wake diameter at the position of the gondola 180 m below the balloon will be around 4 m and 15 m, respectively (Riddhagni et al., 1971, Figure 5.5). Accordingly, the largest isotropic eddies will be between 4 m and 15 m in diameter. Therefore, the energy will

mainly be deposited on scales that are resolved by high-resolution turbulence measurements like LITOS.

Due to the severity of wake influences on the high-resolution measurements of BEXUS 08 and BEXUS 12, geophysical results from Theuerkauf et al. (2011), Theuerkauf (2012), Haack et al. (2014), Schneider et al. (2015) and Schneider (2015) become questionable due to influences from the balloon's wake. Schneider et al. (2017) already used a precursor version of the wake detection algorithm presented in Section 3.2.1 and is therefore considered reliable.

In order to completely avoid any wake influence on our turbulence measurements we adopt a method proposed by Kräuchi et al. (2016) and further described in Section 2.1. We lift our payload up to the ceiling altitude using two balloons and cut one of them away. The amount of lifting gas in the remaining balloon is such that it descents at about $5\,\mathrm{m\,s^{-1}}$. With the sensors measuring the unperturbed flow below the balloon, all wake influences are certainly avoided. Another idea to avoid influence from the balloon's wake on turbulence measurements is given by Kyrazis et al. (2009). They mounted their instruments on an inflatable ring tethered a few meters below an ascending balloon. The ring diameter of 9 m however will make handling difficult during launch. Furthermore, this would have required a technical redesign of the LITOS instrument. Therefore, we choose to use the method proposed by Kräuchi et al. (2016).

3.2.5 Balloon-wake influences on radiosonde measurements

The statistical evaluation of a set of 30 radiosondes (Section 3.2.2) shows that the average probability for wake encounter decreases with increasing payload-balloon distance as expected and as previously stated by Barat et al. (1984). Furthermore, an increased payload-balloon distance will also reduce the dissipation rate in case of wake encounter. This is due to the logarithmic decay of the dissipation rate with time (Gibson and Lin, 1968). However, a contemporary standard radiosonde uses a payload-balloon distance of only 55 m (Survo et al., 2014). This results in only 4 % of all altitude bins to be certainly wake free and in an average wake probability of about 28 %. From the evaluation of artificial datasets in Section 3.2.3, we note that among the investigated parameters the vertical shear of the horizontal wind has the strongest influence on wake encounter probability, followed by the ascent rate of the balloon. We would like to stress, however, that ascent rate is the only parameter that can be modified by the operator. Reducing the ascent rate from $5\,\mathrm{m\,s^{-1}}$ to $3\,\mathrm{m\,s^{-1}}$ reduces the wake encounter probability from 35 % to 6.5 % for a typical wind shear of $10\,\mathrm{m\,s^{-1}\,km^{-1}}$.

However, the balloon's wake does not only influence high resolution turbulence measurements. A literature survey reveals that temperature and humidity measurements from radiosondes are affected as well. Tiefenau and Gebbeken (1989) report daytime heating and nighttime cooling due to radiative heating of the balloon's skin and adiabatic cooling of the lifting gas during ascent, respectively. Due to the radiosonde swinging in and out of that wake with its pendulum frequency they found temperature oscillations on the data with half the pendulum period (i.e. 5.5 s for $d_{\mathrm{p-bal}} = 30\,\mathrm{m}$). During daytime, another artificial temperature signal at the pendulum frequency is discovered by the authors. Consequently, Luers and Eskridge (1998) emphasise that different radiosondes with different payload-balloon distances will show other temperature biases due to the balloon's wake that need to be considered when their data are used for climate studies. Similarly, Gaffen (1994) reports that a lengthening of the radiosonde cord easily leads to discontinuities of

long term temperature records of about 1 K. Jumper and Murphy (2001) compare ascent and descent measurements from thermosondes. Consistent with the other results mentioned here, they find more small-scale temperature spikes on their ascent data compared to descent measurements in the troposphere due to the balloon's wake. These effects are not limited to temperature measurements. According to Kräuchi et al. (2016) the balloon's wake affects humidity measurements as well, because humidity is collected on the balloons skin and subsequently continuously released into the wake.

Accordingly, also lower resolution turbulence retrievals from radiosondes using Thorpe-analysis are likely to be affected by the balloon's wake. This is because they infer kinetic turbulent dissipation rates from the temperature measurement of a radiosonde. For method and error treatment of the Thorpe analysis, please see for example Wilson et al. (2010) and Wilson et al. (2011). The 5.5 s and 11 s temperature distortion reported by Tiefenau and Gebbeken (1989) are well below the common 1 Hz sampling rate of a radiosonde. Therefore, an influence of the balloon's wake is anticipated. This becomes even more likely for high-resolution Thorpe-analyses featuring a 10 cm vertical grid step and payload-balloon distance of 100 m (Luce et al., 2001; Gavrilov et al., 2005).

These findings may also impact later studies that retrieve turbulence climatologies from Thorpe analyses of standard radiosondes (Ko et al., 2019; Zhang et al., 2019b). The authors retrieve energy dissipation rates from routine radiosonde soundings mainly above the United States. The measurements are provided by the SPARC[1] data centre. While especially Ko et al. (2019) perform a very careful error analysis, they do not take into account possible influences from the balloon's wake. The same is true for a study on the ratio between Ozmidov and Thorpe length that has recently become available (Zhang et al., 2019a).

3.2.6 Summary on ballon-wake influences

In conclusion we have seen from the data presented in Figure 3.11 as well as from our calculation on the likelihood of wake encounter and from a literature survey on radiosonde measurements that the balloon's wake will significantly impact turbulence measurements from ascending balloons. In order to avoid these effects, one should preferably measure on descent. If not possible, all potentially wake affected altitude bins need to be detected using an algorithm like the one presented in Section 3.2.1 and subsequently be excluded from the geophysical interpretation.

[1] Stratosphere-troposphere Processes and their Role in Climate

4 Comparison between LITOS and HYFLITS

LITOS provides an established platform for atmospheric turbulence measurements in the troposphere and the lower stratosphere (e.g. Schneider, 2015). There has been a detailed investigation of benefits and limitations of the instrumental design by Theuerkauf et al. (2011). However, those investigations where limited to theoretical considerations and experimental verifications of the CTA-principle for various pressures and temperatures. Prior to this work, there has been no cross-comparison between LITOS and any other turbulence measuring instrument. Cross-comparisons under controlled laboratory conditions seem desirable. However, wind tunnels that can be operated at pressures between $1\,\mathrm{hPa} < p < 1000\,\mathrm{hPa}$ and temperatures between $180\,\mathrm{K} < T < 300\,\mathrm{K}$ are rare. Developments achieving these goals have been made by Wilson et al. (2008) and more recently by Xie et al. (2017). However, currently we have no access to such a device. Therefore, we were glad to be offered the opportunity of taking part in a joint measurement campaign with the balloon-borne HYFLITS (Hypersonic Flight in the Stratosphere) turbulence sensor from University of Colorado Boulder (USA). This campaign took place at different locations in the state of Mecklenburg-Vorpommern (Germany) in November 2018. We included both LITOS and HYFLITS in a single payload. A picture of the sensors taken during launch preparations in the course of that campaign can be seen in Figure 4.1.

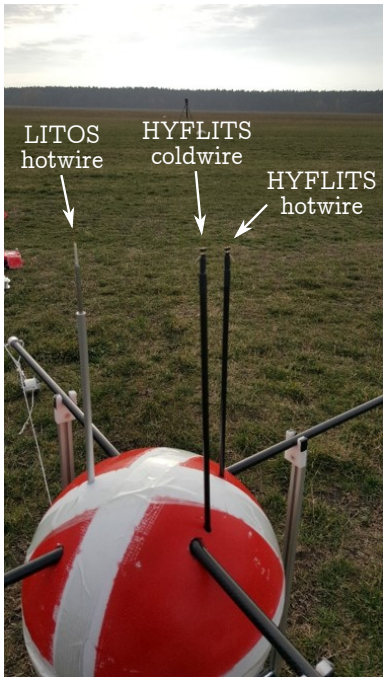

Figure 4.1: Combined LITOS-HYFLITS payload shown upside down. Picture courtesy of Dale A. Lawrence.

In order to allow for a statistical evaluation of our cross-comparison, we will use the Pearson correlation coefficient r as a measure for the linear correlation between two variables x and y.

4.1 Payload design

HYFLITS features a hotwire sensor like LITOS (constant temperature anemometer, CTA) and one coldwire (constant current anemometer, CCA). The instrumentation is an advanced version of the electronics used on DataHawk. DataHawk is an unmanned aerial vehicle (UAV) designed to measure kinetic energy dissipation rates, the temperature turbulence structure constant C_T^2 and other parameters in the lower troposphere (Lawrence and Balsley, 2013). The C_T^2 measurement allows to retrieve the thermal dissipation rate

as previously done on balloons by Barat and Bertin (1984), for example. Deriving the kinetic energy dissipation rate ε from C_T^2 is technically possible, but not reasonable because amongst other "constants" this method relies on the Richardson number Ri of the flow as well as on the turbulent Prandtl number (Pr_θ^{turb}). These quantities can only be poorly estimated and cannot be considered constant (Lübken, 1992). As there is no C_T^2 measurement on the LITOS instrument, we will focus on ε retrieved from velocity fluctuations here.

Whereas LITOS calculates ε from a fit of the inner scale of turbulence l_0, HYFLITS provides a calibrated measurement of velocity fluctuations in the small scale part of the inertial subrange. Therefore, the structure function constant for velocity fluctuations C_v^2 can be obtained from the fluctuations measured with HYFLITS. Subsequently, ε is calculated from C_v^2. Even though the noise floor of the HYFLITS instrument is higher than the noise floor of LITOS, HYFLITS can also resolve parts of the inertial subrange. Therefore, a comparison of the two methods using HYFLITS seems possible. Both methods require knowledge of the same empirical constant a_v^2. Therefore, they are equivalent under the assumption that the Heisenberg (1948) model of turbulence is correct.

As mentioned above, the ε retrieval of HYFLITS depends on a calibration of the CTA for all relevant temperature and pressure regimes. In the planetary boundary layer such a calibration was done in situ using a Pitot tube wind sensor (Muschinski et al., 2001; Frehlich et al., 2003). This does not work on a sounding balloon in the stratosphere, however, because the current technological state of differential pressure sensors does not allow a Pitot tube that can measure velocities as low as a few meters per second at a pressure of 10 hPa to be built. The approach taken with the HYFLITS instrument is to pre-calibrate the electronics in an open blow-down vacuum chamber. In this wind tunnel, an empirical Nusselt number is obtained as a function of altitude and velocity. This allows for a calibration of the CTA wind measurements as briefly outlined in Section 1.2. The wind tunnel's design is similar to the one presented by Xie et al. (2017). The general idea is to create a pipe flow from a gas cylinder containing dry air to a vacuum pump. This allows the pressure to be adjusted to within the required range by flow controllers between the air reservoir and the test section. The temperature is controlled by a heat exchanger mounted upstream of the test section, cooled with liquid nitrogen. The velocity in the centre of the pipe, where the CTA sensor is mounted, can be calculated for a fully developed pipe flow by measuring the mass flow entering the pipe and the pressure in the test section.

Figure 4.2: Left: LITOS hotwire sensor. Right: HYFLITS hotwire sensor.

Figure 4.2 shows both the LITOS and the HYFLITS hotwire sensors. LITOS uses a gold plated tungsten wire Dantec 55P01. In Figure 4.2 one can see that the middle section of the sensor is thinner than the outer part connected with the prongs. This reduces the heat flow into the prongs as well as flow interferences caused by eddies from the prongs. Due to their gold plating, the LITOS sensors can be operated at a comparatively high overtemperature of 300 K, increasing the signal to noise ratio (SNR). The HYFLITS sensors are made of unplated tungsten by the University of Colorado and operated at an overtemperature of 50 K. These lower overtemperatures are possible because, due to the different retrieval strategy, HYFLITS

does not need to resolve as much of the viscous subrange as LITOS. Accordingly, the HYFLITS sensors can be made at a fraction of the cost of the Dantec 55P01. This highlights different development targets for both instruments. LITOS is made to allow for relatively few high-resolution turbulence measurements with as little designing cost as possible. Therefore, operational costs are a secondary priority. On the other hand, HYFLITS pursues the same goal of high-resolution turbulence measurements with a more time-consuming development, but at a lower operational cost. A possibility to further reduce the lower detection limit in ε would be to combine both approaches. Using the LITOS electronics in combination with the HYFLITS retrieval method would further increase the SNR and reduce the risk of influences from flow rarefication (Section 2.5).

4.2 Joint measurement from 14 November 2018

Within the course of our joint campaign in November 2018, three flights were carried out. Due to malfunctioning balloons, only one of them reached its desired top altitude and descent rate. Therefore, our analysis is concentrated on the measurement on 14 November 2018. The balloon was launched in Kühlungsborn (Mecklenburg-Vorpommern, Germany) and headed south-east. The payload shown in Figure 4.1 contained both the LITOS and the HYFLITS system. LITOS was flown in the latest development stage as introduced in Section 2.4. Due to governmental restrictions on payload weight however, we used just one CTA instead of two as on previous measurements. This is not critical because, due to the wake free descent measurement, there are no major distortions of the data.

Figure 4.3 shows both dissipation rates from LITOS and HYFLITS together with background information from a Väisälä RS-41 radiosonde. Turbulent patches that show a distinctly higher dissipation rate compared to their surroundings are marked by grey colour shading. The dissipation rate measurement is discontinued below 2.5 km altitude, because at that height the descent continued on parachute after the second balloon has been cut away. Due to strong sporadic motions of the payload under the parachute, these data cannot be used for turbulence retrieval. The radiosonde wind profile reveals a tropopause jet with a core velocity of slightly above $40\,\mathrm{m\,s^{-1}}$. All tropospheric turbulence is below the median value for *light* turbulence according to Sharman et al. (2014). In the troposphere, there are two distinct areas of reduced Richardson number around 4.3 km and 9.1 km, respectively. In the stratosphere, there are more instances, possibly due to a background modulation by gravity wave activity. In both tropospheric instances Ri is smaller than one but larger than 0.25. This is true for the 500 m smoothing length as well as for 1000 m. Both cases reveal dissipation rates around $0.1\,\mathrm{mW\,kg^{-1}}$, even though the classical criterion for dynamic instability ($Ri < 0.25$) is not met.

Generally, we find that reduced Richardson numbers occur in the marked patches of enhanced dissipation rates in the measurement on 14 November 2018. This corresponds to the lower right panel of Figure 3.11, where a positive correlation of dissipation rate with wind shear is shown.

An exemplary zoom up on the lowest turbulent patch in the troposphere is shown in Figure 4.4. Here we find a double layer structure in the dissipation profile between 4 km and 4.8 km. The lower one of these layers, however shows considerably stronger peak dissipation rates ($\sim 10^{-3.5}\,\mathrm{W\,kg^{-1}}$ vs. $\sim 10^{-4.5}\,\mathrm{W\,kg^{-1}}$). Each of these layers shows a smooth increase in dissipation rate from lower altitudes and a sharp drop at the upper edge. The reason for this feature is not understood yet. The whole structure looks very similar

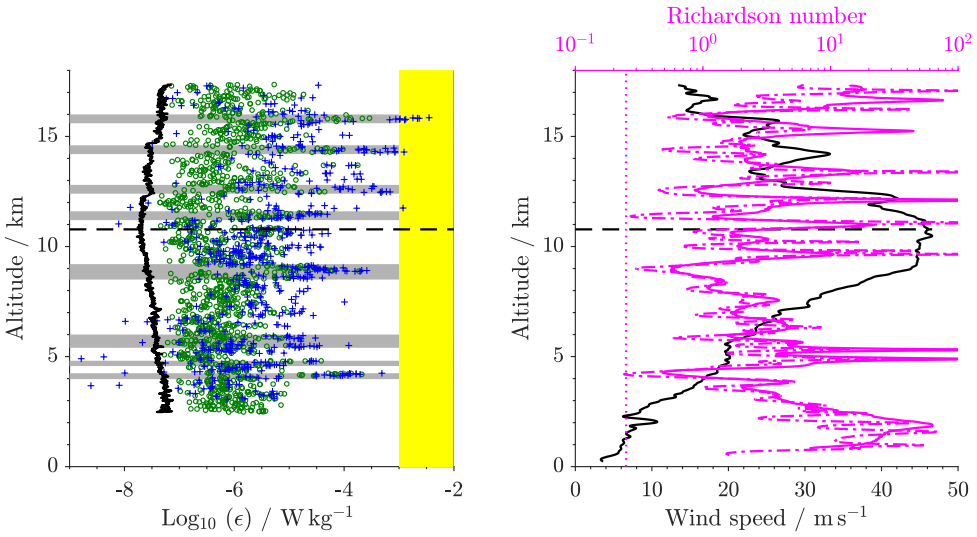

Figure 4.3: Left: Turbulence profile on 14 November 2018. Blue crosses denote turbulent altitude bins measured by LITOS, green circles show turbulent bins measured by HYFLITS. The solid black line marks the lower detection limit of HYFLITS. Grey colour shading highlights turbulent patches, yellow colour shading marks light to moderate turbulence intensity according to Sharman et al. (2014). Right: Solid black line denotes wind speed, solid magenta *Ri* calculated over 1000 m and dashed-dotted magenta *Ri* calculated over 500 m. Dotted magenta line shows critical *Ri* of 0.25. Both: Tropopause marked by dashed black line.

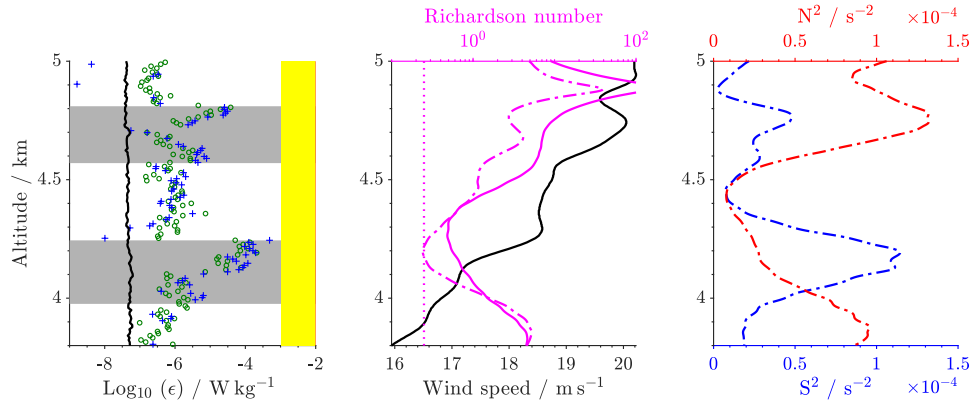

Figure 4.4: Left and middle: Same as Figure 4.3, but zoomed in on two turbulent patches in the troposphere. Right: squared buoyancy frequency N^2 and squared vertical shear of horizontal wind S^2 with 500 m smoothing.

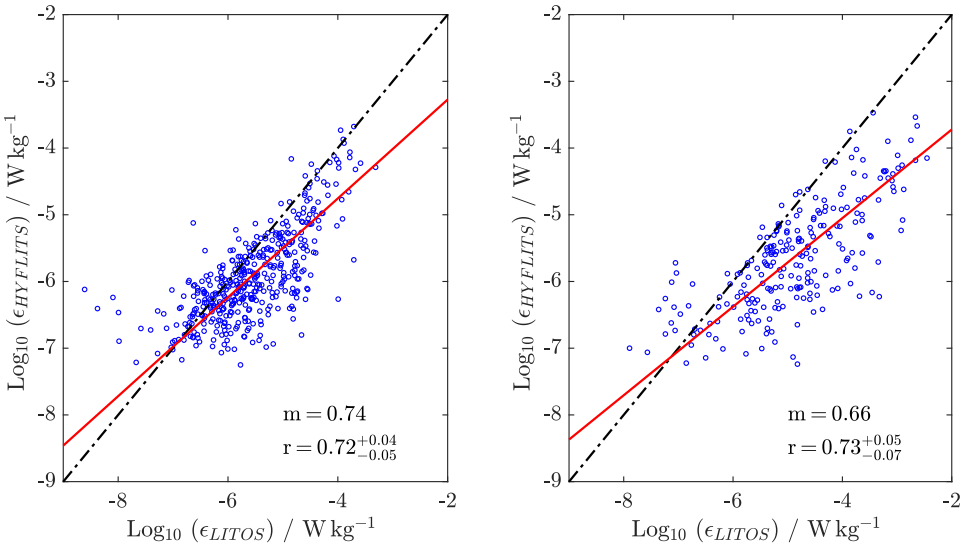

Figure 4.5: Correlation of all logarithmic dissipation rates measured with LITOS and HYFLITS. Each blue circle marks a turbulent altitude bin. The black dashed-dotted line shows an ideal correlation of one, the red line denotes a linear orthogonal regression. The correlation coefficient r and the slope of the regression m are given in the lower right corners. Subscript and superscript numbers denote the uncertainties for a 95 % confidence level. Tropospheric data are shown on the left, stratospheric data on the right.

to what is expected in a Kelvin-Helmholtz instability (KHI). Fritts et al. (2003) performed incompressible direct numerical simulations (DNSs) of such an instability. They will be further discussed in Section 4.3 along with similarities and differences to the measurement.

The original plan for our November 2018 campaign, however, was not the investigation of fundamental turbulence generation mechanisms, but the intercomparison of LITOS and HYFLITS. Accordingly, Figure 4.5 shows the correlation of ε measurements from both instruments. In the troposphere and the stratosphere we find similar correlation coefficients of $r = 0.72^{+0.04}_{-0.05}$ and $r = 0.73^{+0.05}_{-0.07}$, respectively (Subscript and superscript numbers denote the uncertainties for a 95 % confidence level). The steepness of the linear orthogonal regression is smaller than one in both cases ($m = 0.74$ vs. $m = 0.66$). Possible implications of these findings are given in Section 4.3.

As already mentioned in the discussion of Figure 4.3, we identified several turbulent patches. In order to investigate whether some of the differences between the LITOS and the HYFLITS measurement are dependent on the turbulence event, Figure 4.6 shows the correlation of both instruments for all regions of enhanced turbulence that have been marked in Figure 4.3. Compared to all turbulence measurements, the mean correlation coefficient of all turbulent patches in the troposphere is slightly higher ($r = 0.82^{+0.05}_{-0.06}$). Furthermore, the slope of the regression, including turbulent patches only, is higher compared to the data from Figure 4.5, even though the difference is not significant for a 95 % confidence level. In the stratosphere, the picture is slightly different. The correlation coefficient of $r = 0.71^{+0.09}_{-0.11}$ is very similar to the dataset including all turbulence measurements, whereas the slope of the regression is slightly enhanced ($m = 0.79$ vs. $m = 0.66$). We conclude that

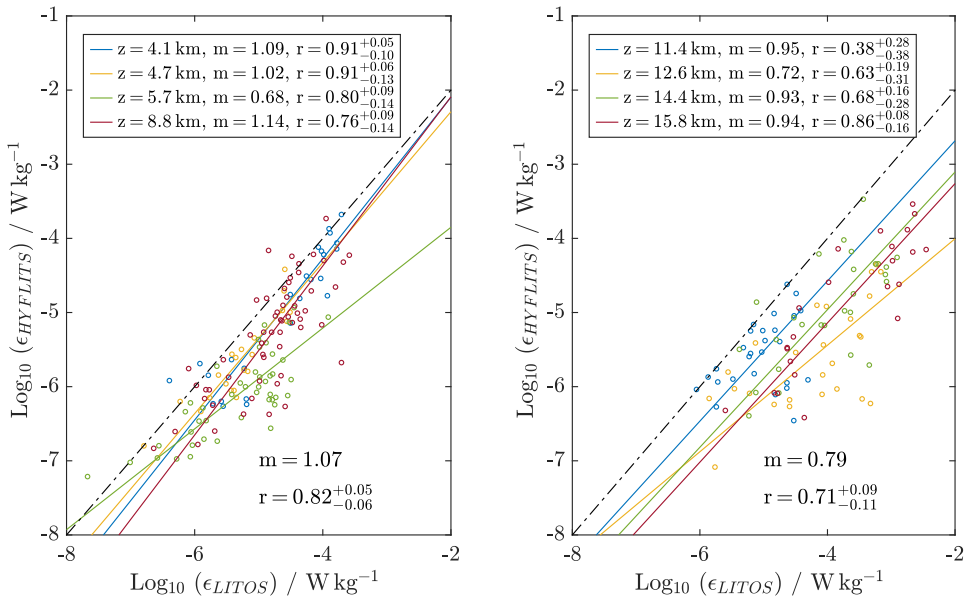

Figure 4.6: Same as Figure 4.5, but for regions of enhanced turbulence only. The mean altitude of each region is given in the legend. The text in the lower right corner shows correlation coefficient r and the slope of the regression over all turbulence measurements from within a turbulent patch.

the deviation in the slope of the regression from the ideal case of $m = 1$ is reduced, if only patches of enhanced turbulence are considered.

Investigating the individual tropospheric patches shown in the left panel of Figure 4.6, we find that the correlation coefficient diminishes with increasing altitude. The slope is slightly above one for all patches, except the one around 5.7 km altitude. In the stratosphere, we find increasing correlation coefficients with altitude, with the lowest correlation of only $r = 0.38^{+0.28}_{-0.38}$ around 11.4 km altitude. Usually, the slope is slightly below $m = 1$ with a lower slope of $m = 0.72$ at 12.6 km altitude.

4.3 Discussion

Generally, we find a reasonably good correlation ($r = 0.71$) for this intercomparison of two independent turbulence measurements on a single payload. More specifically, we note that for small dissipation rates $\varepsilon_{\text{LITOS}} < \varepsilon_{\text{HYFLITS}}$, whereas for large dissipation rates $\varepsilon_{\text{LITOS}} > \varepsilon_{\text{HYFLITS}}$ ($m < 1$). This is true if we consider all turbulent altitude bins as done in Figure 4.5. Furthermore, there is a general tendency for $\varepsilon_{\text{LITOS}} > \varepsilon_{\text{HYFLITS}}$. Overall, we find better agreement at lower altitudes (c.f. Figure 4.3).

Accordingly, we identify two types of deviation in our comparison: **first the deviation in the slope** of the regression curve from the ideal slope ($m < 1$) and **second the overall offset** of the regression curve towards $\varepsilon_{\text{LITOS}} > \varepsilon_{\text{HYFLITS}}$.

From our point of view, the most plausible reasons for the **deviation in the slope** is on the side of the LITOS instrument. We expect an attenuation of the wire signal at higher frequencies as discussed in Sections 2.5.3 and 2.5.4. Such a phenomenon was also reported

by Li (2004) for low SNR measurements. The effect is stronger in altitude bins with low dissipation rates, because the decreased SNR reduces the quality of the spectral fit and the relative influence of the heat flow into the prongs is increased (Section 2.5). This attenuation at high frequencies would result in an artificially low inner scale l_0 and therefore in $\varepsilon_{\text{retrieved}} < \varepsilon_{\text{real}}$ for small dissipation rate measurements. This point is underlined by the data shown in the left panel of Figure 4.6. For all tropospheric cases in distinct turbulent patches (meaning high SNR) the slope of the regression is close to one. This hints that indeed LITOS may underestimate dissipation rates in low SNR measurements. This analysis calls for the development of a better discrimination criterion for low SNR measurements. This however would require a full error analysis, which unfortunately cannot be done in the time frame of this thesis (see below).

A possible cause for the **overall offset** could be imperfections in the calibration of the HYFLITS instrument. However, because this instrument as well as the calibration chamber have been developed by the University of Colorado Boulder, we cannot give further details on the calibration process or possible improvements.

The reduced slope of the regression for the turbulent patch around 5.7 km altitude (Figure 4.6) is probably caused by the low dissipation rate of the patch leading to a lower SNR measurement. The same occurs for the patch around 12.6 km, where we cannot suggest a reason. The low correlation coefficient at $z = 11.4$ km is most likely a result of the low variability of the dissipation rates in the turbulent patch.

From a geophysical point of view, the most interesting phenomenon in the measurement on 14 November 2018 was the occurrence of a Kelvin-Helmholtz instability in altitudes between 4.0 km and 4.8 km. Measurements of Kelvin-Helmholtz instabilities have been reported before (e.g. Coulman et al., 1995; Klostermeyer and Rüster, 1980; Cho et al., 2003), but our case shows a comparatively low dissipation rate never exceeding $1\,\text{mW}\,\text{kg}^{-1}$. We observed this Kelvin-Helmholtz instability in an area with $Ri > 0.25$, where no turbulence is expected in the classical picture of the Richardson criterion. We see two possible reasons for this discrepancy. First it could be due to the 500 m smoothing being still too rough to see strong local gradients in wind and temperature. Cho et al. (2003), for example, used a 100 m vertical scale to calculate Ri from aircraft data. They confirm that the occurrence rate of $Ri < 0.25$ strongly depends on the vertical spacing of the calculation (Cho et al., 2003, Figure 5 e). However, such small smoothing lengths are not reasonable when using radiosonde data, because they increase the risk of misinterpreting instrumental effects for geophysical measurements. The second point is made by Achatz (2007): in short, he argues that looking at the Richardson criterion alone is not sufficient to exclude gravity wave breaking. Even for $Ri > 0.25$ horizontal gradients may lead to gravity wave instability and turbulence production.

Fritts et al. (2003) performed DNSs of such a KHI. Due to computational limitations at that time, their Reynolds number had to be lower than typical Reynolds numbers of KHIs in the troposphere. They roughly represent the mesopause region. However, the general picture is expected to be similar at lower altitudes. For an early stage of a KHI (about two buoyancy periods after initialisation) they find maxima of kinetic dissipation ε and thermal dissipation χ at the edges of the billow. Potential temperatures are isothermal throughout the layer with strong small scale gradients at the edges, leading to a low static stability N^2 in the centre of the billow. They expect small-scale wind fluctuations with high shear at the edges and a larger-scale wind shear in the middle of the billow.

Figure 4.4 shows a similar profile: ε as measured by LITOS and HYFLITS alike shows maxima at the edges. The static stability N^2 is minimal in the centre of the billow around

4.45 km. We measure maxima of the wind shear at the edges of the billow. This may be caused by small-scale secondary instabilities that developed at the edges of the billow in the simulation by Fritts et al. (2003). This, however, cannot be clearly identified because the altitude resolution of our radiosonde wind measurement is not sufficient for that task. In contrast to Fritts et al. (2003), we do not see a maximum of the larger-scale shear in the centre of the billow. Similar observations of Ri, the potential temperature θ and the temperature structure function parameter C_T^2 have been made by Coulman et al. (1995).

After this first intercomparison between LITOS and HYFLITS we intend to undertake the following steps for a second phase of our measurement campaign:

- Develop error analysis for LITOS:
  As outlined in Section 2.5.4 we intend to introduce a full error analysis of the LITOS measurement. The fit error shall be obtained using a Monte-Carlo-type method. An error propagation will allow us to state a minimal measurable dissipation rate ε and an uncertainty in ε for each altitude bin.

- Launch in conditions that foster turbulence:
  Currently we plan to sound a tropopause fold with the combined LITOS/HYFLITS instrument. Tropopause folds are well known to be accompanied by turbulence (e.g. Keyser and Shapiro, 1986). Therefore, we expect higher dissipation rates that will allow to clarify whether the remaining differences between the LITOS and the HYFLITS measurement mainly occur in low dissipation rate and low SNR cases, or whether there are other causes.

- HYFLITS calibration and turbulence retrieval:
  The team from CU Boulder proposed to further develop their calibration (Dale A. Lawrence, private communication). Due to time limitations, the HYFLITS ε from fitting the inner scale l_0 of the turbulent spectrum has not been used in this comparison. However, this may reveal worthwhile information on the applicability of the Heisenberg (1948) model, because both dissipation rate retrievals rely on the same empirical constant a_v^2 (c.f. Section 1.2.1). Furthermore, this dataset could be used to compare the results from the Heisenberg (1948) to the Tatarskii (1971) model.

5 Case study on mountain wave related turbulence

It is widely accepted that the momentum deposition in the mesopause region by breaking gravity waves controls not only the dynamic but also the thermal structure of the middle and upper atmosphere (e.g. Holton and Alexander, 2000). One of the main contributors to gravity wave pseudo-momentum fluxes are mountain waves (e.g. Fritts and Alexander, 2003). As stationary mountain waves have a phase speed of $c = 0$, they reach a critical level and break if the background wind speed U approaches zero (Section 1.1, Eq. 1.1). This wave breaking marks the end of the gravity wave life cycle, which was investigated during the GWLCYCLE II[1] campaign in the Winter 2015/16 (e.g. Krisch et al., 2017; Dörnbrack et al., 2018). This campaign was combined with field investigations using our LITOS instrument as part of the METROSI project (mesoscale processes in troposphere-stratosphere interaction).

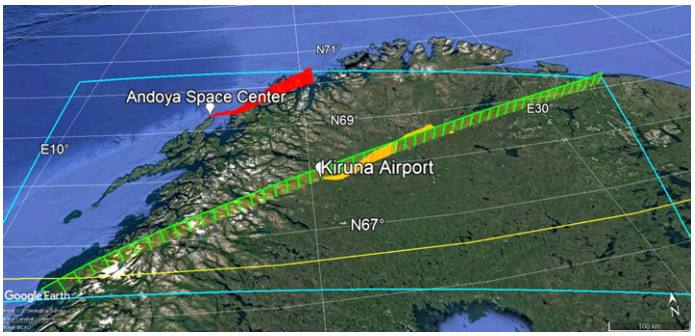

Figure 5.1: Area of joint METROSI-GWLCYCLE II campaign on 29 January 2016. LITOS launched at 10:42 UT shown in orange, radiosonde launched at 09:57 UT shown in red. Bounding box of WRF-Simulations shown in light blue, sectional plane of Figure 5.4 shown in light green.

The role of our instrument was to observe the aforementioned end of the gravity wave life cycle, where it breaks down into turbulence. During that campaign we were kindly invited by the team of DLR-IPA Oberpfaffenhofen, Germany to launch two balloons from their campaign site at Kiruna in northern Sweden. A further set of four LITOS balloons and several radiosonde were launched from Andenes on the island of Andøya. An overview of the campaign area is shown in Figure 5.1. On 29 January 2016, we performed a LITOS sounding reaching 32 km altitude. At an altitude of 30 km, we encountered a distinct turbulent patch that coincided with a reduction in background wind speed to about 18 m s^{-1} (Figure 5.2).

As mentioned above, in the classical case of a wind reversal in the stratosphere, the gravity wave breaks and deposits its momentum in the altitude of the reversal. No so-called *deep propagation* of the waves into the mesosphere takes place (Booker and Bretherton, 1967). In our measurement we observed a wind minimum but no wind reversal. This wind minimum was co-located with turbulence. The question is, whether the co-location was coincidental or causal.

[1] gravity wave life cycle

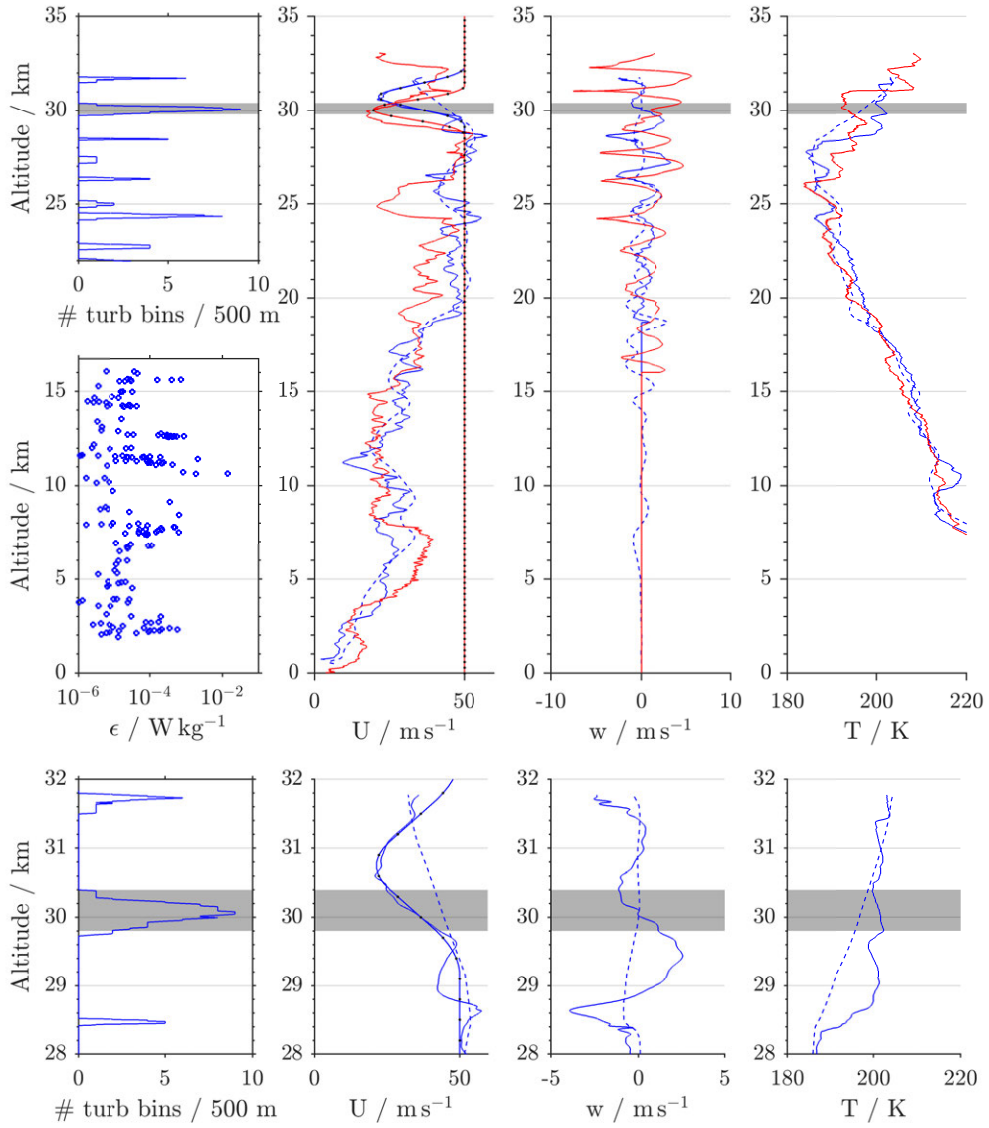

Figure 5.2: LITOS and radiosonde measurements on 29 January 2016. All data from Kiruna are marked blue, data from Andenes red. The lowermost panels provide a zoom of the turbulent region in the Kiruna data. Middle left: Dissipation rate measurement from LITOS. Every blue cross marks a turbulent bin of 2 s length. Upper left: Number of turbulent altitude bins per 500 m altitude interval acquired from LITOS. Please see main text for details. Mid-left: wind speed data. Idealised profiles for the large eddy simulation (LES) marked with black dots. Mid-right: Vertical winds. Right: temperatures. Solid lines denote radiosonde data, dashed lines show WRF data interpolated on the LITOS flightpath.

The conditions under which deep propagation occurs were one of the main targets of an extensive field campaign called DEEPWAVE (Fritts et al., 2016). It was situated around the Southern Alps in New Zealand. In the course of that campaign, Kruse et al. (2016) introduced a concept to the attenuation of mountain waves called *valve layer*. The basic idea is that not only a critical layer will lead to mountain wave breaking, but that a reduction of the background wind speed to $10 - 15\,\mathrm{m\,s^{-1}}$ in altitudes between 15 km and 25 km forms a *valve layer*, which under certain conditions inhibits deep propagation of gravity waves into the mesosphere by attenuating their amplitudes. This is schematically shown in Figure 5.3. Depending on the minimum wind speed and the low-level forcing, Kruse et al. (2016) find ratios for the zonal pseudo-momentum flux below and above the event between 0.05 and 0.95. Accordingly, their case study is very similar to ours in terms of the minimum wind speed, but clearly differs in the vertical extend of the *valve layer* (10 km vs. 2.5 km in our case). This leads us to the following questions that shall be examined in this chapter:

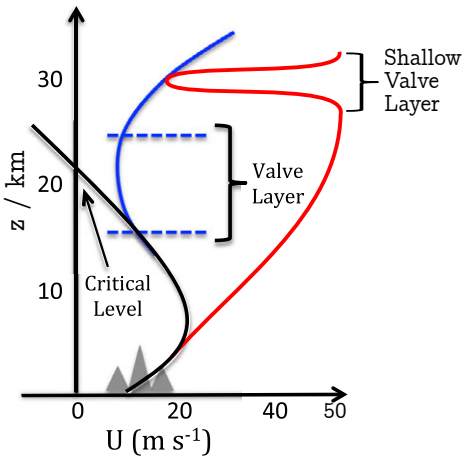

Figure 5.3: Schematic visualisation of critical level and a *valve layer* taken from Kruse et al. (2016). The *shallow valve layer* has been added by the author of this thesis.

- What are the primary components of the gravity wave field that contribute to this turbulence event?
- Can the background wind reduction be understood as a *shallow valve layer* and as the cause for wave attenuation with subsequent turbulence generation (c.f. Figure 5.3)?

The campaign has been performed with the old version of the LITOS instrument. Accordingly, the old data retrieval scheme had to be used (c.f. Section 2.4). As the measurement was taken on an ascending balloon, all quality control measures to avoid wake influence are applied prior to geophysical interpretation, as described in Chapter 3. Furthermore, density reduction and flow rarefication may influence the absolute value of the retrieved energy dissipation rate ε. Therefore, we abstain from retrieving ε in altitudes above 16.7 km ($Kn < 0.1$), as discussed in Section 2.5.4. This represents a conservative approach in order to avoid any influence of low Kn effects on our interpretation and may be reversed once a full uncertainty analysis for our turbulence retrieval has been developed.

For this case study, the gravity wave field is depicted by mesoscale numerical simulations with the WRF[2] model, version 3.7 (Skamarock et al., 2008). The model set-up is similar to the one used in Schneider et al. (2017). However, in this study three nested domains (d01, d02 and d03) with horizontal resolutions of 7.2 km, 2.4 km and 800 m are applied. Here, we show only results from the innermost domain. In the vertical direction 138 terrain following levels with stretched level distances of 80 m near the surface and 300 m in the stratosphere are used. The model top is set to 2 hPa (about 40 km altitude). At the model top, a 7 km thick Rayleigh damping layer is applied to prevent wave reflections (Klemp et al., 2008). Physical parametrisations contain the Rapid Radiative Transfer Model longwave

[2]Weather Research and Forecasting, https://www.mmm.ucar.edu/weather-research-and-forecasting-model (Last accessed: 26/11/19)

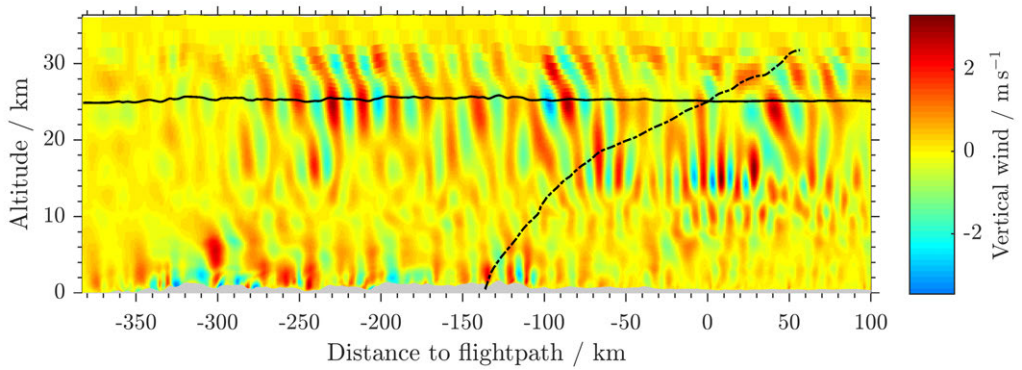

Figure 5.4: Vertical winds for 29 January 2016, 12:00 UT from the WRF model. The picture plane is along the horizontal wind on a model plane around 25 km altitude(solid black line, light green polygon in Figure 5.1). Negative distances denote locations upstream of the LITOS track (dashed-dotted line).

scheme (Mlawer et al., 1997), the Goddard shortwave scheme (Chou and Suarez, 1994), the Mellor-Yamada-Nakanishi-Niino boundary layer scheme (Nakanishi and Niino, 2009), the Noah land surface model (Chen and Dudhia, 2001) and the WRF single-moment 6-class microphysics scheme (WSM6; Hong and Lim, 2006). The initial and boundary conditions are supplied by ECMWF[3] operational analyses on 137 model levels with a temporal resolution of 6 hours. A temporal output interval of 5 minutes is used. The simulation runs for 30 hours and was initialised the day before the balloon was launched at 28 January 2016, 18 UT. These simulations have been kindly provided by Johannes Wagner, DLR Oberpfaffenhofen, Germany.

5.1 The predominant mountain wave

As depicted in Figure 5.2, the LITOS flight from Kiruna and the radiosonde launch from Andenes both clearly show prominent wave activity at altitudes above 20 km. Vertical winds have been acquired according to Söder et al. (2019). At a first glance, both flights show a wave with an apparent vertical wavelength of $\lambda_z \approx 2$ km visible in U, w and T. Another wave with $\lambda_z \approx 5$ km is predominantly visible in U. This wave is in phase with the above mentioned reduction of the background wind speed to 18 m s^{-1}. In order to further investigate the smaller-scale wave we use vertical winds from WRF shown in Figure 5.4. They are shown in a plane following the horizontal wind on a model level at an altitude of approximately 25 km (light green polygon in Figure 5.1). This allows us to conveniently depict mountain waves, because they propagate against the horizontal wind (e.g. Nappo, 2012). In Figure 5.4, a dominant wave structure with slightly changing vertical wavelengths is clearly visible. From the WRF data we find the phase of this wave to be constant in time for several hours (data not shown here). Therefore, we assume that this wave is a mountain wave (MW). The average wavelength in altitudes above 20 km is $\lambda_x \approx \lambda_z \approx 20$ km. This begs the question of how this complies with the apparent $\lambda_z \approx 2$ km from the radiosonde data?

The key to answering this question is the flightpath of the radiosonde through the wave

[3]European Centre for Medium-Range Weather Forecasts

field. The WRF data reveal a phase line steepness of $m = \frac{\lambda_z}{\lambda_x} \approx 1$, yielding an intrinsic wave frequency of $\omega = \frac{N}{2} = 16 \cdot 10^{-3}\,\mathrm{s}^{-1}$ (c.f. Eq. 1.4) and a wave period of about eight minutes above 20 km. The steepness of the flightpath in the relevant altitude range above 20 km on the other hand is $\frac{\text{height of flight}}{\text{range of flight}} \approx \frac{1}{9}$. Hence, the phase lines are much steeper than the flightpath. Accordingly, the radiosonde measurement cannot be treated as a vertical transect through the wave. The awareness of similar effects has been raised by Shutts et al. (1988); Reeder et al. (1999) and Lane et al. (2000). They propose a so called horizontal projection method, where they calculate wave properties neither as a vertical section nor as a horizontal section of the wave, but map the observed wave vectors onto a horizontal grid. For simplicity, we will not adopt this approach here, but treat the flightpath as a horizontal section through the wave. Due to geometry, this may slightly underestimate horizontal wavelengths by less than one percent for the given steepnesses of the flightpath and the phaselines ($\frac{1}{9}$ and ~ 1, respectively). This deviation of measured to true wavelengths is certainly not crucial.

Furthermore, the slant angle of our flightpath and the short horizontal wave length mean that we cannot obtain any vertical derivatives of the wave field. Especially important for turbulence measurements, this consequently also inhibits the calculation of Richardson numbers.

Concerned with the excitation of the wave with $\lambda_x \approx \lambda_z \approx 20\,\mathrm{km}$, we expect that it was not triggered by the flow over the whole mountain range, because this would lead to a horizontal wavelength roughly equivalent to the horizontal scale of the whole mountain range ($\sim 300\,\mathrm{km}$). Instead it is rather excited by the flow into and out of individual valleys, which are a few ten kilometres wide. This has also been described by Smith and Kruse (2017) and has been named the *roughness mode* of the wave spectrum.

In order to identify the horizontal wavelengths of the gravity wave patterns seen in Figure 5.2, we show a wavelet analysis of the radiosonde data in Figure 5.5. Before calculating the power spectra, the radiosonde data have been linearly regridded from constant time scales to constant horizontal spacing. Here, the distance from launch point can be taken as the horizontal coordinate, because there was hardly any change in wind direction during the flight (c.f. Figure 5.1). As argued above, this regridding is needed because, with respect to the dominant mountain wave, we need to examine horizontal instead of vertical scales. We find enhanced power spectral densities at altitudes above 26 km and in a horizontal wavelength regime from 15 km to 30 km. A large part of this regime is within the wavelet's cone of influence (calculated according to Torrence and Compo, 1998). Therefore, this wavelet analysis will be used to give a rough estimate of the horizontal scales of the mountain wave only. Vertical winds are available above 21 km only, because their retrieval is overlayed by self-induced balloon motions in lower altitudes (Section 2.6.1 and Söder et al. 2019).

Please note that the description given here is true for the patch labelled *MW* in Figure 5.5. For other patches we would need to identify whether the radiosonde has to be treated as a vertical or as a horizontal section through the wave field. If for example one of these patches were caused by a low-frequency gravity wave with $m = \frac{\lambda_z}{\lambda_x} \approx\!\ll 1$, the radiosonde flightpath would need to be treated as a vertical section of the wave structure. Nevertheless, the occurrence of these patches already hints that there were more waves present during that flight.

The inverse Scorer (1949) parameter is depicted by the red line in Figure 5.5. A short introduction to this parameter is given in Section 1.1. The inverse Scorer parameter marks

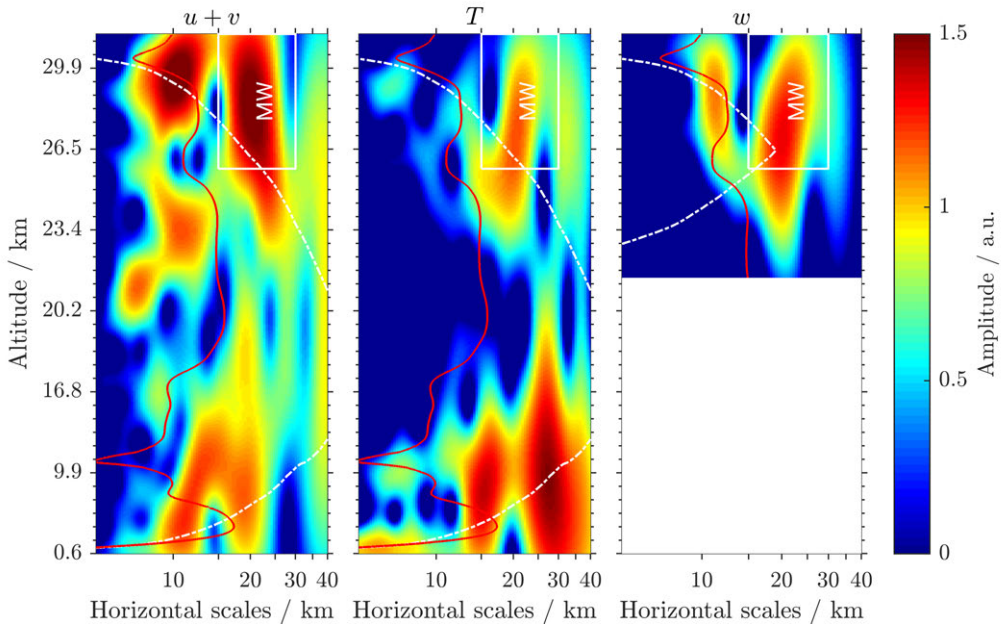

Figure 5.5: Wavelet power spectra of radiosonde data from LITOS launch on 29 January 2016 using a complex Morlet wavelet. Added power spectra of zonal and meridional wind shown in the left panel, temperature data in the middle panel and vertical wind data in the right panel. The inverse Scorer parameter is shown by the red line, the wavelet's cone of influence by the white dashed-dotted line. The area of the mountain wave's hodograph shown in Figure 5.6 is denoted by a white box. Please note, that the y-axis shows a none linear altitude scale due to regridding and changing ascent rates.

the shortest horizontal wavelength, that allows for vertical propagation of mountain waves. From Figure 5.5 we find that the observed mountain wave with $\lambda_x = 20\,\text{km}$ is close to the shortest wavelength that can propagate vertically from the ground to 30 km. Additionally, in altitudes between 7 km and 18 km waves of $\lambda_x = 10\,\text{km}$ may propagate vertically. Indeed, these wave lengths are visible in the WRF and radiosonde data in this altitude range. Similar trapped lee waves have been investigated, for example, by Shutts and Broad (1993). However, as these additional waves do not significantly contribute to the understanding of the observed turbulent patch in a wind minimum they shall not be discussed further.

In order to investigate whether the regime of enhanced power spectral density highlighted in Figure 5.5 is indeed caused by a mountain wave, we plotted hodographs of zonal wind versus meridional wind as well as vertical wind versus temperature in Figure 5.6. As there are several wave-like disturbances present on the radiosonde data, we need to extract the relevant wavelength range from the regridded radiosonde data. This is done by a third-order digital Butterworth band-pass filter with the lower and upper cut-off wavelengths set to 15 km and 30 km, respectively. The method of using a band-pass filter has been successfully applied to atmospheric data before (e.g. Tsuda et al., 1990). We perform a zero phase filtering by applying the filter both in forward and reverse direction on the data. This technique avoids phase shifts in the filtered data as well as it yields more precise cut-off frequencies and a steeper roll-off of the transfer function compared to spline subtraction. Boundary effects of the filter are counteracted by data padding. We mirror the original data at the boundaries of the data set with a length of half the upper cut-off scale of the

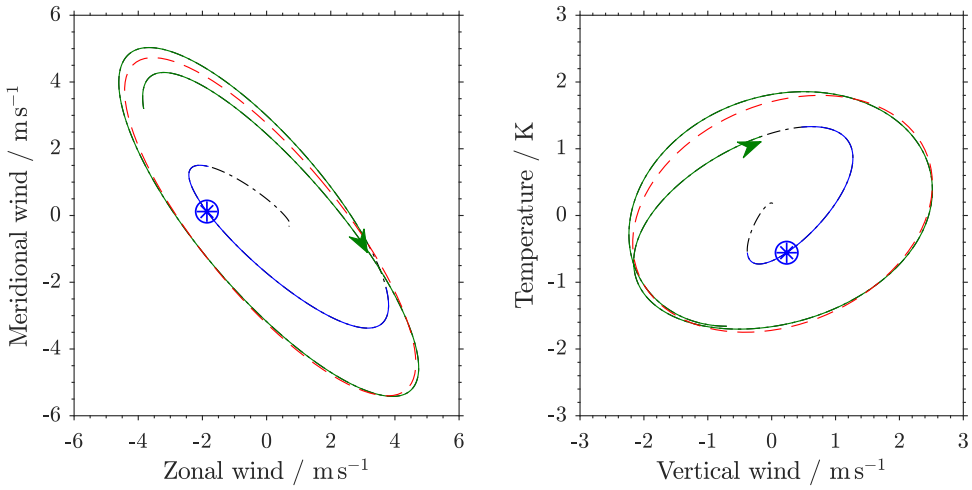

Figure 5.6: Hodographs for the wavelength-altitude regimes marked by white boxes in Figure 5.5. The green line denotes altitudes from 26.0 km to 28.5 km. They have been used for the ellipse-fit (red). Blue lines highlight the altitude range of the wind minimum (28.7 km to 31.1 km). The dashed-dotted black line shows the remaining part of the hodograph. The green arrow highlights the direction of the hodograph. The circled blue star marks the altitude of the turbulent patch highlighted in Figure 5.2. FIX ARROW POSITIONING

band-pass.

Both panels of Figure 5.6 show an ellipse shape, indicating that the wave extracted from the radiosonde data indeed follows the phase relations of a gravity wave (e.g. Nappo 2012, p.54; Sutherland 2010, p.159 ff.). The reduction in the amplitude of the ellipse above 31.1 km already hints an attenuation of the gravity wave. Further below, we will use these filtered wind data to estimate the pseudo-momentum fluxes of the gravity wave below and above the wind minimum. The rightward turning direction of the (u, v)-hodograph indicates a downward phase propagation and an upward energy propagation (e.g. Dutta et al., 2009).

Coming back to the *valve layer* concept of Kruse et al. (2016), we will compare gravity wave pseudo momentum fluxes below and above the suspected *valve layer* in order to identify wave attenuation. Due to our vertical wind retrieval according to Söder et al. (2019), we are able to apply Equation 1.6 directly instead of retrieving w from temperature fluctuations using GW polarisation relations as for example done by Vincent and Alexander (2000).

5.2 Wave-turbulence interaction

GW amplitudes are inferred from the data underlying Figure 5.6 and displayed in Table 5.1. From Figure 5.6 we find that the attenuation of the u and v amplitudes begins exactly at the height where the wind minimum commences. Even though the attenuation of T amplitudes starts a quarter of a wave cycle earlier, we take this as a hint that the wave attenuation and the background wind reduction are connected.

Table 5.1 reveals that the mountain wave flux above the turbulence event is only 8.4 %

		Below turbulent layer	Above turbulent layer
u'	$/\,\mathrm{m\,s^{-1}}$	5	2
w'	$/\,\mathrm{m\,s^{-1}}$	2.2	1
MF_x	$/\,\mathrm{hPa}$	25	2.1
Ratio	$/\,\%$	8.4	
GWD	$/\,\mathrm{m\,s^{-1}\,d^{-1}}$	610	

Table 5.1: Characteristics of the dominant mountain wave extracted from the LITOS measurement on 29 January 2016.

of the value below the events, thus revealing a considerable attenuation of the wave. For a better classification of our measurement, we will compare it to the *valve layer* study by Kruse et al. (2016):

Our measured pseudo-momentum flux below the suspected *valve layer* ($\mathrm{MF}_x = 25\,\mathrm{hPa}$) is at the upper edge of what has been reported by Kruse et al. (2016, Figure 13). Nevertheless, our transmission ratio of 0.08 is in accordance with their ratios between 0.05 for a minimum wind speed of $13\,\mathrm{m\,s^{-1}}$ and 0.2 for $22\,\mathrm{m\,s^{-1}}$. This yields a gravity wave drag of $610\,\mathrm{m\,s^{-1}\,d^{-1}}$, which is about two orders of magnitude larger than the $6\,\mathrm{m\,s^{-1}\,d^{-1}}$ they retrieved from WRF simulations of an exemplary event on 24 June 2014. There are several reasons for our higher gravity wave drag (GWD). First, the wind minimum is much shallower in our case (2.4 km vs. > 10 km), therefore, the wave attenuation is confined to a smaller height range, producing higher GWD (Eq. 1.7). Second, their total loss of MF_x in the *valve layer* is only 6 hPa, compared to 23 hPa in our case. Third, they investigate time-averaged values, whereas in our case we consider a snap-shot, which can be subject to transient effects. Furthermore, our measurement ends at the upper edge of the wind minimum. The mountain wave amplitude may partly recover once the wave has passed the minimum. This is also suggested by idealised simulations as discussed below (Figure 5.7).

Regarding further understanding of the wave attenuation, the results obtained with our LITOS instrument can reach beyond Kruse et al. (2016). We are generally able to measure the turbulent energy dissipation rates along the flightpath and compare them to the energy loss of the gravity wave. This would for example allow us to estimate to which extend non-dissipative transient wave-mean flow interactions contributed to observed losses in gravity wave energy. As for example in Bölöni et al. (2016), these effects are increasingly introduced into recent gravity wave parameterisations and therefore observational studies on these phenomena seem relevant. With the current state of the LITOS instrument, however, we cannot carry out such a quantitative comparison in the altitude region of the observed wind minimum due to the above mentioned limitations in low Kn environments. However, the upper left panel of Figure 5.2 shows the highest abundance of turbulent altitude bins in the region of the wind minimum (grey colour shading). This already shows that in the particular case the reduction of gravity wave pseudo-momentum flux was accompanied by turbulence generation.

It is an open question whether gravity wave breaking induced the observed turbulent patch or whether it was caused by other processes like the advection of fossil turbulence. At the first glance this could be investigated using the WRF simulations. When comparing the WRF velocity and temperature fields along the flightpath with our radiosonde data however, we note that in altitudes above 28 km neither the background wind reduction nor

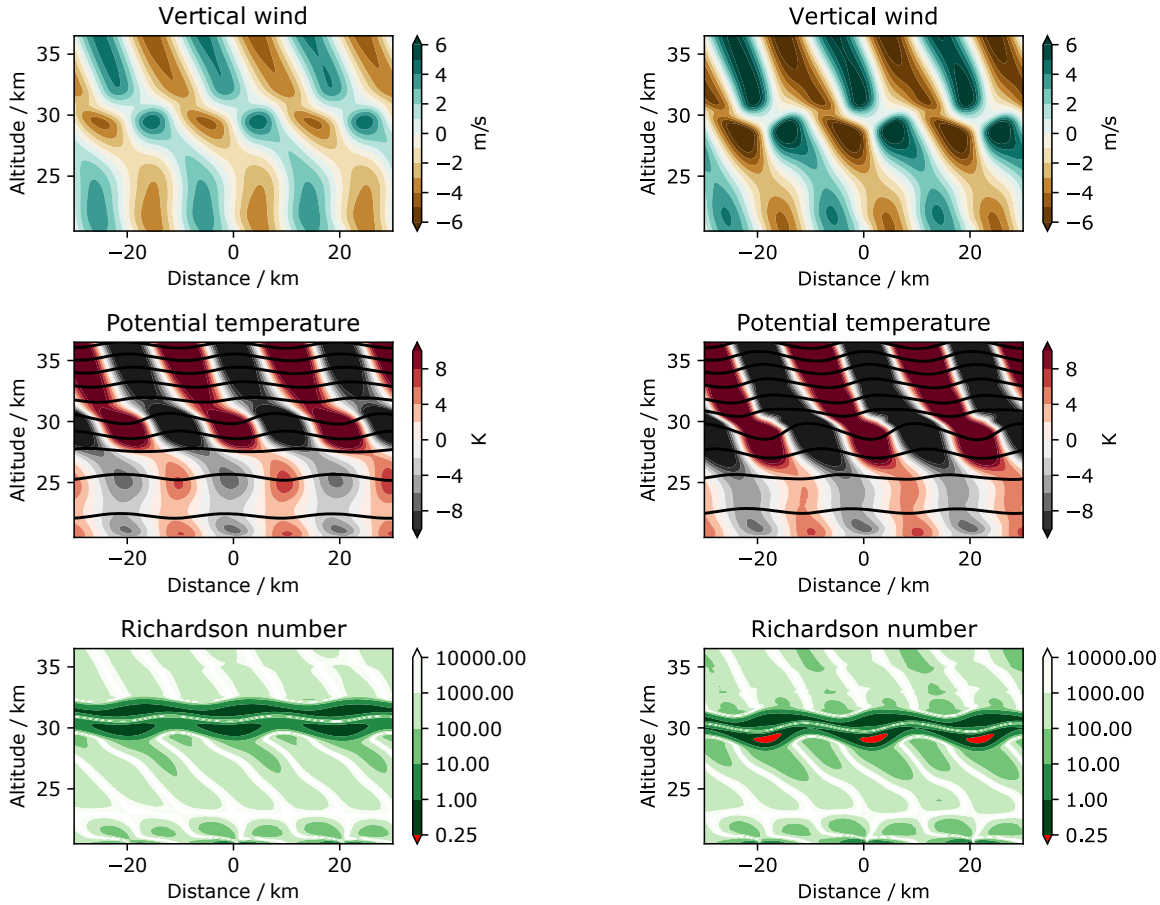

Figure 5.7: Results from the EULAG simulations for the LITOS flight from KIRUNA (left) and radiosonde from Andenes (right). Plots courtesy of Henrike Wilms.

the gravity wave amplitude in w and T are well represented in the model (Figure 5.2). This is primarily caused by the damping layer of the WRF model beginning at 30 km altitude. Therefore, we choose to address this question by the means of idealised EULAG simulations (Prusa et al., 2008).

These EULAG simulations have been kindly set up, run and plotted by Henrike Wilms, previously at DLR Oberpfaffenhofen, Germany. The setup assumes non-hydrostatic equations of motion and is similar to one used by Bramberger et al. (2018). The model includes a subgrid turbulence parameterisation scheme. The idealised background wind profiles for the LITOS launch from Kiruna as well as for the radiosonde from Andenes are depicted in Figure 5.2. The potential temperature profiles are taken from smoothed radiosonde observations (not shown here). The gravity wave in the flow field is induced by a chain of six sinusoidal mountains. The mountain height of ~ 300 m is chosen such that the simulated wave amplitudes shown in Figure 5.7 match the observed ones in altitudes below the wind minimum as displayed in Figure 5.6 (data of the Andenes radiosonde not shown here). At the left, right and upper boundary a damping layer is used in order to avoid unwanted wave reflections.

The EULAG results presented in Figure 5.7 show a reduction in phase line steepness in the region of the wind minimum similar to the WRF model. This is expected from linear wave theory. In comparison with the LITOS measurements the EULAG simulations show

considerably higher wave amplitudes above the wind minimum. A possible cause could be that we are not able to see the full recovery of the wave amplitude above the damping zone in our measurement, because the top height did not exceed the upper boundary of the wind minimum. Furthermore, boundary effects of the filters used to estimate the wave amplitudes might have influenced our results, even though we applied data padding at the ends.

For the LITOS case, the EULAG fields contain Richardson numbers below one in the wind minimum. For the Andenes case, even values below 0.25 occurred due to higher wave amplitudes compared to the LITOS area. From our measurements we find that the altitude of the turbulent patch coincides with the wind speed minimum. The damping of the wave's horizontal wind field starts at the beginning of the wind minimum, while the temperature field is attenuated already slightly below (Figures 5.2;5.6). A similar picture is found in the EULAG simulations.

5.3 Conclusion and outlook

Coming back to the introductory questions of this chapter, we conclude that on 29 January 2016 there was a high-frequency mountain wave present in the lee of the Scandinavian mountains above Kiruna. Due to its high internal frequency, this wave carried comparatively high momentum below the turbulent patch under discussion ($\mathrm{MF}_x = 25\,\mathrm{hPa}$). Kruse et al. (2016) and Bramberger et al. (2017) argue that these waves with high pseudo-momentum fluxes are often considerably attenuated in the lower stratospheric wind minimum called *valve layer*.

In our study we are able to show that this concept not only holds for a wind minimum of about 10 km vertical extend, but also for much shallower cases like ours. Here, the vertical extend of the wind minimum was $\sim 2.4\,\mathrm{km}$, which is only about 1/8th of the vertical wavelength. This implies that not only large scale flows can be expected to create wave attenuation in such a layer. Instead, also other events like a low frequency gravity wave creating a local minimum in the background wind for a mountain wave are found to act as a *shallow valve layer* as depicted in Figure 5.3. Furthermore, we showed with idealised simulations that the observed mountain wave creates Richardson numbers of $Ri < 1$ in the wind minimum at 30 km. Even though the classical criterion of $Ri < 0.25$ is not reached, we can expect the mountain wave to have created turbulence in the wind minimum measured by LITOS. This is especially plausible in the light of the strong horizontal gradients created by the wave (Achatz, 2007).

Therefore, we conclude that this turbulence was not created by a classical critical level but by a valve layer similar to Kruse et al. (2016). Our study was able to show that the vale layer concept can be used for wind minima of small vertical extend, which we call *shallow valve layers*.

If we are either able to improve the behaviour of the LITOS instrument in low Knudsen number conditions (c.f. Section 2.5) or encounter a similar situation at lower altitudes, it would be highly desirable to perform a similar case study with a quantitative comparison of losses in wave energy due to attenuation and the amount of kinetic energy dissipated into heat by turbulent processes. This would possibly allow to quantify the relative influence of transient wave mean flow interactions compared to turbulent wave breakdown for the individual case.

6 Case study on turbulence-tropopause interaction

In this chapter, results from a turbulence sounding within a tropopause fold are presented. The meteorological situation was marked by an upper-level front. The accompanying jet-streak was centred around an altitude of 9.6 km and reached wind speeds of $55\,\mathrm{m\,s^{-1}}$. The measurement took place on 06 August 2016, 15:13 UT to 17:04 UT. Originally, this sounding was not planned as an upper-level front investigation. Instead, it was meant to be a technical test flight. More precisely, it was the first LITOS measurement on a descending balloon that took into account our findings presented in Chapter 3. From the geophysical point of view, our attention was originally triggered by a turbulent patch centred around an altitude of 11 km (see turbulence profile, Figure 6.4). We measured peak dissipation rates around $10\,\mathrm{mW\,kg^{-1}}$. This corresponds to moderate turbulence intensities in the classification of Sharman et al. (2014) for medium sized aircraft and to turbulent heating rates of $\left(\frac{dT}{dt}\right)_{\mathrm{turb}} \approx 1\,\mathrm{K\,d^{-1}}$.

In the course of this chapter, however, we will not follow the classical approach of describing and then interpreting the measurement. Instead, a brief overview of the role of turbulence in the formation of tropopause folds will be given, following the concept of Shapiro (1976). Then the meteorological event will be described using the numerical weather prediction, followed by a description of our LITOS measurement and a discussion of the peculiarities found in the turbulence sounding.

As mentioned above, the measurement under discussion was taken within an upper-level front. As opposed to surface fronts, these weather patterns develop near the tropopause. They may emerge from baroclinic waves and are characterised by large horizontal gradients in wind and temperature. Viewed from above, these features appear to be confined to long, narrow regions. Typical along-front scales are 1000 km to 2000 km whereas cross-front scales tend to be one order of magnitude shorter (100 km to 200 km, Keyser and Shapiro, 1986). The wind field from the 06 August 2016, 16:00 UT can be seen in the left panel of Figure 6.1. The wind field around the flightpath is governed by a jet streak with a south-easterly flow direction.

With the details being laid out below, we briefly mention that a tropopause fold is characterised as a submersion of stratospheric air under the tropopause jet from the cyclonic side of the jet core (e.g. Keyser and Shapiro, 1986, from the North in our case). According to Shapiro (1976), this submersion is driven by turbulent mixing in the shear zones of the jet that is converted into relative vorticity of the flow via the increase of potential vorticity (PV). This generation of relative vorticity results in the formation of a tropopause fold.

As shown in the right panel of Figure 6.1, our LITOS sonde measured a complete transect through the jet that characterised the upper-level front system. Therefore, this is one of the few measurements in tropopause folds where energy dissipation rates or turbulent heat fluxes have been obtained (others are Reid and Vaughan, 2004; Shapiro, 1980; Kennedy and Shapiro, 1975). We will use this opportunity to compare our case study with the model of Shapiro (1976), elaborating similarities and differences as well as possible implications.

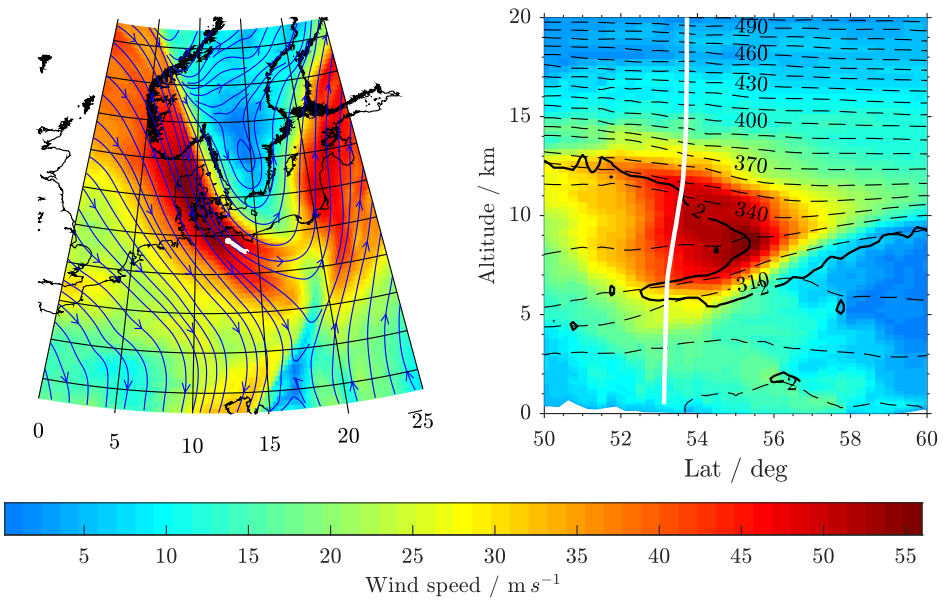

Figure 6.1: Horizontal wind over central Europe on 06 August 2016, 16 : 00 UT at $z = 10$ km. The white lines mark the flightpath of the LITOS sensor. Left: The blue lines indicate the wind direction. Data are plotted along a hybrid level from the ECMWF-IFS. Right: Latitudinal section at 11 °E. Potential temperature is marked by dashed lines, the solid black line denotes the dynamical tropopause at 2 PVU.

6.1 The mesoscale flow in the ECMWF-IFS

In this chapter, we describe the meteorological flow field above Northern Europe on 06 August 2016, where the tropopause fold had developed. This characterisation will be based on the *Integrated Forecast System* of the *European Centre for Medium-Range Weather Forecasts* (ECMWF-IFS), version CY41R2, HRES. The data has been kindly provided by Gerd Baumgarten. The processing, however, is part of this thesis. All data maps shown here are presented in a sigma-coordinate system, meaning that the vertical coordinate is terrain-following at the bottom of the atmosphere, whereby the influence from the terrain is reduced with increasing altitude. A comprehensive documentation of the ECMWF-IFS can be accessed at ECMWF (2019). For simplicity, we will replace sections across the front by latitudinal sections from the ECMWF-IFS data throughout this chapter. This does not induce errors in our analysis because we will not infer horizontal scales from these plots, but use them for depiction only.

On the cyclonic side of the jet core (above the Baltic Sea, Skagerrak and Kattegat), ECMWF-IFS reveals horizontal wind shears in the order of 30 m s^{-1} per 100 km. This is typical for extratropical upper-level frontal zones that have previously been investigated in other case studies (e.g. Shapiro, 1976, 1980; Koch et al., 2005). An extensive review on these phenomena has been given by Keyser and Shapiro (1986). Connected to these fronts are so called *tropopause folds* where stratospheric air folds into the troposphere in a shape that resembles a tongue (please see PV isoline in the right panel of Figure 6.1). In order to detect a tropopause fold, however, we need to look at the definition of the tropopause. After the detection of the stratosphere, the tropopause has been defined by the sharp decrease

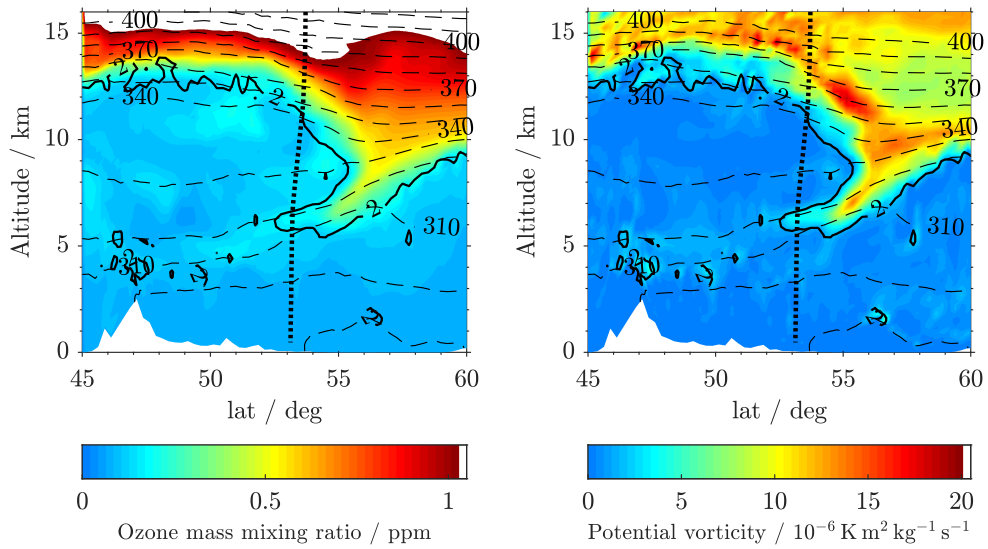

Figure 6.2: Latitudinal sections of the ozone mass mixing ratio (left) and potential vorticity (right) plotted at 11 °E. Both plots show ECMWF-IFS data for 06 August 2016, 16:00 UT. The dotted lines mark the flightpath of the LITOS sonde, dashed lines denote isolines of potential temperature. The solid black lines show the dynamical tropopause at 2 PVU.

in temperature lapse rate (Aßmann, 1902). To this day, a very common definition of the tropopause is "the lowest level at which the lapse rate decreases to 2 °C km^{-1}" together with some auxiliary conditions (WMO, 1957). In our case, it is vital to distinguish tropospheric from stratospheric air masses during an event where the flow is not in thermodynamic equilibrium. This separation can be done by the definition of a *dynamical* tropopause based on potential vorticity P:

$$P = -g\,(\xi_\theta + f)\,\partial\theta/\partial p. \tag{6.1}$$

$(\xi_\theta + f)$ is the absolute vorticity of an air parcel evaluated on constant pressure surfaces, g the Earth's acceleration and $-\partial\theta/\partial p$ is the thermal stability of the background atmosphere (e.g. Shapiro, 1980). This potential vorticity shows a sharp gradient at the extratropical tropopause, thereby enabling us to separate tropospheric and stratospheric air masses (e.g. Holton et al., 1995). This is because, for all diabatic processes, P is a conserved quantity.

In the literature, a variety of PV thresholds are used to define the dynamical tropopause. Some use a level of $P = 2$ PVU (1 PVU $\equiv \frac{10^{-6}\,K\,m^2}{kg\,s}$, e.g. Holton et al., 1995; Kunz et al., 2011), others adopt 1.5 PVU (e.g. Koch et al., 2005) or 1 PVU (Shapiro, 1978). In this chapter, we use a threshold of 2 PVU in order to be consistent with recent publications (c.f. Woiwode et al., 2018).

This tropopause definition is used in the right panel of Figure 6.1, for example. There we see that from the North-East a tongue of stratospheric air is submerged under the jet streak. Further evidence that this submersion took place can be seen in Figure 6.2. We note that the 2 PVU line corresponds reasonably well with a sharp increase in the ozone mass mixing ratio. Therefore, our dynamical definition of the tropopause corresponds adequately

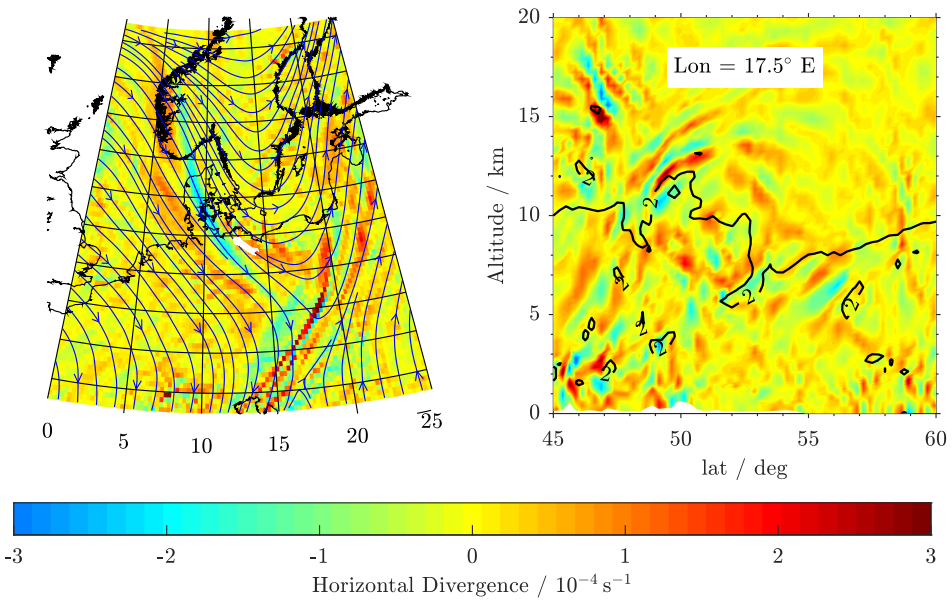

Figure 6.3: Same as Figure 6.1, but showing a map of horizontal divergence of the wind field at $z = 10\,\text{km}$ on the left and a logitudinal Section at 17.5 °E on the right. Please note that in comparison to Figure 6.3 another longitude is chosen for the Section in order to show wave structures over Eastern Europe. For enhanced visibility the colourbar is slightly over saturated.

with the chemical one. This allows us to use the 2 PVU line as a proxy for the chemical tropopause, which is relevant for mixing processes of trace gases.

In the *exit region* of the jet, a strong cyclonic/anticyclonic curvature of the flow is visible. The *exit region* is the area where the jet turns sharply northward above South-Eastern Europe. A schematic picture and further information are, for example, given by Plougonven and Zhang (2014). This region is characterised by enhanced divergence of the horizontal wind field above South-Eastern Europe (c.f. left panel of Figure 6.3). The vertical winds shown in the right panel of that figure suggest the generation of gravity waves in this region. However, as their signatures are located approximately 100 km away from our measurement and no traces of the waves were found on the data, we will not discuss them in further detail.

6.2 In-situ measurements using LITOS and a radiosonde

A comparison between the measurement from our radiosonde on board the LITOS instrument and the ECMWF data is shown in Figure 6.5. Above 9.5 km we use data from the descending radiosonde, because the LITOS measurement has been done on downleg. Below 9.5 km, the upleg data of the radiosonde is used, because we lost radiosonde telemetry in this height on descent. We note, however, that there is hardly any "jump" in the temperature and humidity measurements where both profiles have been merged, even though no smoothing has been applied. In the wind speed measurement, the deviation is less than $2\,\text{m}\,\text{s}^{-1}$. This is expected though, as typical along-front scales of upper-level fronts are

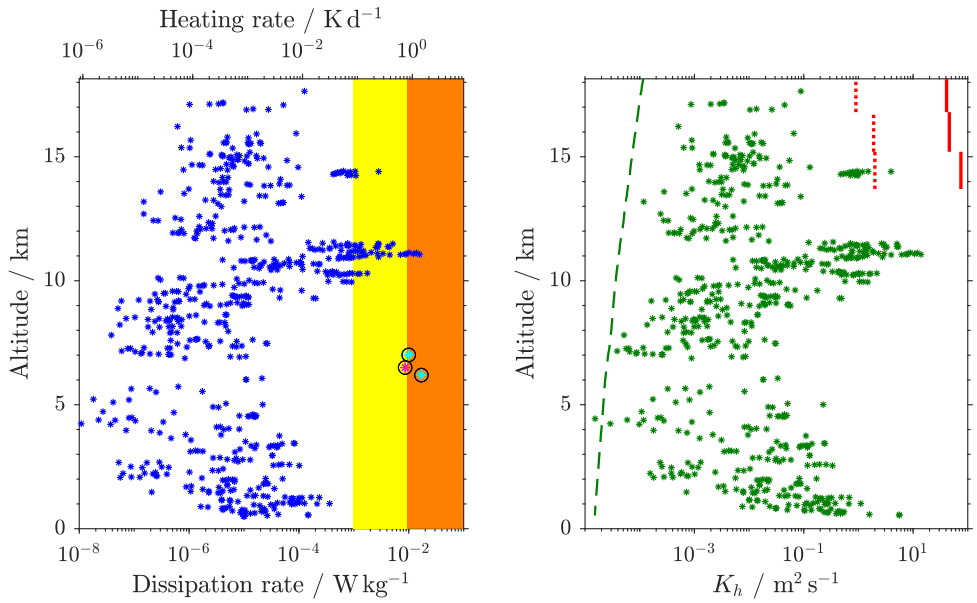

Figure 6.4: Left: Turbulent kinetic energy dissipation rates from LITOS on 06 August 2016 (blue stars). Circled cyan stars denote measurements from Kennedy and Shapiro (1975), the circled magenta star from Reid and Vaughan (2004). Yellow and orange colour-shading marks light to moderate and moderate to severe turbulence intensities according to Sharman et al. (2014), respectively. Right: Turbulent diffusion coeffcient for heat K_h from the same measurement (green stars). The dashed green line marks molecular diffusivity. Solid red lines show mean dissipation rates for turbulence events from Lilly et al. (1974), dashed red lines denote derived mean values over turbulent and non-turbulent situations.

about one order of magnitude larger than the distance of upleg and downleg tracks from the radiosonde (190 km).

In general, the radiosonde data and the ECMWF-IFS agree remarkably well, even though this particular radiosonde was not assimilated in the model. In wind speed, deviations are mostly below 5 m s^{-1}. It is only within the jet that the model underestimates the wind speed by up to 10 m s^{-1}. For temperature, the deviation is generally less than 3 K. At altitudes below 7 km, there is a systematic bias in the IFS to higher temperatures. This, however, may have been caused by smaller scale tropospheric weather patterns, as the radiosonde data in this area are taken from the ascent.

In the altitude range from 6 km to 8 km, we see a reduced temperature lapse rate, reduced humidity and an increased ozone concentration in comparison with the layers below and above. The former two metrics give an independent reference to the stratospheric intrusion that has already been discussed in connection with Figures 6.1; 6.2.

For the computation of the Richardson number, the radiosonde data have been smoothed using a Hann-weighted average of 1000 m (solid line) or 500 m (dotted line), respectively . The two areas with the lowest Richardson numbers are found in the vertical shear zone above the jet core at 11.1 km and in the planetary boundary layer. Using a smoothing length of 500 m, we are sufficiently able to resolve the shear above the jet core resulting in subcritical Richardson numbers. In contrast to the 1000 m smoothing, however, we still

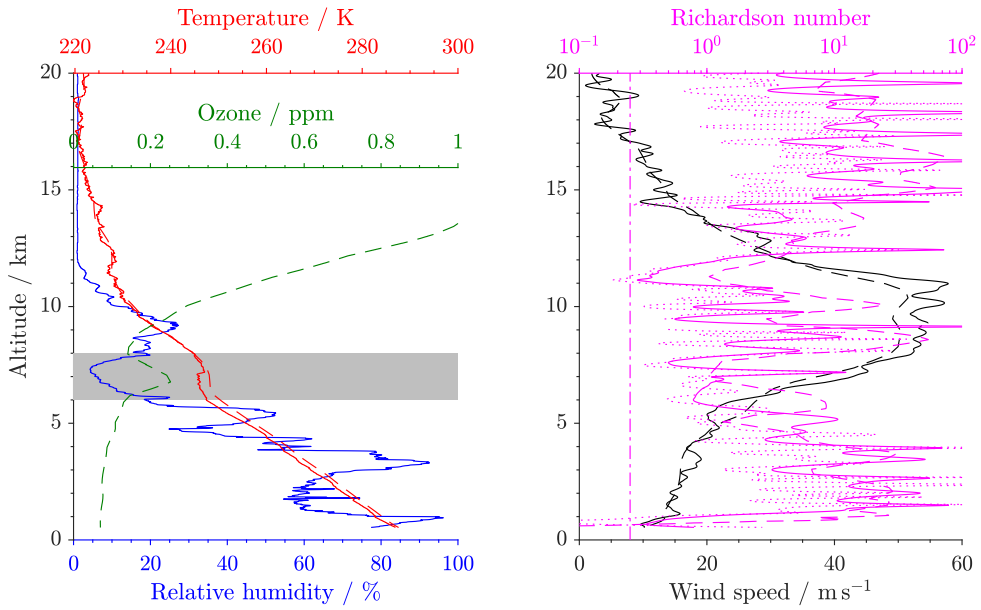

Figure 6.5: Data from the LITOS measurement on 06 August 2016. All solid lines are taken from the radiosonde, dashed lines are interpolated on the downleg radiosonde flight-path from ECMWF-IFS. Left: Temperature (red), and relative humidity (blue) and ozone (green). The grey shaded area marks the height range with intrusion of stratospheric air. Right: wind in black and Richardson number in magenta (solid: radiosonde, 1000 m smoothing; dotted: radiosonde, 500 m smoothing; dashed: ECMWF-IFS). $Ri_{\mathrm{crit}} = 0.25$ is marked by the dash-dotted line.

see an influence of small-scale wave-like features in the wind field. The stronger smoothed data show a roughly similar pattern compared to the unsmoothed IFS data (dashed line). However, we notice that apart from the boundary layer there are two Ri-minima in the IFS-data (above and below the jet core) with equal stability of $Ri = 1.1$. This is in contrast to the radiosonde data, where the stability in the shear zone above the jet core is distinctly lower than below the jet core.

The primary instrument on our payload was LITOS. The profile of kinetic energy dissipation rates depicted in the left panel of Figure 6.4 prominently show a turbulent patch between 9 km and 11.5 km altitude. Peak dissipation rates in this patch are $1.5{\cdot}10^{-2}\,\mathrm{W\,kg^{-1}}$, which correspond to *moderate* turbulence intensities for medium sized aircraft (Sharman et al., 2014). Casually speaking, this means that no more coffee will be served on board, but that there is no danger to the structural integrity of the aircraft, either.

Compared with the few other turbulence measurements related to tropopause folds, we find similar peak dissipation rates: Kennedy and Shapiro (1975) obtain $1.7 \cdot 10^{-2}\,\mathrm{W\,kg^{-1}}$ from in-situ aircraft measurements, while Reid and Vaughan (2004) find $8.6 \cdot 10^{-3}\,\mathrm{W\,kg^{-1}}$ from the spectral width of a radar measurement. Given that the location of the tropopause folds, the measurement methods and even the supposed local turbulence generation mechanisms are different in these cases, the agreement is remarkable. However, the location of the turbulent patch significantly differs between our measurement and reports in the literature (discussed further below). Besides the upper-level front related turbulence patch, we find slightly enhanced dissipation rates in the boundary layer compared to the

free troposphere ($2 \cdot 10^{-4}\,\mathrm{W\,kg^{-1}}$ vs. $2 \cdot 10^{-5}\,\mathrm{W\,kg^{-1}}$) as well as one turbulence patch of *light* intensity at an altitude of 14.5 km (Sharman et al., 2014). However, these turbulence encounters shall not be discussed further in order to keep this chapter focused. Instead, we will investigate the strongest turbulence event of the measurement around 11 km altitude with a special focus on the turbulence-background interaction in the next section.

In the right panel of Figure 6.4, we show turbulent diffusion coefficients K_h calculated according to Lilly et al. (1974):

$$K_h = \frac{\varepsilon}{3\,N^2}. \tag{6.2}$$

The general structure of the altitude profile resembles that of the ε-measurement with some influences from the background static stability, which has been calculated using a 1000 m averaging window. For comparison, we also plotted averaged values measured by Lilly et al. (1974) over flat terrain during the HICAT project. They will be discussed in Section 6.4.

6.3 The role of atmospheric turbulence in the formation of the tropopause fold

As mentioned above, these turbulence investigations were taken during the passage of an upper-level front. Upper level fronts are classified as regions of large horizontal temperature gradients, high static stability N and high absolute vorticity $\xi_\theta + f$ (Keyser and Shapiro, 1986). They occur if baroclinic wave disturbances of the flow converge horizontally, thereby steepening the gradients. Early investigations of these phenomena were made possible by the introduction of the radiosonde in the late 1920s and early 1930s (BJERKNES, 1937). Further understanding of the phenomenon was gathered in the 1950s (e.g. Reed, 1955). As also visible in Figures 6.1 and 6.2, these upper-level fronts are associated with a submersion of stratospheric air (high potential vorticity, high ozone concentration, low humidity) on the cyclonic side of the tropopause jet (e.g. Davies and Rossa, 1998).

As shown in the previous section, we encountered *moderate* turbulence intensities in the lower stratosphere above the jet, but not within the tropopause fold. Shapiro (1976) found that turbulence not only accompanies upper-level fronts due to their strong vertical gradients in wind speed, but that mixing induced by turbulence is of primary importance in the genesis of these fronts. This concept relies on the local generation of potential vorticity (PV) by turbulent mixing. Comparing latitudinal sections of ozone concentration and PV in Figure 6.2, we note enhanced PV values in the lowermost stratosphere close to the dynamical tropopause (between 1.5 PVU and 2 PVU). They are especially pronounced in the shear region around the jet (c.f. Figure 6.1 for wind speeds). The ozone concentration in contrast shows a continuous increase with altitude in the lower stratosphere. This is a first hint that PV conservation is violated in tropopause folds.

Hence we will consider the continuity equation for potential vorticity that is given by (Shapiro, 1976):

$$\frac{dP}{dt} = \frac{d}{dt}\left(\xi_\theta + f\right)\frac{\partial \Theta}{\partial p} \approx \left(\xi_\theta + f\right)\frac{\partial}{\partial p}\left(\frac{d\Theta}{dt}\right). \tag{6.3}$$

This consideration neglects frictional heating by turbulence, as suggested by Shapiro (1976) from a scale analysis. In our case, the maximum frictional heating rate is below $2\,\mathrm{K\,d^{-1}}$.

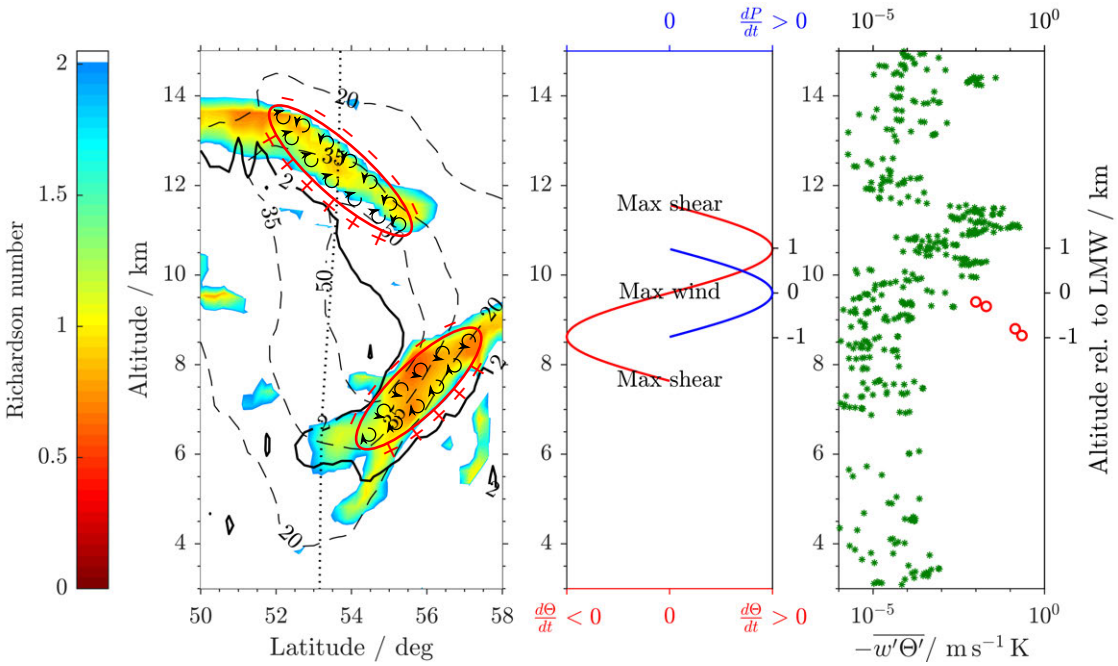

Figure 6.6: Schematic showing the local PV generation by turbulence for the case from 06 August 2016. Left: Colour-coded Richardson numbers from the ECMWF-IFS for 16:00 UT. Wind speed shown by dashed lines, the black line shows the 2 PVU level. Regions where turbulence is expected are marked by red ellipses, together with the sign of $\frac{d\Theta}{dt}$ due to turbulent temperature diffusion. The LITOS flightpath is shown by a dotted line. Middle: Idealised illustration of heat fluxes and diabatic heating rate. Right: vertical eddy flux of potential temperature from the LITOS measurement in green, values from Shapiro (1976) shown in red for comparison.

The heating due to vertical eddy flux of potential temperature on the other hand can be computed from:

$$\frac{d\Theta}{dt} = g\frac{\partial}{\partial p}\left(-\rho\overline{w'\Theta'}\right) \approx -\frac{\partial}{\partial z}\left(\overline{w'\Theta'}\right) \tag{6.4}$$

(Keyser and Shapiro, 1986). The approximation in this formula comes from the assumption that vertical density variations are small compared to vertical heat flux variations. In our case, we retrieve a maximum of $\frac{d\Theta}{dt} = 16\,\mathrm{K\,d^{-1}}$ in the turbulent layer. This is about one order of magnitude larger than the frictional heating term ($\epsilon = 16\,\mathrm{mW\,kg^{-1}}$, turbulent heating rate $\left(\frac{dT}{dt}\right)_{\mathrm{turb}} = 1.4\,\mathrm{K\,d^{-1}}$), which justifies neglecting the latter. The prognostic equation of potential vorticity P can be obtained from Eq. 6.3, according to Keyser and Shapiro (1986):

$$\frac{dP}{dt} \approx (\xi_\theta + f)\,\frac{\partial^2}{\partial p^2}\left(-\rho\overline{w'\Theta'}\right). \tag{6.5}$$

As the high diabatic changes in potential temperature of up to $16\,\mathrm{K\,d^{-1}}$ suggest, we will investigate the local diabatic generation of potential vorticity by turbulent mixing. The general idea of Shapiro's (1976) concept and its application to our measurement from 06

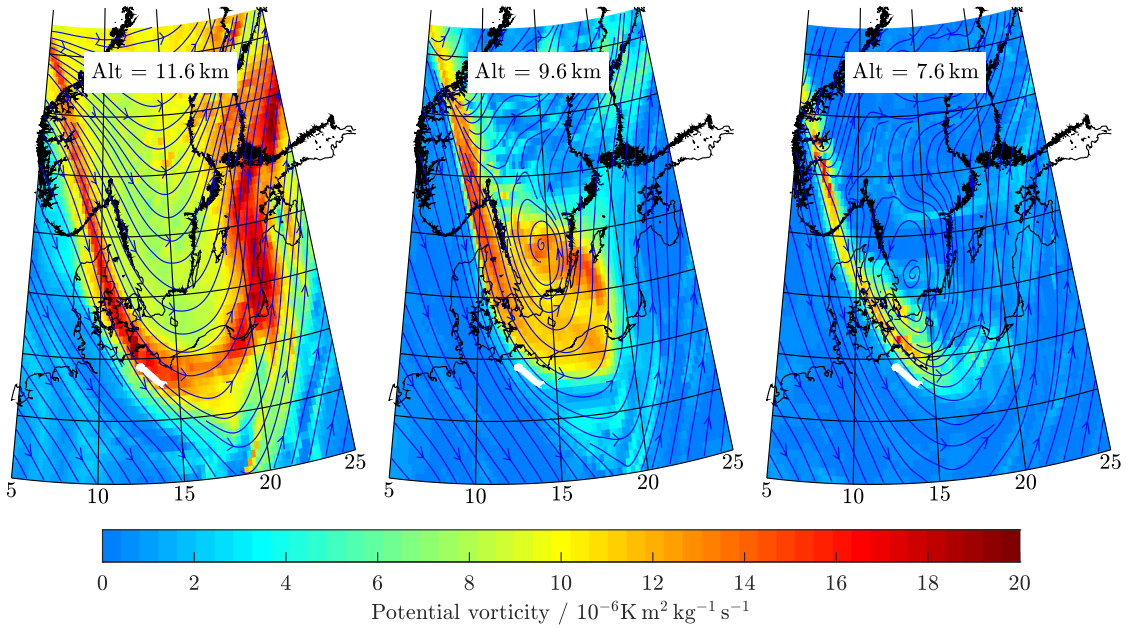

Figure 6.7: Same as Figure 6.1, but for potential vorticity. Shown are the upper shear zone (left), the level of maximum wind (LMW, middle) and the lower shear zone (right).

August 2016 are visualised in Figure 6.6. In the ECMWF-IFS analyses we find two kidney-shaped areas of reduced Richardson numbers, where turbulent mixing leads to a downward (negative) vertical flux of potential temperature. This in turn results in cooling at the top and heating at the bottom of each turbulent layer according to Equation 6.4. This is shown by the schematic $\frac{d\Theta}{dt}$ curve in the middle panel of Figure 6.6. According to Equation 6.5, this results in a generation of potential vorticity at the level of maximum wind (LMW) above the southern Baltic sea that can also be seen in the PV map of the ECMWF-IFS data (middle panel of Figure 6.7). As the absolute vorticity ($\xi_\theta + f$) appears as a factor in Equation 6.5, this production of potential vorticity is limited to the cyclonic side of the jet core. This is the northern side in our case, because the relative vorticity ξ_θ is higher there.

In the right panel of Figure 6.6, we show measured vertical eddy fluxes of potential temperature $\overline{w'\Theta'}$. They are calculated from the kinetic energy dissipation rates according to Lilly et al. (1974). As the viscous dissipation is given by the difference between the buoyant removal and the production of energy, they obtain:

$$\overline{w'\Theta'} = -\frac{\varepsilon\,\Theta}{3\,g}, \tag{6.6}$$

where g is the gravitational constant. For comparison, we also plotted values obtained by Kennedy and Shapiro (1975) during the sounding of a tropopause fold. Their vertical position has been plotted relative to the level of maximum wind in our case study.

We note that in contrast to the expectations by Shapiro (1976) and Keyser and Shapiro (1986), we did not encounter a turbulent patch below the level of maximum wind (LMW). Accordingly, no enhanced eddy heat fluxes were observed in this region. This also contrasts the expectation of turbulence occurrence from Richardson numbers in the ECMWF-IFS fields as shown in the left panel of Figure 6.6. Possible reasons and implications will be discussed in the following section.

According to Shapiro (1976), this enhanced potential vorticity generated at the LMW is transported downward into the troposphere while retaining high static stability. This potential vorticity increase is then transformed into relative vorticity of the mesoscale flow. This can be seen from the continuity equation of potential vorticity. An increase in PV due to turbulent heat flux will increase the right hand side of Eq. 6.3. If the gradient of potential temperature $\partial\Theta/\partial p$ is constant, then this increase will enhance the relative vorticity ξ_Θ. Due to the eastward mean flow in our case, this leads to a submersion of stratospheric air from the north to the south as seen in Figure 6.2. The proposed constancy in static stability is also found in the radiosonde data. In the submersion zone marked by grey colour shading in Figure 6.5, the measured buoyancy frequency is between $2 \cdot 10^{-2}$ Hz and $2.5 \cdot 10^{-2}$ Hz like in the stratosphere, while we find $1.1 \cdot 10^{-2}$ Hz in the free troposphere (full profile not shown here).

In the left and right panel of Figure 6.7, we see that enhanced values of PV not only appear in the LMW, but also in the upper and lower shear zones close to the jet. This is a further hint that stratospheric air can be submerged under the jet, because the similar PV values in all three altitudes suggest that air parcels can be moved adiabatically between these altitudes.

For completeness, we like to mention that there is another mechanism influencing frontogenesis: It is an ageostrophic circulation transverse to the the jet-axis. This transverse flow subsides into the troposphere, thereby enhancing the shear of the flow and the vorticity, which in turn amplifies the subsidence (Keyser and Shapiro, 1986). Therefore, this mechanism creates a positive feedback loop for frontogeneis and the generation of tropopause folds.

6.4 Discussion of our findings and differences to a *standard* tropopause fold

Tropopause folds are regarded as zones where stratospheric air enters the troposphere and vice versa, thereby influencing ozone destruction by chlorofluorocarbons (CFCs, e.g. Shapiro, 1980). On the other hand, in the second half of the 20th century radioactive substances from nuclear tests entered the troposphere from the stratosphere in these regions (e.g. Reiter, 1975). From a more general perspective, tropopause folds are one of the processes that lead to stratosphere-troposphere exchange. This exchange also leads to changes in radiative forcing of the troposphere and lower stratosphere that have an influence on climate change (Holton et al., 1995). Furthermore, upper-level front systems are known to generate intense gravity waves and turbulence, which can be hazardous to air transport (Koch et al., 2005). Even though this field of atmospheric studies is not new, we think that we can make a beneficial contribution to the discussion because our case study showed some significant differences to the classical picture that may have influences on the stratosphere-troposphere exchange.

A report of a tropopause fold that contains advanced two dimensional remote soundings of trace gases is given by Woiwode et al. (2018). Even though they did not measure turbulence directly, they reported two regions of enhanced mixing. They find mixing in the shear zone on the anticyclonic side of the jet core (the Northern side in our case). Furthermore, they find mixing by shear generated turbulence at the lower edge of the tropopause fold. The first mixing region corresponds well to the area where LITOS measured turbulence in our case study. The mixing zone at the lower edge of the intrusion however is non turbulent in

our case (c.f. Figure 6.6).

Generally our measurement through a tropopause fold shows good agreement with ECMWF-IFS in the wind and temperature fields as well as in the altitude of the stratospheric intrusion (Figure 6.5). Our turbulence measurement yields eddy diffusion coefficients that are less than half a magnitude lower than the average values over all turbulence measurements above flat terrain obtained by Lilly et al. (1974) in slightly higher altitudes (c.f. Figure 6.4). This is taken as a first hint that our turbulent patch showed an ordinary eddy diffusion coefficient when compared to a broad database of turbulence measurements. This impression is substantiated when comparing our data more specifically to other measurements from within tropopause folds. The values of Kennedy and Shapiro (1975) as well as Reid and Vaughan (2004) show remarkable consensus with our dissipation rates, differing by less than a factor of two. This justifies that we compare our measurement and the ECMWF-IFS analyses to their findings, even though their studies were done under slightly different conditions such as other latitude.

However, this correspondence has to be treated with some caution because different measurement methods (aircraft and radar analyses) yield different averaging lengths of the retrieval, which can influence the measured dissipation rates due to the strong intermittency of turbulence. Shapiro (1976) provides further examples of *moderate* turbulence being observed by aircraft in the upper shear zone of an upper-level front.

Regarding the turbulence generation mechanism, we expect that in our case shear from the jet in the upper-level front system created turbulence via a Kelvin-Helmholtz instability, because no significant gravity wave activity was found on our measurement data. This is in accordance with other soundings like Kennedy and Shapiro (1975). In contrast however, Koch et al. (2005) found breaking gravity waves to be the main cause for turbulence production in his investigation of an upper-level front with a tropopause fold.

As mentioned above, we also find good resemblance between our measurement and the ECMWF-IFS in terms of the height of the stratospheric intrusion. However, we find a clear difference between our turbulence measurements and what is expected from ECMWF-IFS as well as from the considerations by Shapiro (1976) and Keyser and Shapiro (1986): we only find turbulence in the upper shear zone of the jet, not in the lower one (c.f. Figure 6.4). It is, furthermore, in contrast to the expectation from the occurrence of low Richardson number areas in the ECMWF-IFS (Figure 6.6) and to trace gas observations from Woiwode et al. (2018). This is especially remarkable, as the model shows even slightly lower Ri in the lower shear zone compared to the upper one (Figure 6.5). Therefore, we note that the ECMWF-IFS agrees with the theoretical expectations from Shapiro (1976), whereas our measurement does not. However, our dissipation rates and vertical turbulent potential temperature fluxes of the turbulence patch in the upper shear zone resemble other values in the literature very closely. This makes the fact that we did not find any enhanced dissipation rates in the lower shear zone even more puzzling.

We do not know the reason for these deviations from the classical picture of a tropopause fold. In our opinion, there are two likely explanations for the differences:

No turbulence encounter due to transience:
As there was only one LITOS sonde flown during the particular event, the only data source available to us to consider the time development of the turbulent patches are the ECMWF-IFS data. Figure 6.8 shows latitudinal sections of Ri in the area where the tropopause fold developed. At 04:00 UT, the jet has not reached the area and accordingly, no kidney-shaped pattern of reduced Ri is found. For 10:00 UT, we find $Ri < 1/4$ in the lower shear zone and even further south. Equally, at 16:00 UT (time of LITOS sounding) as well as at 22:00 UT,

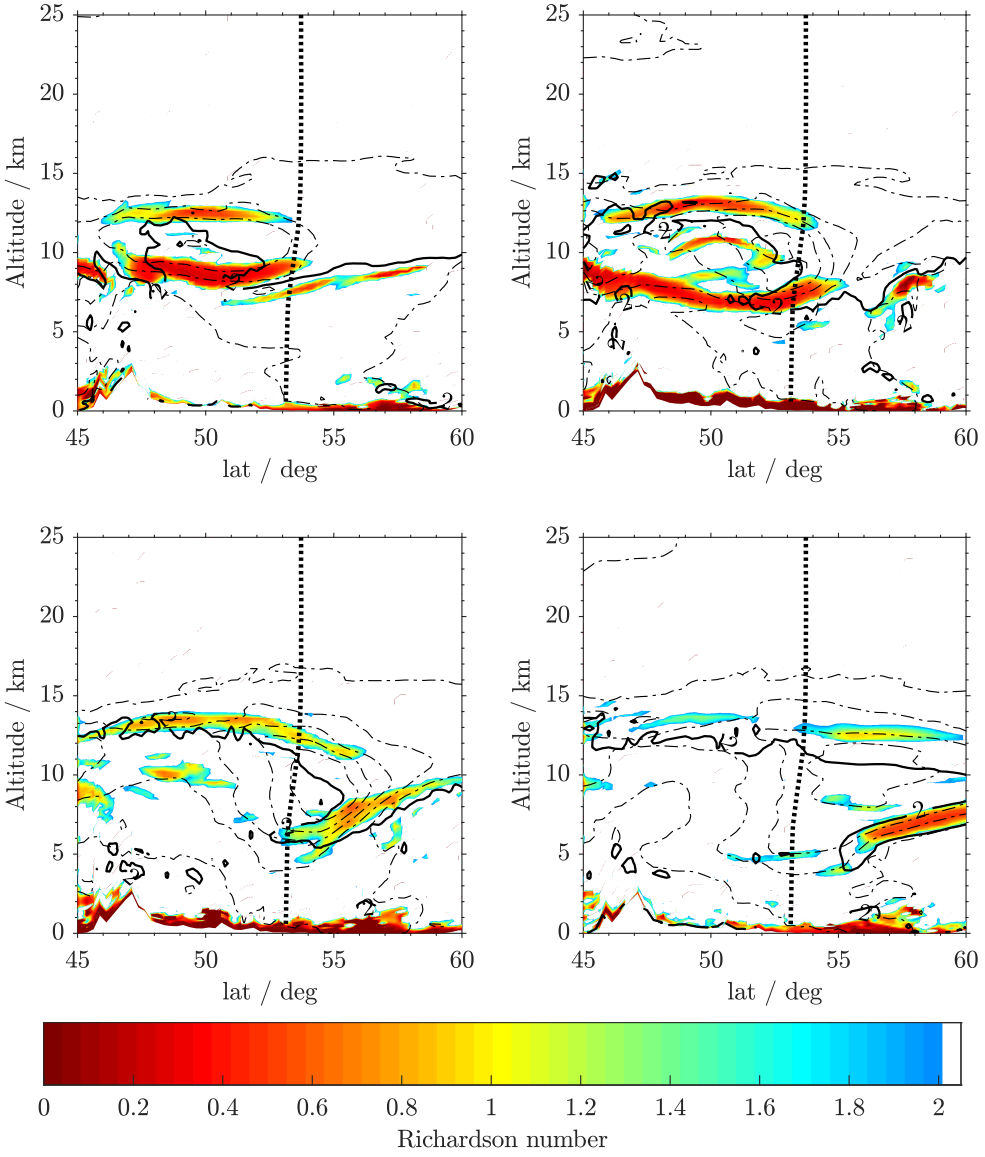

Figure 6.8: Latitudinal section of the Richardson number from ECMWF-IFS on 06 August 2016. Top left: 04:00 UT. Top right: 10:00 UT. Bottom left: 16:00 UT (time of the LITOS measurement). Bottom right: 22:00 UT. The dashed-dotted lines denote the windspeed in $\mathrm{m\,s^{-1}}$, the solid black line marks a potential vorticity of 2 PVU and the dotted line shows the flightpath of the LITOS sonde.

Ri in the lower shear zone is lower than in the upper one. However, *Ri* in the lower shear zone is lower at 10:00 UT and 22:00 UT compared to the time of the launch. Accordingly, we cannot rule out the possibility that the lower shear zone was turbulent before or after the measurement. This would yield two mixing regions as found by Woiwode et al. (2018). However, this remains speculative, as we would also expect to find turbulence in the lower shear zone at 16:00 UT, given that it occurs in the upper one.

Turbulence occurrence not as regular as expected:
The mechanisms of turbulence fostering the development of upper-level frontal zones given by Shapiro (1976) have been affirmed several times in the literature (Shapiro, 1978; Gidel and Shapiro, 1979; Shapiro, 1980; Keyser and Shapiro, 1986; Koch et al., 2005). However, there are other explanations like for example a PV-based approach to upper-level frontogenesis based on the mesoscale flow (Davies and Rossa, 1998). Furthermore, the above mentioned transverse ageostrophic circulation may have considerably contributed to the generation of this tropopause fold (Keyser and Shapiro, 1986). Accordingly, it may be that tropopause folds are not only generated under the very turbulence conditions described by Shapiro (1976). This, however, might have significant influence on their effect on stratosphere-troposphere exchange processes. If there is no turbulence present in the zone of the stratospheric intrusion, stratospheric trace gases may not necessarily be deployed in the troposphere. This is because even though the stratospheric air is transported into tropospheric altitudes, it will need turbulence to be mixed with tropospheric air (Reid and Vaughan, 2004).

In the near future, we plan to further investigate this questions with a series of LITOS launches into an upper-level front. We thereby hope to clarify whether transient effects led to the particularities of the sounding on 06 August 2016, or whether indeed some tropopause folds create less mixing than previously thought in the literature. We are currently waiting for the occurrence of an upper level front to do another single LITOS sounding (October 2019). We are excited to see whether the *abnormal* turbulence distribution of the sounding from 06 August 2016 will occur again.

7 Summary and outlook

Atmospheric turbulence is a condition of the atmospheric flow that has a significant impact on nature as well as on human activities. Momentum deposition by breaking gravity waves, along with the subsequent production of turbulence, controls middle-atmospheric dynamics. Turbulent mixing is important for stratosphere-troposphere exchange of trace gases and turbulence poses significant risks to aviation. Aside from this general comprehension, I obtained the following answers on the questions presented in the introduction:

Q 1: Which theoretical models, measurement concepts and hardware solutions are suitable for atmospheric turbulence measurements?

We retrieve turbulent energy dissipation rates with LITOS using the *inner scale method*. This method depends on one empirical constant only, it avoids a complicated calibration and circumvents influences from internal balloon oscillations. Furthermore we were able to show that measurements using this method do not violate *Taylor's frozen field hypothesis*. However, this retrieval procedure requires a high signal to noise ratio for our measurement. Therefore, in the course of this thesis we have taken steps that reduced the noise of our electronics by more than 1.5 orders of magnitude using a specially designed anti-aliasing filter. Dissipation rates are retrieved by fitting a spectral turbulence model and evaluating the fit quality. These criteria and other parts of the retrieval software have been refined and adjusted as part of this work, while a precursor solution had been created by my predecessors. The same is true for most of the hardware.

As it turned out to be necessary for successful and safe balloon operations, we developed real-time capability for our flightpath prediction tool LIFF and adjusted it to produce all the necessary outputs for descent measurements using two balloons.

For the first time, we were able to do an in-flight comparison with another balloon-borne turbulence instrument in the course of this work. The instrument is called HYFLITS and measures in the inertial subrange. Generally, we found a reasonably good correlation between both measurements ($r = 0.71$) with lower altitudes showing better agreement. On average, LITOS measures higher dissipation rates than HYFLITS in strong turbulence and lower dissipation rates in weak turbulence. This leads us to the conclusion that on the LITOS instrument an attenuation of high frequencies in the measured spectrum possibly causes an underestimation of low dissipation rates under weakly turbulent conditions. Furthermore, the HYFLITS calibration could potentially be improved in order to reduce the overall bias of $\epsilon_{\mathrm{LITOS}} > \epsilon_{\mathrm{HYFLITS}}$.

From our point of view, valuable future tasks concerning this question include calibrated CTA measurements combining the *inner scale* with the *inertial subrange* method, a further simplification of the payload structure and the experimental investigation of turbulent

temperature fluctuations.

Q 2: Which quality control procedures are needed for reliable measurements?

According to our results, the most important quality control measure for turbulence soundings on ascending balloons is the avoidance of wake effects. For a standard radiosonde, we find an average probability for encountering the balloon's wake of $P_{\text{wake}} = 28\,\%$, while for an exemplary LITOS sounding $P_{\text{wake}} = 5.6\,\%$ was obtained. In case of the LITOS sounding this leads to only 27 % of all altitude bins being certainly wake free ($P_{\text{wake}} < 5\,\%$). In other words, on about two thirds of all altitude bins there is a potential for false turbulence detections. Furthermore, we noted that the wake from smaller objects upstream of the sensors shows very high dissipation rates ($100\,\text{mW}\,\text{kg}^{-1}$ to $1000\,\text{mW}\,\text{kg}^{-1}$), while the wake from the balloon shows lower dissipation rates between $0.01\,\text{mW}\,\text{kg}^{-1}$ and $10\,\text{mW}\,\text{kg}^{-1}$ (depending on the payload-balloon distance). However, the wake from smaller objects can be detected from its spectral shape, while the wake from the balloon cannot. Solving these issues has made this thesis the first one in the LITOS context where geophysical effects and instrumental influences can be separated. This has led to a new concept, namely measuring on descending balloons. Thereby wake effects are comletely avoided on all LITOS measurements since August 2016.

The second most important finding on that question concerns the CTA measurement. We found from DSMC simulations that from 100 hPa to 3 hPa the CTA signal is reduced by almost three orders of magnitude with half of the reduction being caused by flow rarefication. This is likely to cause an attenuation of the spectrum at high frequencies, having particular impact on the *inner scale method*. In order to avoid influences on our measurements, we refrain from retrieving energy dissipation rates for $Kn > 0.1$ ($z \gtrsim 17.5\,\text{km}$) until a full error handling of the LITOS data has been implemented. This will allow for a more precise discrimination of altitude and dissipation rate areas that are affected by flow rarefication.

Third, we found from our own data as well as from a literature survey that self-induced balloon motions influence horizontal and vertical wind retrievals on vertical scales down to 50 m. Furthermore, we have discussed internal balloon oscillations, which had hardly been noticed in the literature before. From our data we have seen that they influence scales between 5 m and 20 m, thereby possibly inducing errors on turbulence measurements from the large scale part of the *inertial subrange method*. This, however, does not influence our measurements using the *inner scale method*.

In the future, we plan to develop a full error analysis for the LITOS measurement that will include further clarification on the performance of CTAs in rarefied flows.

Q 3: Which results have been obtained with the revised LITOS instrument?

So far, only a small amount of studies has been published that directly relate energy dissipation rate measurements to gravity wave dissipation and shear instabilities of the background flow. Here, three different cases have been evaluated. In our case study on mountain wave breaking we identified wave attenuation with subsequent turbulence generation in a stratospheric layer of reduced wind speed extending over 2.4 km. We were able to show that the *valve layer* concept of Kruse et al. (2016) not only holds for wind minima

of 10 km to 15 km thickness caused by larger scale geophysical flows, but can be extended to *shallow valve layers*. In this case study, gravity waves were investigated using wavelet and hodograph analyses from radiosonde data aided by numerical weather prediction using WRF. The connection between gravity wave attenuation and turbulence generation was suggested by idealised modelling with EULAG.

During our measurement from 14 November 2018, we encountered a Kelvin-Helmholtz instability with comparatively low dissipation rates below 1 mW kg^{-1}. Like the other measurements, it suggests the occurrence of turbulence under flow conditions with Richardson numbers even slightly larger than 0.25. Furthermore, they highlight the influence of the averaging kernel for radiosonde data smoothing on the absolute value of Ri.

In our observational study on the role of turbulence in the generation of a tropopause fold we were able to provide a rare turbulence profile in such a meteorological situation. We have evaluated the passage of LITOS through the fold using radiosonde and ECMWF-IFS data. Remarkably, our peak dissipation rate in the upper shear zone of the jet differs by less than a factor of two from other soundings under similar conditions. Likewise, turbulent heat fluxes and diabatic temperature changes agree very well. However, in contrast to the model from Shapiro (1976) and in contrast to the ECMWF-IFS we did not find turbulence in the stratospheric intrusion. This could be due to the transience of turbulence generation. If, however, this is statistically confirmed by further measurements, it would mean that the influence of tropopause folds on mixing across the tropopause is smaller than expected. Here, turbulence measurements with instruments like LITOS can significantly contribute to the global understanding of stratosphere-troposphere exchange processes.

Concerning this question a series of soundings under certain meteorological conditions such as in upper-level fronts seems a worthwhile future task. Furthermore, regular soundings may be achieved, possibly in combination with the HYFLITS instrument.

The results summarised here contribute to our awareness of the role of turbulence in geophysical flows. Furthermore, they improve our ability to understand and circumvent possible distortions of turbulence measurements that are inherent to balloon soundings. However, as suggested in the quotation below, the progress made in this thesis can hardly be more than a small step in the understanding of turbulence in the Earth's atmosphere, given the amount of open questions.

> There is a physical problem that is common to many fields, that is very old, and that has not been solved. It is not the problem of finding new fundamental particles, but something left over from a long time ago over a hundred years. Nobody in physics has really been able to analyze it mathematically satisfactorily in spite of its importance to the sister sciences. It is the analysis of circulating or turbulent fluids.
>
> Richard P. Feynman (1989)

Bibliography

Achatz, U.: Gravity-wave breaking: Linear and primary nonlinear dynamics, Advances in Space Research, 40, 719 – 733, doi:https://doi.org/10.1016/j.asr.2007.03.078, URL http://www.sciencedirect.com/science/article/pii/S027311770700316X, 2007.

Achenbach, E.: Experiments on the flow past spheres at very high Reynolds numbers, Journal of Fluid Mechanics, 54, 565–575, 1972.

Achenbach, E.: The effects of surface roughness and tunnel blockage on the flow past spheres, Journal of Fluid Mechanics, 65, 113 125, doi:10.1017/S0022112074001285, 1974.

Aßmann, R.: Über die Existenz eines wärmeren Luftstromes in der Höhe von 10 bis 15 km, Sitzungsbericht der Königlich-Preußischen Akademie der Wissenschaften zu Berlin, 24, 495–504, 1902.

Attivissimo, F., Savino, M., and Trotta, A.: A study on nonlinear averagings to perform the characterization of power spectral density estimation algorithms, IEEE Transactions on Instrumentation and Measurement, 49, 1036–1042, 2000.

Azouit, M. and Vernin, J.: Optical Turbulence Profiling with Balloons Relevant to Astronomy and Atmospheric Physics, Publications of the Astronomical Society of the Pacific, 117, 536–543, URL http://stacks.iop.org/1538-3873/117/i=831/a=536, 2005.

Bailey, S. C. C., Kunkel, G. J., Hultmark, M., Vallikivi, M., Hill, J. P., Meyer, K. A., Tsay, C., Aarnold, C. B., and Smits, A. J.: Turbulence measurements using a nanoscale thermal anemometry probe, Journal of Fluid Mechanics, 663, 160 179, doi:10.1017/S0022112010003447, 2010.

Barat, J.: Initial Results from the Use of Ionic Anemometers Under Stratospheric Balloons: Application to the High-Resolution Analysis of Stratospheric Motions, Journal of Applied Meteorology, 21, 1489–1496, doi:10.1175/1520-0450(1982)021⟨1489:IRFTUO⟩2.0.CO;2, 1982.

Barat, J. and Bertin, F.: Simultaneous Measurements of Temperature and Velocity Fluctuations Within Clear Air Turbulence Layers. Analysis of the Estimate of Dissipation Rate by Remote Sensing Techniques, Journal of the Atmospheric Sciences, 41, 1613–1619, doi:10.1175/1520-0469(1984)041⟨1613:SMOTAV⟩2.0.CO;2, 1984.

Barat, J. and Genie, J. C.: A New Tool for the Three-Dimensional Sounding of the Atmosphere: The Helisonde, Journal of Applied Meteorology, 21, 1497–1505, doi:10.1175/1520-0450(1982)021⟨1497:ANTFTT⟩2.0.CO;2, URL https://doi.org/10.1175/1520-0450(1982)021<1497:ANTFTT>2.0.CO;2, 1982.

Barat, J., Cot, C., and Sidi, C.: On the Measurement of the Turbulence Dissipation Rate from Rising Balloons, Journal of Atmospheric and Oceanic Technology, 1, 270–275, doi:10.1175/1520-0426(1984)001⟨0270:OTMOTT⟩2.0.CO;2, 1984.

Becker, E.: Energietransformationen in der Atmosphäre, junge DPG, Bremen, 16 June 2014.

Becker, E.: Dynamical Control of the Middle Atmosphere, Space Science Reviews, 168, 283–314, doi:10.1007/s11214-011-9841-5, URL https://doi.org/10.1007/s11214-011-9841-5, 2012.

Bird, G. A.: Approach to translational equilibrium in a rigid sphere gas, Physics of fluids, 6, 1518–1519, doi:10.1063/1.1710976, 1963.

Bird, G. A.: Molecular gas dynamics and the direct simulation of gas flows, Clarendon Press Oxford, reprinted, 2003.

BJERKNES, J.: Investigations of selected european cyclones by means of serial ascents, Geofysiske Publikasjoner, 12, URL https://ci.nii.ac.jp/naid/10009665785/en/, 1937.

Bönisch, H., Engel, A., Birner, T., Hoor, P., Tarasick, D., and Ray, E.: On the structural changes in the Brewer-Dobson circulation after 2000, Atmospheric Chemistry and Physics, 11, 3937–3948, doi:10.5194/acp-11-3937-2011, URL http://www.atmos-chem-phys.net/11/3937/2011/, 2011.

Booker, J. R. and Bretherton, F. P.: The critical layer for internal gravity waves in a shear flow, Journal of Fluid Mechanics, 27, 513 539, doi:10.1017/S0022112067000515, 1967.

Bouttier, F. and Kelly, G.: Observing-system experiments in the ECMWF 4D-Var data assimilation system, Quarterly Journal of the Royal Meteorological Society, 127, 1469–1488, doi:10.1002/qj.49712757419, 2001.

Bramberger, M., Dörnbrack, A., Bossert, K., Ehard, B., Fritts, D. C., Kaifler, B., Mallaun, C., Orr, A., Pautet, P., Rapp, M., et al.: Does Strong Tropospheric Forcing Cause Large-Amplitude Mesospheric Gravity Waves? A DEEPWAVE Case Study, Journal of Geophysical Research: Atmospheres, 122, 2017.

Bramberger, M., Dörnbrack, A., Wilms, H., Gemsa, S., Raynor, K., and Sharman, R.: Vertically Propagating Mountain WavesA Hazard for High-Flying Aircraft?, Journal of Applied Meteorology and Climatology, 57, 1957–1975, doi:10.1175/JAMC-D-17-0340.1, URL https://doi.org/10.1175/JAMC-D-17-0340.1, 2018.

Brewer, A.: Evidence for a World Circulation Provided by the Measurements of Helium and Water Vapour Distribution in the Stratosphere, Quarterly Journal of the Royal Meteorological Society, 75, 351–363, 1949.

Butchart, N.: The Brewer-Dobson circulation, Reviews of Geophysics, 52, 157–184, doi:10.1002/2013RG000448, URL https://agupubs.onlinelibrary.wiley.com/doi/abs/10.1002/2013RG000448, 2014.

Bölöni, G., Ribstein, B., Muraschko, J., Sgoff, C., Wei, J., and Achatz, U.: The Interaction between Atmospheric Gravity Waves and Large-Scale Flows: An Efficient Description beyond the Nonacceleration Paradigm, Journal of the Atmospheric Sciences, 73, 4833–4852, doi:10.1175/JAS-D-16-0069.1, URL https://doi.org/10.1175/JAS-D-16-0069.1, 2016.

Chen, F. and Dudhia, J.: Coupling an Advanced Land Surface–Hydrology Model with the Penn State-NCAR MM5 Modeling System. Part I: Model Implementation and Sensitivity, Mon. Wea. Rev., 129, 569–585, doi:10.1175/1520-0493(2001)129⟨0569:CAALSH⟩2.0.CO;2, 2001.

Cho, J. Y. N., Newell, R. E., Anderson, B. E., Barrick, J. D. W., and Thornhill, K. L.: Characterizations of tropospheric turbulence and stability layers from aircraft observations, Journal of Geophysical Research: Atmospheres, 108, doi:10.1029/2002JD002820, URL https://agupubs.onlinelibrary.wiley.com/doi/abs/10.1029/2002JD002820, 2003.

Chou, M. D. and Suarez, M. J.: An efficient thermal infrared radiation parameterization for use in general circulation models., NASA Tech. Memo., 104606, 85pp., 1994.

Clayson, C. A. and Kantha, L.: On Turbulence and Mixing in the Free Atmosphere Inferred from High-Resolution Soundings, Journal of Atmospheric and Oceanic Technology, 25, 833–852, doi:10.1175/2007JTECHA992.1, 2008.

Colin, S.: Rarefaction and Compressibility Effects on Steady or Transient Gas Flows in Microchannels, vol. ASME 2nd International Conference on Microchannels and Minichannels of *International Conference on Nanochannels, Microchannels, and Minichannels*, pp. 13–24, doi:10.1115/ICMM2004-2316, URL https://doi.org/10.1115/ICMM2004-2316, 2004.

Constantinescu, G. and Squires, K.: Numerical investigations of flow over a sphere in the subcritical and supercritical regimes, Physics of Fluids, 16, 1449–1466, doi:10.1063/1.1688325, 2004.

Coulman, C. E., Vernin, J., and Fuchs, A.: Optical seeing—mechanism of formation of thin turbulent laminae in the atmosphere, Appl. Opt., 34, 5461–5474, doi:10.1364/AO.34.005461, URL http://ao.osa.org/abstract.cfm?URI=ao-34-24-5461, 1995.

Davies, H. C. and Rossa, A. M.: PV Frontogenesis and Upper-Tropospheric Fronts, Monthly Weather Review, 126, 1528–1539, doi:10.1175/1520-0493(1998)126⟨1528:PFAUTF⟩2.0.CO;2, URL https://doi.org/10.1175/1520-0493(1998)126<1528:PFAUTF>2.0.CO;2, 1998.

Dietmüller, S., Garny, H., Plöger, F., Jöckel, P., and Cai, D.: Effects of mixing on resolved and unresolved scales on stratospheric age of air, Atmospheric Chemistry and Physics, 17, 7703–7719, doi:10.5194/acp-17-7703-2017, URL https://www.atmos-chem-phys.net/17/7703/2017/, 2017.

Dobson, G. M. B. and Massey, H. S. W.: Origin and distribution of the polyatomic molecules in the atmosphere, Proceedings of the Royal Society of London. Series A. Mathematical and Physical Sciences, 236, 187–193, doi:10.1098/rspa.1956.0127, URL https://royalsocietypublishing.org/doi/abs/10.1098/rspa.1956.0127, 1956.

Dommermuth, D. G., Rottman, J. W., Innis, G. E., and Novikov, E. A.: Numerical simulation of the wake of a towed sphere in a weakly stratified fluid, Journal of Fluid Mechanics, 473, 83 101, doi:10.1017/S0022112002002276, 2002.

Dörnbrack, A., Gisinger, S., Kaifler, N., Portele, T. C., Bramberger, M., Rapp, M., Gerding, M., Söder, J., Žagar, N., and Jelić, D.: Gravity waves excited during a minor sudden stratospheric warming, Atmospheric Chemistry and Physics, 18, 12 915–12 931, doi:10.5194/acp-18-12915-2018, URL https://www.atmos-chem-phys.net/18/12915/2018/, 2018.

Dutta, G., Ajay Kumar, M. C., Vinay Kumar, P., Venkat Ratnam, M., Chandrashekar, M., Shibagaki, Y., Salauddin, M., and Basha, H. A.: Characteristics of high-frequency gravity waves generated by tropical deep convection: Case studies, Journal of Geophysical Research: Atmospheres, 114, doi:10.1029/2008JD011332, URL https://agupubs.onlinelibrary.wiley.com/doi/abs/10.1029/2008JD011332, 2009.

ECMWF: IFS Documentation CY45R1, URL https://www.ecmwf.int/en/forecasts/documentation-and-support/changes-ecmwf-model/ifs-documentation, accessed: 04/06/2019, 2019.

Fan, J. and Shen, C.: Statistical Simulation of Low-Speed Rarefied Gas Flows, Journal of Computational Physics, 167, 393 – 412, doi:https://doi.org/10.1006/jcph.2000.6681, URL http://www.sciencedirect.com/science/article/pii/S0021999100966816, 2001.

Feynman, R. P.: The Feynman lectures on physics, Addison-Wesley, Redwood City, Calif. [u.a.], commemorative issue edn., 1989.

Fleming, E. L., Chandra, S., Barnett, J., and Corney, M.: Zonal mean temperature, pressure, zonal wind and geopotential height as functions of latitude, Advances in Space Research, 10, 11 – 59, doi:https://doi.org/10.1016/0273-1177(90)90386-E, URL http://www.sciencedirect.com/science/article/pii/027311779090386E, 1990.

Frehlich, R., Meillier, Y., Jensen, M. L., and Balsley, B.: Turbulence Measurements with the CIRES Tethered Lifting System during CASES-99: Calibration and Spectral Analysis of Temperature and Velocity, Journal of the Atmospheric Sciences, 60, 2487–2495, doi:10.1175/1520-0469(2003)060⟨2487:TMWTCT⟩2.0.CO;2, URL https://doi.org/10.1175/1520-0469(2003)060<2487:TMWTCT>2.0.CO;2, 2003.

Fritts, D. and Alexander, J.: Gravity wave dynamics and effects in the middle atmosphere, Reviews of Geophysics, 41, 2003.

Fritts, D., Bizon, C., Werne, J., and Meyer, C.: Layering accompanying turbulence generation due to shear instability and gravity-wave breaking, Journal of Geophysical Research: Atmospheres (1984–2012), 108, 2003.

Fritts, D. C., Smith, R. B., Taylor, M. J., Doyle, J. D., Eckermann, S. D., Dörnbrack, A., Rapp, M., Williams, B. P., Pautet, P.-D., Bossert, K., Criddle, N. R., Reynolds, C. A., Reinecke, P. A., Uddstrom, M., Revell, M. J., Turner, R., Kaifler, B., Wagner, J. S., Mixa, T., Kruse, C. G., Nugent, A. D., Watson, C. D., Gisinger, S., Smith, S. M., Lieberman, R. S., Laughman, B., Moore, J. J., Brown, W. O., Haggerty, J. A., Rockwell, A., Stossmeister, G. J., Williams, S. F., Hernandez, G., Murphy, D. J., Klekociuk, A. R., Reid, I. M., and Ma, J.: The Deep Propagating Gravity Wave Experiment (DEEPWAVE): An Airborne and Ground-Based Exploration of Gravity Wave Propagation and Effects from Their Sources throughout the Lower and Middle Atmosphere, Bulletin of the

American Meteorological Society, 97, 425–453, doi:10.1175/BAMS-D-14-00269.1, URL https://doi.org/10.1175/BAMS-D-14-00269.1, 2016.

Gaffen, D. J.: Temporal inhomogeneities in radiosonde temperature records, Journal of Geophysical Research: Atmospheres, 99, 3667–3676, doi:10.1029/93JD03179, 1994.

Gai, S. L.: Calibration and use of hot wire probes for steady state measurements in low density flows, Wärme - und Stoffübertragung, 10, 107–115, doi:10.1007/BF01682703, URL https://doi.org/10.1007/BF01682703, 1977.

Gavrilov, N. M., Luce, H., Crochet, M., Dalaudier, F., and Fukao, S.: Turbulence parameter estimations from high-resolution balloon temperature measurements of the MUTSI-2000 campaign, Annales Geophysicae, 23, 2401–2413, URL https://hal.archives-ouvertes.fr/hal-00329429, 2005.

Gibson, CH Chen, C. and Lin, S.: Measurements of turbulent velocity and temperature fluctuations in the wake of a sphere., AIAA Journal, 6, 642–649, doi:10.2514/3.4557, 1968.

Gidel, L. T. and Shapiro, M. A.: The Role of Clear Air Turbulence in the Production of Potential vorticity in the Vicinity of Upper Tropospheric jet Stream-Frontal Systems, Journal of the Atmospheric Sciences, 36, 2125–2138, doi:10.1175/1520-0469(1979)036⟨2125:TROCAT⟩2.0.CO;2, URL https://doi.org/10.1175/1520-0469(1979)036<2125:TROCAT>2.0.CO;2, 1979.

Gill, G. C.: A Fast Response Anemometer for Micrometeorological Investigations, Bulletin of the American Meteorological Society, 35, 69–75, doi:10.1175/1520-0477-35.2.69, URL https://doi.org/10.1175/1520-0477-35.2.69, 1954.

Haack, A., Gerding, M., and Lübken, F.-J.: Characteristics of stratospheric turbulent layers measured by LITOS and their relation to the Richardson number, Journal of Geophysical Research: Atmospheres, 119, 10,605–10,618, doi:10.1002/2013JD021008, 2014.

Heisenberg, W.: Zur statistischen Theorie der Turbulenz, Zeitschrift für Physik, 124, 628–657, 1948.

Henderson, R. D.: Details of the drag curve near the onset of vortex shedding, Physics of Fluids, 7, 2102–2104, doi:10.1063/1.868459, 1995.

Holton, J. R. and Alexander, M. J.: The role of waves in the transport circulation of the middle atmosphere, Washington DC American Geophysical Union Geophysical Monograph Series, 123, 21–35, doi:10.1029/GM123p0021, 2000.

Holton, J. R., Haynes, P. H., McIntyre, M. E., Douglass, A. R., Rood, R. B., and Pfister, L.: Stratosphere-troposphere exchange, Reviews of Geophysics, 33, 403–439, doi:10.1029/95RG02097, URL https://agupubs.onlinelibrary.wiley.com/doi/abs/10.1029/95RG02097, 1995.

Hong, S.-Y. and Lim, J.-O. J.: The WRF single-moment 6-class microphysics scheme (WSM6), J. Korean Meteor. Soc., 42, 129–151, 2006.

Hugo, R. J., Nowlin, S. R., Eaton, F. D., Bishop, K. P., and McCrae, K. A.: Hot-wire calibration in a nonisothermal incompressible pressure variant flow, Airbborne Laser Advanced Technology II, 3706, doi:10.1117/12.356955, URL https://doi.org/10.1117/12.356955, 1999.

Isom, L. W.: Fast Rising Sounding Balloon, URL https://patents.google.com/patent/US2492800A/en, US Patent 2,492,800, 1949.

Jang, Y. I. and Lee, S. J.: PIV analysis of near-wake behind a sphere at a subcritical Reynolds number, Experiments in Fluids, 44, 905–914, doi:10.1007/s00348-007-0448-2, URL https://doi.org/10.1007/s00348-007-0448-2, 2008.

Jodlbauer, K.: Das Temperatur- und Geschwindigkeitsfeld um ein geheiztes Rohr bei freier Konvektion, Forschung auf dem Gebiet des Ingenieurwesens A, 4, 157–172, doi:10.1007/BF02714582, URL https://doi.org/10.1007/BF02714582, 1933.

Jørgensen, F. E.: How to measure turbulence with hot-wire anemometers, NCAR technical note, Dantec Dynamics A/S, Tonsbakken, Skovlunde, Denmark, URL http://www2.mmm.ucar.edu/wrf/users/docs/arw_v3.pdf, 2005.

Jumper, G. and Murphy, E.: Effect of balloon wake on thermosonde results, in: 32nd AIAA Plasmadynamics and Lasers Conference, p. 2796, doi:10.2514/6.2001-2796, 2001.

Kadoya, K., Matsunaga, N., and Nagashima, A.: Viscosity and Thermal Conductivity of Dry Air in the Gaseous Phase, Journal of Physical and Chemical Reference Data, 14, 947–970, doi:10.1063/1.555744, URL https://doi.org/10.1063/1.555744, 1985.

Kennedy, P. J. and Shapiro, M. A.: The Energy Budget in a Clear Air Turbulence Zone as Observed by Aircraft, Monthly Weather Review, 103, 650–654, doi:10.1175/1520-0493(1975)103⟨0650:TEBIAC⟩2.0.CO;2, URL https://doi.org/10.1175/1520-0493(1975)103<0650:TEBIAC>2.0.CO;2, 1975.

Keyser, D. and Shapiro, M. A.: A Review of the Structure and Dynamics of Upper-Level Frontal Zones, Monthly Weather Review, 114, 452–499, doi:10.1175/1520-0493(1986)114⟨0452:AROTSA⟩2.0.CO;2, URL https://doi.org/10.1175/1520-0493(1986)114<0452:AROTSA>2.0.CO;2, 1986.

King, L.: On the Convection of Heat from Small Cylinders in a Stream of Fluid: Determination of the Convection Constants of Small Platinum Wires, with Applications to Hot-Wire Anemometry, Proceedings of the Royal Society of London. Series A, 90, 563–570, doi:10.1098/rspa.1914.0089, URL http://rspa.royalsocietypublishing.org/content/90/622/563.short, 1914.

Klemp, J. B., Dudhia, J., and Hassiotis, A. D.: An Upper Gravity-Wave Absorbing Layer for NWP Applications, Mon. Wea. Rev., 136, 3987–4004, doi:10.1175/2008MWR2596.1, 2008.

Klostermeyer, J. and Rüster, R.: Radar observation and model computation of a jet stream-generated Kelvin-Helmholtz instability, Journal of Geophysical Research: Oceans, 85, 2841–2846, doi:10.1029/JC085iC05p02841, URL https://agupubs.onlinelibrary.wiley.com/doi/abs/10.1029/JC085iC05p02841, 1980.

Ko, H.-C., Chun, H.-Y., Wilson, R., and Geller, M. A.: Characteristics of Atmospheric Turbulence Retrieved From High Vertical-Resolution Radiosonde Data in the United States, Journal of Geophysical Research: Atmospheres, 124, 7553–7579, doi:10.1029/2019JD030287, URL https://agupubs.onlinelibrary.wiley.com/doi/abs/10.1029/2019JD030287, 2019.

Koch, S. E., Jamison, B. D., Lu, C., Smith, T. L., Tollerud, E. I., Girz, C., Wang, N., Lane, T. P., Shapiro, M. A., Parrish, D. D., and Cooper, O. R.: Turbulence and Gravity Waves within an Upper-Level Front, Journal of the Atmospheric Sciences, 62, 3885–3908, doi:10.1175/JAS3574.1, URL https://doi.org/10.1175/JAS3574.1, 2005.

Kolmogorov, A.: The local structure of turbulence in incompressible viscous fluid for very large Reynolds numbers, in: Dokl. Akad. Nauk SSSR, vol. 30, pp. 299–303, 1941.

Kräuchi, A., Philipona, R., Romanens, G., Hurst, D. F., Hall, E. G., and Jordan, A. F.: Controlled weather balloon ascents and descents for atmospheric research and climate monitoring, Atmospheric Measurement Techniques, 9, 929–938, doi:10.5194/amt-9-929-2016, 2016.

Krisch, I., Preusse, P., Ungermann, J., Dörnbrack, A., Eckermann, S. D., Ern, M., Friedl-Vallon, F., Kaufmann, M., Oelhaf, H., Rapp, M., Strube, C., and Riese, M.: First tomographic observations of gravity waves by the infrared limb imager GLORIA, Atmospheric Chemistry and Physics, 17, 14 937–14 953, doi:10.5194/acp-17-14937-2017, URL https://www.atmos-chem-phys.net/17/14937/2017/, 2017.

Kruse, C. G., Smith, R. B., and Eckermann, S. D.: The Midlatitude Lower-Stratospheric Mountain Wave "Valve Layer", Journal of the Atmospheric Sciences, 73, 5081–5100, doi:10.1175/JAS-D-16-0173.1, URL https://doi.org/10.1175/JAS-D-16-0173.1, 2016.

Kunz, A., Konopka, P., Müller, R., and Pan, L. L.: Dynamical tropopause based on isentropic potential vorticity gradients, Journal of Geophysical Research: Atmospheres, 116, doi:10.1029/2010JD014343, URL https://agupubs.onlinelibrary.wiley.com/doi/abs/10.1029/2010JD014343, 2011.

Kyrazis, D. T., Eaton, F. D., Black, D. G., Black, W. T., and Black, A.: The balloon ring: a high-performance low-cost instrumentation platform for measuring atmospheric turbulence profiles, in: Atmospheric Optics: Models, Measurements, and Target-in-the-Loop Propagation III, vol. 7463, p. 746308, International Society for Optics and Photonics, doi:10.1117/12.827540, 2009.

Lane, T. P., Reeder, M. J., Morton, B. R., and Clark, T. L.: Observations and numerical modelling of mountain waves over the Southern Alps of New Zealand, Quarterly Journal of the Royal Meteorological Society, 126, 2765–2788, doi:10.1002/qj.49712656909, URL https://rmets.onlinelibrary.wiley.com/doi/abs/10.1002/qj.49712656909, 2000.

Lasance, C. J.: The Thermal Conductivity of Air at Reduced Pressures and Length Scales, Electronics Cooling, URL http://www.electronics-cooling.com/2002/11/the-thermal-conductivity-of-air-at-reduced-pressures-and-length-scales/, 2002.

Lawrence, D. A. and Balsley, B. B.: High-Resolution Atmospheric Sensing of Multiple Atmospheric Variables Using the DataHawk Small Airborne Measurement System, Journal of Atmospheric and Oceanic Technology, 30, 2352–2366, doi:10.1175/JTECH-D-12-00089.1, URL https://doi.org/10.1175/JTECH-D-12-00089.1, 2013.

Lesieur, M.: Turbulence in fluids, Springer, 2008.

Li, J. D.: Dynamic response of constant temperature hot-wire system in turbulence velocity measurements, Measurement Science and Technology, 15, 1835–1847, doi:10.1088/0957-0233/15/9/022, URL https://doi.org/10.1088%2F0957-0233%2F15%2F9%2F022, 2004.

Lilly, D., Waco, D., and Adelfang, S.: Stratospheric mixing estimated from high-altitude turbulence measurements, Journal of Applied Meteorology, 13, 488–493, 1974.

Lorenz, E. N.: The predictability of a flow which possesses many scales of motion, Tellus, 21, 289–307, doi:10.3402/tellusa.v21i3.10086, URL https://doi.org/10.3402/tellusa.v21i3.10086, 1969.

Lübken, F.-J.: On the extraction of turbulent parameters from atmospheric density fluctuations, Journal of Geophysical Research: Atmospheres, 97, 20 385–20 395, doi:10.1029/92JD01916, 1992.

Lübken, F.-J.: Experimental Results on the Role of Turbulence for the Heat Budget of the Upper Atmosphere, Habilitation, Rheinische Friedrich-Wilhelms-Universität, Bonn, 1993.

Luce, H., Fukao, S., Yamamoto, M., Sidi, C., and Dalaudier, F.: Validation of Winds Measured by MU Radar with GPS Radiosondes during the MUTSI Campaign, Journal of Atmospheric and Oceanic Technology, 18, 817–829, doi:10.1175/1520-0426(2001)018⟨0817:VOWMBM⟩2.0.CO;2, 2001.

Luers, J. K. and Eskridge, R. E.: Use of Radiosonde Temperature Data in Climate Studies, Journal of Climate, 11, 1002–1019, doi:10.1175/1520-0442(1998)011⟨1002:UORTDI⟩2.0.CO;2, 1998.

Lübken, F.-J., Berger, U., and Baumgarten, G.: Temperature trends in the midlatitude summer mesosphere, Journal of Geophysical Research: Atmospheres, 118, 13,347–13,360, doi:10.1002/2013JD020576, URL https://agupubs.onlinelibrary.wiley.com/doi/abs/10.1002/2013JD020576, 2013.

MacCready, P. B.: Comparison of Some Balloon Techniques, Journal of Applied Meteorology, 4, 504–508, doi:10.1175/1520-0450(1965)004⟨0504:COSBT⟩2.0.CO;2, 1965.

Mathieu, J. and Scott, J.: An introduction to turbulent flow, Cambridge University Press, 2000.

Mlawer, E. J., Taubman, S. J., Brown, P. D., Iacono, M. J., and Clough, S. A.: Radiative transfer for inhomogeneous atmospheres: RRTM, a validated correlated-k model for the longwave, J. Geophys. Res., 102, 16 663–16 682, doi:10.1029/97JD00237, 1997.

Murrow, H. N. and Henry, R. M.: Self-Induced Balloon Motions, Journal of Applied Meteorology, 4, 131–138, doi:10.1175/1520-0450(1965)004⟨0131:SIBM⟩2.0.CO;2, 1965.

Muschinski, A., Frehich, R., Jensen, M., Hugo, R., Hoff, A., Eaton, F., and Balsley, B.: Fine-Scale Measurements Of Turbulence In The Lower Troposphere: An Intercomparison Between A Kite- And Balloon-Borne, And A Helicopter-Borne Measurement System, Boundary-Layer Meteorology, 98, 219–250, doi:10.1023/A:1026520618624, URL https://doi.org/10.1023/A:1026520618624, 2001.

Nakanishi, M. and Niino, H.: Development of an Improved Turbulence Closure Model for the Atmospheric Boundary Layer, J. Meteor. Soc. Japan, 87, 895–912, URL http://ci.nii.ac.jp/naid/110007465760/en/, 2009.

Nappo, C. J.: An Introduction to Atmospheric Gravity Waves, Volume 102 (International Geophysics), Academic Press, 2012.

NOAA: US standard atmosphere, 1976, Tech. rep., NOAA-S/T, 1976.

Norman, A. K. and McKeon, B. J.: Unsteady force measurements in sphere flow from subcritical to supercritical Reynolds numbers, Experiments in Fluids, 51, 1439, doi:10.1007/s00348-011-1161-8, URL https://doi.org/10.1007/s00348-011-1161-8, 2011.

Ozmidov, R.: On the turbulent exchange in a stably stratified ocean, Izv. Acad. Sci. USSR, Atmos. Oceanic Phys, 1, 861–871, 1965.

Plougonven, R. and Zhang, F.: Internal gravity waves from atmospheric jets and fronts, Reviews of Geophysics, 52, 33–76, 2014.

Podglajen, A., Bui, T. P., Dean-Day, J. M., Pfister, L., Jensen, E. J., Alexander, M. J., Hertzog, A., Kärcher, B., Plougonven, R., and Randel, W. J.: Small-Scale Wind Fluctuations in the Tropical Tropopause Layer from Aircraft Measurements: Occurrence, Nature, and Impact on Vertical Mixing, Journal of the Atmospheric Sciences, 74, 3847–3869, 2017.

Pope, S. B.: Turbulent flows, Cambridge university press, 2000.

Prusa, J. M., Smolarkiewicz, P. K., and Wyszogrodzki, A. A.: EULAG, a computational model for multiscale flows, Computers & Fluids, 37, 1193 – 1207, doi:https://doi.org/10.1016/j.compfluid.2007.12.001, URL http://www.sciencedirect.com/science/article/pii/S004579300700206X, 2008.

Reed, R. J.: A STUDY OF A CHARACTERISTIC TPYE OF UPPER-LEVEL FRONTOGENESIS, Journal of Meteorology, 12, 226–237, doi:10.1175/1520-0469(1955)012⟨0226:ASOACT⟩2.0.CO;2, URL https://doi.org/10.1175/1520-0469(1955)012<0226:ASOACT>2.0.CO;2, 1955.

Reeder, M. J., Adams, N., and Lane, T. P.: Radiosonde observations of partially trapped lee waves over Tasmania, Australia, Journal of Geophysical Research: Atmospheres, 104, 16 719–16 727, doi:10.1029/1999JD900038, URL https://agupubs.onlinelibrary.wiley.com/doi/abs/10.1029/1999JD900038, 1999.

Reid, H. J. and Vaughan, G.: Convective mixing in a tropopause fold, Quarterly Journal of the Royal Meteorological Society, 130, 1195–1212, doi:10.1256/qj.03.21, URL https://rmets.onlinelibrary.wiley.com/doi/abs/10.1256/qj.03.21, 2004.

Reiter, E. R.: Stratospheric-tropospheric exchange processes, Reviews of Geophysics, 13, 459–474, doi:10.1029/RG013i004p00459, URL https://agupubs.onlinelibrary.wiley.com/doi/abs/10.1029/RG013i004p00459, 1975.

Reynolds, O.: XXIX. An experimental investigation of the circumstances which determine whether the motion of water shall be direct or sinuous, and of the law of resistance in parallel channels, Philosophical Transactions of the Royal Society of London, 174, 935–982, doi:10.1098/rstl.1883.0029, URL https://royalsocietypublishing.org/doi/abs/10.1098/rstl.1883.0029, 1883.

Reynolds, O.: IV. On the dynamical theory of incompressible viscous fluids and the determination of the criterion, Philosophical Transactions of the Royal Society of London. (A.), 186, 123–164, doi:10.1098/rsta.1895.0004, URL https://royalsocietypublishing.org/doi/abs/10.1098/rsta.1895.0004, 1895.

Richardson, L. F.: Weather prediction by numerical process, Cambridge University Press, 1922.

Riddhagni, P., Bevilaqua, P., and Lykoudis, P.: Measurements in the turbulent wake of a sphere, AIAA Journal, 9, 1433–1434, doi:10.2514/3.6379, 1971.

Roshko, A.: On the development of turbulent wakes from vortex streets, Tech. Rep. 1191, California Institute of Technology, URL https://ntrs.nasa.gov/archive/nasa/casi.ntrs.nasa.gov/19930092207.pdf, 1954.

Schmaltz, J.: Cloud picture of Jan mayen Islands on 5 May 2012, https://eoimages.gsfc.nasa.gov/images/imagerecords/77000/77654/JanMayen_amo_2012096_lrg.jpg, online; accessed 31 July 2019, 2012.

Schneider, A.: In-situ turbulence observations in the stratospheric wind and temperature field, dissertation, Universität Rostock, URL https://www.iap-kborn.de/fileadmin/user_upload/MAIN-abteilung/optik/Forschung/Doktorarbeiten/Schneider-Diss-2015.pdf, 2015.

Schneider, A., Gerding, M., and Lübken, F.-J.: Comparing turbulent parameters obtained from LITOS and radiosonde measurements, Atmospheric Chemistry and Physics, 15, 2159–2166, doi:10.5194/acp-15-2159-2015, 2015.

Schneider, A., Wagner, J., Söder, J., Gerding, M., and Lübken, F.-J.: Case study of wave breaking with high-resolution turbulence measurements with LITOS and WRF simulations, Atmospheric Chemistry and Physics, 17, 7941–7954, doi:10.5194/acp-17-7941-2017, 2017.

Scoggins, J. R.: Spherical Balloon Wind Sensor Behavior, Journal of Applied Meteorology, 4, 139–145, doi:10.1175/1520-0450(1965)004⟨0139:SBWSB⟩2.0.CO;2, 1965.

Scoggins, J. R.: Sphere behavior and the measurement of wind profiles, Tech. rep., NASA, Washington, D.C., URL https://ntrs.nasa.gov/archive/nasa/casi.ntrs.nasa.gov/19670017960.pdf, 1967.

Scorer, R. S.: Theory of waves in the lee of mountains, Quarterly Journal of the Royal Meteorological Society, 75, 41–56, doi:10.1002/qj.49707532308, URL https://rmets.onlinelibrary.wiley.com/doi/abs/10.1002/qj.49707532308, 1949.

Shapiro, M. A.: The Role of Turbulent Heat Flux in the Generation of Potential Vorticity in the Vicinity of Upper-Level Jet Stream Systems, Monthly Weather Review, 104, 892–906, doi:10.1175/1520-0493(1976)104⟨0892:TROTHF⟩2.0.CO;2, URL https://doi.org/10.1175/1520-0493(1976)104<0892:TROTHF>2.0.CO;2, 1976.

Shapiro, M. A.: Further Evidence of the Mesoscale and Turbulent Structure of Upper Level Jet StreamFrontal Zone Systems, Monthly Weather Review, 106, 1100–1111, doi:10.1175/1520-0493(1978)106⟨1100:FEOTMA⟩2.0.CO;2, URL https://doi.org/10.1175/1520-0493(1978)106<1100:FEOTMA>2.0.CO;2, 1978.

Shapiro, M. A.: Turbulent Mixing within Tropopause Folds as a Mechanism for the Exchange of Chemical Constituents between the Stratosphere and Troposphere, Journal of the Atmospheric Sciences, 37, 994–1004, doi:10.1175/1520-0469(1980)037⟨0994:TMWTFA⟩2.0.CO;2, URL https://doi.org/10.1175/1520-0469(1980)037<0994:TMWTFA>2.0.CO;2, 1980.

Sharman, R., Tebaldi, C., Wiener, G., and Wolff, J.: An Integrated Approach to Mid- and Upper-Level Turbulence Forecasting, Weather and Forecasting, 21, 268–287, doi:10.1175/WAF924.1, URL https://doi.org/10.1175/WAF924.1, 2006.

Sharman, R., Trier, S., Lane, T., and Doyle, J.: Sources and dynamics of turbulence in the upper troposphere and lower stratosphere: A review, Geophysical Research Letters, 39, 2012.

Sharman, R., Cornman, L., Meymaris, G., Pearson, J., and Farrar, T.: Description and derived climatologies of automated in situ eddy-dissipation-rate reports of atmospheric turbulence, Journal of Applied Meteorology and Climatology, 53, 1416–1432, 2014.

Sharman, R. D. and Pearson, J. M.: Prediction of Energy Dissipation Rates for Aviation Turbulence. Part I: Forecasting Nonconvective Turbulence, Journal of Applied Meteorology and Climatology, 56, 317–337, doi:10.1175/JAMC-D-16-0205.1, 2017.

Shutts, G. and Broad, A.: A case study of lee waves over the Lake District in northern England, Quarterly Journal of the Royal Meteorological Society, 119, 377–408, doi:10.1002/qj.49711951102, URL https://rmets.onlinelibrary.wiley.com/doi/abs/10.1002/qj.49711951102, 1993.

Shutts, G. J., Kitchen, M., and Hoare, P. H.: A large amplitude gravity wave in the lower stratosphere detected by radiosonde, Quarterly Journal of the Royal Meteorological Society, 114, 579–594, doi:10.1002/qj.49711448103, URL https://rmets.onlinelibrary.wiley.com/doi/abs/10.1002/qj.49711448103, 1988.

Skamarock, W. C., Klemp, J. B., Dudhia, J., Gill, D. O., Barker, D. M., Duda, M. G., Huang, X.-Y., Wang, W., and Powers, J. G.: A description of the Advanced Research WRF Version 3, NCAR technical note, Mesoscale and Microscale Meteorology Division, National Center for Atmospheric Research, Boulder, Colorado, USA, URL http://www2.mmm.ucar.edu/wrf/users/docs/arw_v3.pdf, 2008.

Smith, R. B. and Kruse, C. G.: Broad-Spectrum Mountain Waves, Journal of the Atmospheric Sciences, 74, 1381–1402, doi:10.1175/JAS-D-16-0297.1, URL https://doi.org/10.1175/JAS-D-16-0297.1, 2017.

Söder, J., Gerding, M., Schneider, A., Dörnbrack, A., Wilms, H., Wagner, J., and Lübken, F.-J.: Evaluation of wake influence on high-resolution balloon-sonde measurements, Atmospheric Measurement Techniques, 12, 4191–4210, doi:10.5194/amt-12-4191-2019, URL https://www.atmos-meas-tech.net/12/4191/2019/, 2019.

Strelnikov, B., Szewczyk, A., Strelnikova, I., Latteck, R., Baumgarten, G., Lübken, F.-J., Rapp, M., Fasoulas, S., Löhle, S., Eberhart, M., Hoppe, U.-P., Dunker, T., Friedrich, M., Hedin, J., Khaplanov, M., Gumbel, J., and Barjatya, A.: Spatial and temporal variability in MLT turbulence inferred from in situ and ground-based observations during the WADIS-1 sounding rocket campaign, Annales Geophysicae, 35, 547–565, doi:10.5194/angeo-35-547-2017, URL https://www.ann-geophys.net/35/547/2017/, 2017.

Survo, P., Turunen, M., Salo, T., and Jauhiainen, H.: VAISALA RADIOSONDE RS41–NEW SENSING TECHNOLOGIES FOR OPERATIONAL UPPER AIR MEASUREMENTS, https://www.wmo.int/pages/prog/www/IMOP/publications/IOM-116_TECO-2014/Session%201/O1_4_Survo_VaisalaRS41.pdf, 2014.

Sutherland, B. R.: Internal gravity waves, Cambridge University Press, 2010.

Söder, J.: Development of a small-scale LITOS payload for turbulence measurements in the stratosphere, Master's thesis, Rostock University, URL https://www.iap-kborn.de/fileadmin/user_upload/MAIN-abteilung/optik/Forschung/Master/Soeder-Master-2014.pdf, 2014.

Taneda, S.: Downstream Development of the Wakes behind Cylinders, Journal of the Physical Society of Japan, 14, 843–848, doi:10.1143/JPSJ.14.843, 1959.

Taneda, S.: Visual observations of the flow past a sphere at Reynolds numbers between 10^4 and 10^6, Journal of Fluid Mechanics, 85, 187–192, doi:10.1017/S0022112078000580, 1978.

Tatarskii, V. I.: The effects of the turbulent atmosphere on wave propagation, Israel Program for Scientific Translations, 1971.

Taylor, G.: The spectrum of turbulence, Proceedings of the Royal Society of London. Series A-Mathematical and Physical Sciences, 164, 476–490, 1938.

Tennekes, H. and Lumley, J. L.: A First Course in Turbulence, MIT Press, 1972.

Theuerkauf, A.: Stratospheric turbulence observation with the new balloon-borne instrument LITOS, dissertation, Universität Rostock, URL https://www.iap-kborn.de/fileadmin/user_upload/MAIN-abteilung/optik/Forschung/Doktorarbeiten/Theuerkauf-Diss-2012.pdf, 2012.

Theuerkauf, A., Gerding, M., and Lübken, F.-J.: LITOS – a new balloon-borne instrument for fine-scale turbulence soundings in the stratosphere, Atmospheric Measurement Techniques, 4, 55–66, doi:10.5194/amt-4-55-2011, 2011.

Tiefenau, H. K. E. and Gebbeken, A.: Influence of Meteorological Balloons on Temperature Measurements with Radiosondes: Nighttime Cooling and Daylight Heating, Journal of Atmospheric and Oceanic Technology, 6, 36–42, doi:10.1175/1520-0426(1989)006⟨0036:IOMBOT⟩2.0.CO;2, 1989.

Torrence, C. and Compo, G. P.: A practical guide to wavelet analysis, Bulletin of the American Meteorological society, 79, 61–78, 1998.

Tsuda, T., Kato, S., Yokoi, T., Inoue, T., Yamamoto, M., VanZandt, T. E., Fukao, S., and Sato, T.: Gravity waves in the mesosphere observed with the middle and upper atmosphere radar, Radio Science, 25, 1005–1018, doi:10.1029/RS025i005p01005, URL https://agupubs.onlinelibrary.wiley.com/doi/abs/10.1029/RS025i005p01005, 1990.

Vincent, R. A. and Alexander, J. M.: Gravity waves in the tropical lower stratosphere: An observational study of seasonal and interannual variability, Journal of Geophysical Research: Atmospheres, 105, 17 971–17 982, doi:10.1029/2000JD900196, URL https://agupubs.onlinelibrary.wiley.com/doi/abs/10.1029/2000JD900196, 2000.

White, C., Borg, M., Scanlon, T., Longshaw, S., John, B., Emerson, D., and Reese, J.: dsmcFoam+: An OpenFOAM based direct simulation Monte Carlo solver, Computer Physics Communications, 224, 22 – 43, doi:https://doi.org/10.1016/j.cpc.2017.09.030, URL http://www.sciencedirect.com/science/article/pii/S0010465517303375, 2018.

Wilczek, M., Xu, H., and Narita, Y.: A note on Taylor's hypothesis under large-scale flow variation, Nonlinear Processes in Geophysics, 21, 645–649, doi:10.5194/npg-21-645-2014, URL https://www.nonlin-processes-geophys.net/21/645/2014/, 2014.

Williamson, C. H.: Vortex dynamics in the cylinder wake, Annual Review of Fluid Mechanics, 28, 477–539, doi:10.1146/annurev.fl.28.010196.002401, 1996.

Wilson, C., Camilletti, A., Calcutt, S., and Ligrani, P.: A wind tunnel for the calibration of Mars wind sensors, Planetary and Space Science, 56, 1532 – 1541, doi:https://doi.org/10.1016/j.pss.2008.05.011, URL http://www.sciencedirect.com/science/article/pii/S0032063308001438, 2008.

Wilson, R., Luce, H., Dalaudier, F., and Lefrère, J.: Turbulence Patch Identification in Potential Density or Temperature Profiles, Journal of Atmospheric and Oceanic Technology, 27, 977–993, doi:10.1175/2010JTECHA1357.1, 2010.

Wilson, R., Dalaudier, F., and Luce, H.: Can one detect small-scale turbulence from standard meteorological radiosondes?, Atmospheric Measurement Techniques, 4, 795–804, doi:10.5194/amt-4-795-2011, 2011.

WMO: Definition of the tropopause, vol. VI, pp. 136–137, URL https://library.wmo.int/doc_num.php?explnum_id=6960, accessed: 06/07/2020, 1957.

Woiwode, W., Dörnbrack, A., Bramberger, M., Friedl-Vallon, F., Haenel, F., Höpfner, M., Johansson, S., Kretschmer, E., Krisch, I., Latzko, T., Oelhaf, H., Orphal, J., Preusse, P., Sinnhuber, B.-M., and Ungermann, J.: Mesoscale fine structure of a tropopause fold over mountains, Atmospheric Chemistry and Physics, 18, 15 643–15 667, doi:10.5194/acp-18-15643-2018, URL https://www.atmos-chem-phys.net/18/15643/2018/, 2018.

Wyngaard, J. C. and Clifford, S. F.: Taylor's Hypothesis and HighFrequency Turbulence Spectra, Journal of the Atmospheric Sciences, 34, 922–929, doi:10.1175/1520-0469(1977)034⟨0922:THAHTS⟩2.0.CO;2, URL https://doi.org/10.1175/1520-0469(1977)034<0922:THAHTS>2.0.CO;2, 1977.

Xie, F., Li, Y., Liu, Z., Wang, X., and Wang, L.: A forced convection heat transfer correlation of rarefied gases cross-flowing over a circular cylinder, Experimental Thermal and Fluid Science, 80, 327 – 336, doi:https://doi.org/10.1016/j.expthermflusci.2016.09.002, URL http://www.sciencedirect.com/science/article/pii/S0894177716302461, 2017.

Zhang, J., Zhang, S. D., Huang, C. M., Huang, K. M., Gong, Y., Gan, Q., and Zhang, Y. H.: Statistical Study of Atmospheric Turbulence by Thorpe Analysis, Journal of Geophysical Research: Atmospheres, 124, 2897–2908, doi:10.1029/2018JD029686, URL https://agupubs.onlinelibrary.wiley.com/doi/abs/10.1029/2018JD029686, 2019a.

Zhang, J., Zhang, S. D., Huang, C. M., Huang, K. M., Gong, Y., Gan, Q., and Zhang, Y. H.: Latitudinal and Topographical Variabilities of Free Atmospheric Turbulence From High-Resolution Radiosonde Data Sets, Journal of Geophysical Research: Atmospheres, 124, 4283–4298, doi:10.1029/2018JD029982, URL https://agupubs.onlinelibrary.wiley.com/doi/abs/10.1029/2018JD029982, 2019b.

Acknowledgements

First of all, I like to thank my colleagues from IAP and beyond for the pleasure of being able to collaborate with you.

Namely, I am grateful to Franz-Josef Lübken for the opportunity to work in his department. This starts with funding, includes the supervision of publications and this thesis as well as the ability to carry out field campaigns and does not end with his efforts to make atmospheric science accessible to the public. Furthermore I owe gratitude to Richard Wilson for kindly serving as the second referee of my PhD.

Particular thanks go to Michael Gerding for his unassuming way of supporting me throughout this thesis. This includes countless discussions on the development of the LITOS payload, campaign planning and geophysical questions. He never lost his temper even when I raised fundamental questions, challenging our way of measuring turbulence.

Furthermore, I am grateful for the technical support received in the development and deployment of the LITOS system. In particular, I like to mention Reik Ostermann who developed the electronics as well as Michael Priester who provided lots of operational support, be it in Kühlungsborn or during field campaigns. Moreover, Torsten Köpnick was always available for discussions on general issues with the electronics and beyond.

Additionally, I am indebted to Andreas Schneider for his patience when introducing me to a lot of topics from general programming issues to questions about our data retrieval. The same is true for Tristan Staszak, with whom I enjoyed pondering about numerical simulations as well as sources of error on turbulence measurements. Furthermore, I was pleased to learn about meteorological phenomena in general and tropopause folds in particular from Christoph Zülicke.

There have been numerous collaborations outside IAP which I particularly enjoyed. Many of them where encouraged by the DFG research group MS-GWaves led by Ulrich Achatz. In particular I received a lot of input from Andreas Dörnbrack, who also kindly invited our LITOS team to launch from their site in Kiruna during the GW-LCycle II campaign in January 2016.

There was also fruitful cooperation with Dale Lawrence and Dave Fritts from the MURI project. I am particularly thankful to Dale Lawrence for the extremely pleasant working atmosphere during our campaign in November 2018. Furthermore, I am indebted to Henrike Wilms, Mark Schlutow and Martina Bramberger for rewarding conversations on matters of turbulence and beyond. Henrike Wilms also kindly and enthusiastically set up the EULAG simulations that are used in this thesis.

WRF simulations used in the course of this thesis have been kindly provided by Johannes Wagner. Gerd Baumgarten acquired the ECMWF data used here. Financial support was given by the Bundesministerium für Bildung und Forschung (ROMIC-METROSI, grant no. 01 LG 1218A). The radiosonde dataset used in Chapter 3 has been acquired by DLR-IPA, supported by ROMIC-GW-LCYCLE, grant no. 01 LG 1206A.

In addition, I owe gratitude to Eric Wolever for proofreading this thesis. Last but not least, I am most grateful to friends and family with Josephine Faber in particular for their sincere support and genuine interest in the project.

Statement of authorship

I hereby certify that the work presented in this thesis has been performed solely by myself except where explicitly identified to the contrary. Any sources from which I used data, ideas or words either in quotation or in paraphrase are cited.

I confirm that this work has not been submitted elsewhere in any other form for the fulfilment of any other degree or qualification. Furthermore I confirm that I have not sought to obtain a doctoral degree at any other university.

Rostock, 10 December 2019

(Jens Söder)

,